Thermal Expansion and Transport Properties of Low-Dimensional Organic Conductors

Dissertation
zur Erlangung des Doktorgrades
der Naturwissenschaften

vorgelegt beim Fachbereich Physik
der Johann Wolfgang Goethe Universität
in Frankfurt (M)

von
Valdeci Pereira Mariano de Souza
aus Mogi das Cruzes - SP, Brasilien

Frankfurt am Main (2008)

vom Fachbereich Physik der Goethe Universität als Dissertation angenommen.

Dekan: Prof. Dr. Michael Huth

Gutachter: Prof. Dr. Michael Lang
Prof. Dr. Naoki Toyota (Tohoku University, Sendai - Japan)
Prof. Dr. Wolf Aßmus (als Vertretung von Prof. Toyota in der Disputation)

Einreichung: 04.11.2008
Datum der Disputation: 29.01.2009

Kurzfassung

Die vorliegende Arbeit beschäftigt sich hauptsächlich mit der thermischen Ausdehnung niedrigdimensionaler organischer Leiter. Die thermische Ausdehnung kristalliner Materialien ist ein wohlverstandener physikalischer Prozess [1]. Er beruht auf der Temperaturabhängigkeit der interatomaren Abstände, welche wiederum von der Anharmonizität der Gitterschwingungen hervorgerufen wird. Bei den hier untersuchten organischen Ladungstransfersalzen handelt es sich um stark korrelierte, elektronisch ein- oder zweidimensionale Systeme, deren verschiedenartige Grundzustände durch das Wechselspiel von Spin-, Ladungs- und Gitterfreiheitsgraden bestimmt werden. Aufgrund der Größe der Effekte haben sich thermische Ausdehnungsmessungen als eine äußerst nützliche Methode erwiesen, um tiefere Einblicke in die Physik dieser Materialien zu gewinnen. Die hier vorgestellten Ergebnisse wurden an einem ultrahochauflösenden Dilatometer aus der Arbeitsgruppe von Prof. Dr. Michael Lang (Physikalisches Institut, Goethe Universität - Frankfurt (M)) gewonnen [2].

Systematische Untersuchungen zur thermischen Ausdehnung wurden im Rahmen dieser Arbeit an zwei Materialklassen durchgeführt, zum einen an der Familie der quasi-eindimensionalen organischen Leiter $(TMTTF)_2X$, wobei TMTTF für Tetramethyltetrathiofulvalen steht, und X ein einwertiges Anion (X = PF_6, AsF_6 oder SbF_6) ist, und zum anderen an der Familie der quasi-zweidimensionalen Leiter κ-$(ET)_2X$, wobei ET = BEDT-TTF die Abkürzung für Bis(ethylen-dithiolo)tetrathiofulvalen ($C_{10}S_8H_8$), und X wieder ein einwertiges Anion ist. Diese Materialien stellen Modellsysteme zur Erforschung elektronischer Korrelationen in einer oder zwei Dimensionen dar. Insbesondere hat das vollständig deuterierte Salz κ-$(D8\text{-}ET)_2Cu[N(CN)_2]Br$ ("κ-D8-Br") Aufmerksamkeit auf sich gezogen, da es sich im Phasendiagramm in unmittelbarer Nähe zur *S*-förmigen Phasengrenzlinie befindet [3], die den metallischen vom isolierenden Bereich trennt. Dies ermöglicht es, den Mottschen Metall-Isolator(MI)-Übergang (1. Ordnung), eines der Hauptforschungsfelder auf dem Gebiet der stark korrelierten elektronischen Systeme, als Funktion der Temperatur zu untersuchen. Im Rahmen dieser Arbeit wurden zum ersten Mal experimentelle Resultate gewonnen, welche die wichtige Rolle belegen, die die Gitterfreiheitsgrade für den Mott-MI-Übergang in den obigen Materialien spielen [4].

Um die Gittereffekte zu untersuchen, die bei letztgenanntem System am Mott-Übergang auftreten, wurden richtungsabhängige thermische Ausdehnungsmessungen durchgeführt. Dazu wurde ein ultrahochauflösendes kapazitives Dilatometer (Konstruktion nach [60]) verwendet, das eine maximale relative Längenauflösung von $\Delta l/l = 10^{-10}$ besitzt und in einem Temperaturbereich von 1,6 bis 200 K betrieben werden kann. Zusätzlich kann ein Magnetfeld mit einer Maximalstärke von 10 T angelegt werden. Die genannte Auflösung ist im Allgemeinen nur bis zu einer Temperatur von $T \simeq 40$ K erreichbar, weil darüber eine genaue Temperaturkontrolle aufgrund der Größe der auftretenden Zeitkonstante zunehmend schwierig wird. Um externe Schwingun-

gen abzufangen, ist der Kryostat mit Vibrationsdämpfern ausgestattet. Die Messzelle (fast vollständig aus hochreinem Kupfer) besteht im Wesentlichen aus einem Rahmen und zwei parallelen Stempeln, von denen der obere in der Höhe verstellbar ist, um die Probe zwischen die beiden Stempel platzieren zu können. Der untere Stempel, der beweglich (über Federn) am Zellrahmen aufgehängt ist, ist fest mit der oberen Platte eines Plattenkondensators verbunden, während die untere Platte am Zellrahmen befestigt ist. Das Messprinzip ist sehr einfach: Eine Änderung der Probenlänge, also eine Expansion oder eine Kontraktion, bei steigender bzw. fallender Temperatur spiegelt sich in einer Änderung des Plattenabstands des Kondensators und folglich in einer Kapazitätsänderung wider, aus deren Messung auf die Längenänderung zurückgeschlossen werden kann. Die bemerkenswerteste Eigenschaft des Dilatometers ist die bereits erwähnte enorm hohe Auflösung von $\Delta l/l = 10^{-10}$, die für eine 1 mm lange Probe einer absoluten Auflösung von 0,01 Angstrom entspricht. Dieser Wert, der vor allem durch die gute Auflösung der verwendeten Kapazitätsbrücke und die hohe Qualität der Messzelle bedingt ist, übertrifft den von konventionellen Methoden wie Neutronen- oder Röntgenstreuung um etwa fünf Größenordnungen, was die Messung winzig kleiner Gitteränderungen gestattet.

Kühlt man das System κ-D8-Br ab, so zeigt es bei der Temperatur $T_p \simeq 30$ K, am kritischen Endpunkt der 1. Ordnungs-Phasengrenzlinie, eine kontinuierliche Veränderung der Gitterparameter. Innerhalb der Messgenauigkeit konnten hier keinerlei Hystereseerscheinungen beobachtet werden, was auf einen Übergang 2. Ordnung hinweist. Eine abruptere Änderung der Gitterparameter tritt bei weiterem Abkühlen bei der Temperatur T_{MI} = 13,6 K, der Mott-MI-Übergangstemperatur, auf.

Diese Änderung ist entlang der *a*-Achse (parallel zu den elektrisch leitenden ET-Ebenen) und entlang der *b*-Achse (senkrecht zu den Ebenen) am stärksten ausgeprägt, während man entlang der *c*-Achse, der zweiten parallel zu den ET-Ebenen liegenden Richtung, erstaunlicherweise so gut wie keinen Effekt beobachtet. Dies ist ein Anzeichen dafür, dass in diesem System am Mott-MI-Übergang eine Kopplung zwischen den Elektronen und den Gitterfreiheitsgraden vorliegt. Die Anisotropie kann nicht im Rahmen eines rein zweidimensionalen elektronischen Modells erklärt werden, dass aus Dimeren auf einem anisotropen Dreiecksgitter bestünde. Die Hysterese in der relativen Längenänderung entlang der *a*-Achse bestätigt, dass es sich um einen Übergang erster Ordnung handelt.

Ein weiteres Material, das in den letzten Jahren große Aufmerksamkeit auf sich gezogen hat, ist die Verbindung κ-$(ET)_2Cu_2(CN)_3$ [5]. Die Spins in diesem System sind in einem nahezu perfekt frustrierten quasi-zweidimensionalen Dreiecksgitter angeordnet, das heißt für das Verhältnis der Überlapp-Integrale (Hüpfamplituden) gilt $t/t' \simeq 1$. Bis hin zu den tiefsten erreichbaren Temperaturen wurden bislang keinerlei Anzeichen einer langreichweitigen Ordnung entdeckt. Aus diesen Gründen gilt das System als aussichtsreicher Kandidat für die Realisierung einer Spin-Flüssigkeit. Ein Vorschlag aus der Literatur besagt, dass bei $T \simeq 6$ K ein Crossover, auch versteckte Ordnung genannt, in die Spinflüssigkeits-Phase vorliegt. Die Natur dieses Crossovers bzw. Übergangs ist noch umstritten. α_c, der thermische Ausdehnungskoeffizient entlang der *c*-Richtung, nimmt mit fallender Temperatur zunächst bis $T_{min} \simeq 30$ K monoton ab. Eine breite Anomalie ist bei $T \simeq 150$ K zu sehen. Oberhalb dieser Temperatur haben Y. Shimizu *et al.* eine Zunahme der Kernspin-Relaxationsrate festgestellt, die sie mit der thermisch aktivierten Schwingung der Ethylen-Endgruppen in Verbindung brachten [110].

Es sind keine Spuren einer glasartigen Anomalie bei T = 77 - 80 K zu erkennen. Dieses Verhalten unterscheidet sich deutlich von dem in den Systemen κ-$(ET)_2Cu[N(CN)_2]Cl$ [86], κ-D8-Br (in dieser Arbeit untersucht) und κ-H8-Br [86] beobachteten, bei denen

der thermische Ausdehnungskoeffizient deutliche Signaturen bei $T_g \simeq 77\,\mathrm{K}$ zeigt. Dies deutet darauf hin, dass sich die Gitterdynamik von κ-$(ET)_2Cu_2(CN)_3$ von der der gerade genannten Verbindungen unterscheidet. In der Tat kann das Fehlen einer glasartigen Anomalie in κ-$(ET)_2Cu_2(CN)_3$ mit Hilfe des Modells der rigid-unit modes (RUM) (siehe [122] und die darin zitierten Referenzen) verstanden werden: Die $Cu_2(CN)_3{}^-$-Anionen bilden ein zweidimensionales Netzwerk aus Cu(I)-Ionen und verbrückenden Cyanid-Gruppen [92]. Dies stellt einen markanten Unterschied zur Polymer-Anordnung der Anionen in κ-$(ET)_2Cu[N(CN)_2]Cl$ und κ-$(ET)_2Cu[N(CN)_2]Br$ dar. Die Schwingungsmoden der CN-Gruppen sind in κ-$(ET)_2Cu_2(CN)_3$ demzufolge auf den Bereich zwischen benachbarten Cu(I)-Ionen beschränkt und können sich nicht entlang der Struktur ausbreiten, wodurch das Auftreten von RUM-Moden unterbunden ist, und folglich keine Signaturen eines glasartigen Übergangs auftreten. Eine weitere breite Anomalie in α_c ist bei $T_{max,\chi} \simeq 70\,\mathrm{K}$ sichtbar. Bei etwa dieser Temperatur zeigt auch die magnetische Suszeptibilität ein breites Maximum [110]. Unterhalb von $T \simeq 50\,\mathrm{K}$ nimmt α_c negative Werte an und durchläuft ein breites Minimum bei $T_{min} \simeq 30\,\mathrm{K}$, um unterhalb von $T \simeq 14\,\mathrm{K}$ erneut positiv zu werden. Ein mögliches Szenario zur Erklärung der negativen thermischen Ausdehnung im Bereich $14\,\mathrm{K} \lesssim T \lesssim 50\,\mathrm{K}$ sieht so aus, dass in diesem Temperaturbereich (höchstwahrscheinlich anionische) Gitterschwingungsmoden weich werden, der Grüneisenparameter daher negative Werte annimmt und sich das Gitter beim Abkühlen ausdehnt. Andererseits kann die Hypothese einer von den Spinfreiheitsgraden getriebenen negativen thermischen Ausdehnung nicht ausgeschlossen werden. So wird in der Literatur von einem Zusammenhang zwischen negativer thermischer Ausdehnung und Frustration berichtet [143], obgleich eine Theorie zur Erklärung dieses Phänomens noch aussteht. Bei weiterem Abkühlen wird in α_c eine erstaunlich stark ausgeprägte Anomalie bei $T^{anom} \simeq 6\,\mathrm{K}$ sichtbar, die bei derselben Temperatur, wenngleich deutlich schwächer ausgeprägt, auch in der spezifischen Wärme erscheint [5]. Thermische Ausdehnungsmessungen entlang der *b*-Achse, die genau wie die *c*-Achse parallel zu den ET-Ebenen liegt, offenbaren eine bemerkenswerte Ausdehnungsanisotropie bei T^{anom}, das heißt, der vorgeschlagene Crossover in den Spinflüssigkeits-Zustand geht mit einer starken Verzerrung innerhalb der ET-Ebenen einher. Unsere Ergebnisse stellen den ersten Nachweis von Gittereffekten bei T^{anom} dar. Bei noch tieferen Temperaturen ($T \simeq 2{,}8\,\mathrm{K}$) zeigen die Daten eine weitere sprungförmige Anomalie, zu der in spezifischen Wärmemessungen keine Entsprechung gefunden wurde [5], vermutlich aufgrund der zu geringen Auflösung solcher Experimente.

Die Signaturen in α_c haben ihre direkte Entsprechung in der Kernspin-Relaxationsrate (T_1^{-1}) und magnetischen Suszeptibilität (χ) [110]. Unterhalb von 50 K nehmen beide Größen bis zu einer Temperatur von 4 K monoton ab, wonach T_1^{-1} wieder zuzunehmen beginnt und ein breites Maximum bei 1 K zeigt, während χ weiterhin kontinuierlich abnimmt. Thermische Ausdehnungsmessungen bei einem angelegten Magnetfeld von 8 T entlang der *c*-Achse ließen keinerlei Veränderungen, weder des scharfen Maximums bei 6 K noch der Anomalie bei 2,8 K, im Vergleich zu den Nullfelddaten erkennen. Diese fehlende Magnetfeldabhängigkeit, die sich auch in der spezifischen Wärme zeigt [5], macht eine langreichweitige magnetische Ordnung als Ursache der Anomalie bei 6 K unwahrscheinlich. Außerdem ergaben im Abkühlen und im Aufwärmen durchgeführte Messungen keinerlei Hinweise auf hysteretisches Verhalten, zumindest innerhalb der experimentellen Auflösung, so dass ein Übergang erster Ordnung ausgeschlossen werden kann. Somit bleibt die Ursache der Anomalie bei 6 K unbekannt, wenn auch die vorliegenden Ergebnisse zur thermischen Ausdehnung mit einem von Lee *et al.* vorgeschlagenen Modell [115] in Einklang zu stehen scheinen. Hiernach wird durch Spinpaarung auf der Fermifläche eine spontane Brechung der Gittersymmetrie hervorgerufen, was zu

einem Phasenübergang bei endlicher Temperatur führt, der wiederum mit einer Gitterverzerrung gekoppelt ist. Anders ausgedrückt muss die Spin-Entropie beim Abkühlen (teilweise) eingefroren werden, was bei Abwesenheit langreichweitiger magnetischer Ordnung nur über eine Verzerrung des Gitters möglich ist. Dieser Prozess weist einige Ähnlichkeiten zum klassischen Spin-Peierls-Übergang auf, bei dem die Ausbildung des Singulett-Zustands und die einhergehende Abnahme der Spin-Entropie ebenfalls durch eine Gitterverzerrung verursacht werden. Im vorliegenden Fall liegt im Bereich 0,3 K $\lesssim T \lesssim$ 1,5 K nur eine Entropie von wenigen Prozent von Rln 2 vor [5], das heißt, nur ein kleiner Bruchteil aller Spins ist an der Spinflüssigkeitsphase beteiligt. Bemerkenswert ist außerdem, dass die Form des Übergangs bei 6 K der Form derjenigen thermischen Ausdehnungsanomalie ähnelt, die mit dem Spin-Peierls-Übergang in den quasieindimensionalen organischen Leitern $(TMTTF)_2X$ (X = PF_6 oder AsF_6) verbunden ist.

Ein weiteres Phänomen von großem aktuellen Interesse auf dem Gebiet der stark korrelierten elektronischen Systeme ist die Ladungsordnung (CO). Der Phasenübergang zu einem ladungsgeordneten Zustand ist experimentell schon bei einer Reihe von Materialien beobachtet worden. Unter ihnen befindet sich die Familie der quasieindimensionalen organischen Ladungstransfersalze $(TMTTF)_2X$ [6]. Bemerkenswerterweise wurde die Existenz einer ladungsgeordneten Phase in $(TMTTF)_2X$ mit Hilfe der Molekularfeldnäherung im erweiterten Hubbard-Modell, also unter Berücksichtigung von *on-site* und *inter-site* Coulomb-Wechselwirkungen [7], schon theoretisch vorhersagt, als die experimentelle Bestätigung noch ausstand. Bislang fanden sich in der Literatur keinerlei Hinweise auf strukturelle Veränderungen als Folge der Ladungsordnung, weshalb der CO-Übergang in den $(TMTTF)_2X$-Salzen als "strukturloser" Phasenübergang, an dem nur Ladungsfreiheitsgrade beteiligt sind, bekannt wurde. Die erste Beobachtung von Gittereffekten am CO-Übergang und die sich daraus ergebene Erklärung für das Auftreten von Ferroelektrizität, stellt daher ein zweites wichtiges Ergebnis der vorliegenden Arbeit [8] dar. Sie weisen stark darauf hin, dass für die $(TMTTF)_2X$-Salze mit X = PF_6, AsF_6 und SbF_6 sowohl die Ladungs- als auch die Gitterfreiheitsgrade an diesem Übergang beteiligt sind . Darüber hinaus wird in dieser Arbeit der erste Nachweis eines weiteren Phasenübergangs bei der Temperatur $T_{int} = 0{,}6 \cdot T_{CO}$ in den Salzen mit X = PF_6 und AsF_6 vorgestellt, welcher aller Wahrscheinlichkeit nach mit dem Ladungsordnungsprozess in Beziehung steht.

Im Rahmen dieser Arbeit wurden auch Widerstandsmessungen unter hydrostatischem Druck unter Verwendung einer ^{4}He-Gasdruckzelle an der Verbindung $(CH_3)_{0,92}ReO_3$ durchgeführt. Diese Verbindung ist das erste Beispiel eines leitenden polymerischen Oxids. Der elektrische Widerstand verhält sich metallisch bis $T_{MI} \simeq 30$ K, wo ein Metall-Isolator Übergang stattfindet. Eine Altshuler-Aronov Korrektur basierend auf die Vorstellung eines Crossovers in der Diffusion von Ladungsträgern wurde von E.-W. Scheidt *et al.* vorgeschlagen, um den Metall-Isolator Übergang bei $T_{MI} \simeq 30$ K zu beschreiben. Die Ergebnisse von Widerstandmessungen für Drücke bis 1 kbar zeigen eine Abnahme des Widerstands im gesamten untersuchten Temperaturbereich, was auf eine Abnahme des Restwiderstandes hindeutet. Die Lage des Metall-Isolator-Übergangs bei $T_{MI} \simeq 30$ K bleibt hingegen unberührt.

Zusammenfassend sei gesagt, dass es auf dem Gebiet der stark korrelierten elektronischen Systeme eine schon lange währende Diskussion darüber gibt, ob die Gitterfreiheitsgrade eine Rolle für verschiedene physikalische Phänomene spielen, darunter der Mott-Metall-Isolator-Übergang und der Ladungsordnungs-Übergang. Die Ladungstransfersalze der κ-$(ET)_2X$- und der $(TMTTF)_2X$-Familie stellen in dieser Hinsicht Modellsysteme dar, erstere für die Erforschung von Korrelationseffekten in zwei Dimensionen, letztere entsprechend für eine Dimension. In der vorliegenden Arbeit wurden diese

Fragestellungen mit Hilfe hochaufgelöster Dilatometrie angegangen. Die hier diskutierten Ergebnisse offenbaren eine enge Verflechtung der Gitter- und elektronischen Freiheitsgrade sowohl beim Mott-Metall-Isolator-Übergang im vollständig deuterierten Salz κ-(D8-ET)$_2$Cu[N(CN)$_2$]Br als auch beim Ladungsordnungs-Übergang in der (TMTTF)$_2$X-Familie mit X = PF_6, AsF_6 und SbF_6.

Contents

Chapter 1

Introduction

The present work is dedicated mainly to the study of the thermal expansion of low-dimensional organic conductors. As a matter of fact, the phenomenon of thermal expansion in crystalline materials is a well-understood physical process [1]. The latter is predominantly dominated by the anharmonic vibrations of the lattice, which changes the interatomic distance as the temperature is increased or decreased and can in turn be observed at the macroscopic scale. For the organic charge-transfer salts investigated in the frame of this work, the interplay between spin, charge and lattice degrees of freedom defines the various ground states of these highly correlated one- or two-dimensional electronic systems and, due to their large expansivity, thermal expansion measurements have been revealed as a powerful experimental tool to obtain more insights into the physics of these materials. In this sense, given its high sensitivity, the experimental setup existent in the group of Prof. Dr. Michael Lang (Physics Institute - Goethe University - Frankfurt (M)) is an ideal experimental tool for studying the various electronic phases in organic conductors [2]. Charge-transfer salts of the κ-phase-(BEDT-TTF)$_2$X, here (BEDT-TTF) refers to (bisethylenedithio-tetrathiafulvalene), i.e. ($C_{10}S_8H_8$), and X to a monovalent anion, have been recognized as model systems to study electronic correlations in two-dimensions (2D). In particular, single crystals of fully deuterated salts of κ-(BEDT-TTF)$_2$Cu[N(CN)$_2$]Br, have been attracting interest due to their close proximity to the *S*-shaped first-order phase transition line in the phase diagram [3], which separates the metallic from the insulating state, thus enabling the Mott metal-insulator (MI) transition, one of the key topics in the field of strongly correlated electron systems, to be explored through temperature sweeps. One important result achieved in the frame of this work refers to the first experimental observation of the actual role of the lattice degrees of freedom for the Mott MI transition in the above-mentioned materials [4]. Both the discontinuity and the anisotropy of the lattice parameters observed via high-resolution thermal expansion experiments indicate an intricate role of the lattice degrees of freedom at the Mott transition for the present material which cannot be explained by a purely 2D electronic model. Furthermore, in the frame of the present work, a model based on the

rigid-unit modes scenario is proposed to describe the negative thermal expansion above the so-called glass like transition temperature $T_g \simeq 77\,\mathrm{K}$ in fully deuterated salts of κ-(BEDT-TTF)$_2$Cu[N(CN)$_2$]Br and parent compounds.

The compound κ-(BEDT-TTF)$_2$Cu$_2$(CN)$_3$ is another material of great interest in the last few years [5]. This system has an almost perfect quasi-2D frustrated triangular lattice, i.e. a ratio of hopping integrals of $t/t' \simeq 1$. No signature of long-order magnetic ordering has been observed down to low temperatures. Thus, this system has been recognized as a candidate for the realization of a spin-liquid. At T = 6 K, a crossover from a paramagnetic Mott insulating to a spin-liquid phase has been proposed in the literature. Nevertheless, the nature of the crossover/transition, also called *hidden ordering*, is still controversial. Thermal expansion performed on this material in the frame of the present work revealed a huge phase-transition-like-anomaly at T = 6 K, which coincides nicely with recent specific heat results reported in the literature. Our results provide strong evidences that this instability at T = 6 K is directly linked to the proposed spin-liquid phase.

Charge-ordering (CO) phenomena have been highly topical over the last few years. The phase transition towards a CO state was already observed experimentally in several materials. Found among them, is the family of quasi-one dimensional (quasi-1D) organic charge-transfer salt (TMTTF)$_2$X [6], where (TMTTF) stands for tetramethyltetrathiafulvalene and X for a monovalent anion (X = PF_6, AsF_6 and SbF_6). For the latter substances, the transition into the charge-ordered phase is accompanied by the onset of ferroelectricity. Interestingly enough, the existence of a charge-ordered phase in (TMTTF)$_2$X was predicted theoretically through mean-field calculations in the extended Hubbard model, i.e. taking into account the *on-site* and *inter-site* Coulomb interactions [7], before such experimental observations could be made. To date, no evidence of structural changes accompanying the charge ordering has been reported in the literature and, due to this, the CO transition in these substances has been known as a "*structureless*" phase transition. Due to the lack of structural changes it is believed that only charge degrees of freedom are involved in the CO transition. A second important result obtained in the present work concerns the first evidence for lattice effects at the CO transition, indicating that for the (TMTTF)$_2$X salt with X = PF_6, AsF_6 and SbF_6, both charge and lattice degrees of freedom should be involved in the CO transition [8]. In addition, the present work provides the first evidence of another phase transition at $T_{int} = 0.6 \cdot T_{CO}$ for the X = PF_6 and AsF_6 salts, which is likely to be related to the charge-ordering process.

Following this brief introduction which includes the first chapter, this thesis is subsequently divided into eight chapters, as follows:

- **Chapter 2**: this chapter is dedicated to a discussion on the basic theoretical aspects related to this work. Firstly, a discussion about the thermodynamic quantities used in this work is presented, followed by a discussion of the main characteristics of first- and second-order transitions and critical behavior. The basic concepts about the physics of low-dimensional systems, organic conductors and electronic correlation effects are then introduced. The chapter ends with a discussion on the Mott MI transition.

- **Chapter 3**: here the experimental methods and techniques, i.e. high-resolution dilatometry employing the capacitive method and resistivity under ambient and high pressures employing a ^{4}He-gas pressure cell are discussed. Details of the

measurement procedures and data analysis are also presented.

- **Chapter 4**: sample preparation, the existent phases, crystal structures, pressure-temperature phase diagram and state of the art of the (BEDT-TTF)$_2$X based organic conductors are introduced, followed by the main results which have been obtained from the above-mentioned organic conductors. High-resolution thermal expansion experiments on the fully deuterated compound with the anion X = Cu[N(CN)$_2$]Br and the system with X = Cu$_2$(CN)$_3$ are discussed in detail. This chapter embodies part of the main results of this thesis.

- **Chapter 5**: this chapter is dedicated to the quasi-1D (TMTTF)$_2$X with X = PF_6, AsF_6 and SbF_6 charge-transfer salts. Firstly, the crystal structure and the generalized phase diagram are discussed. This is followed by a discussion of selected literature results related to the CO phase transition. The chapter ends with a detailed discussion of the thermal expansion results for the present organic conductors. This chapter incorporates another important part of this thesis.

- **Chapter 6**: in this chapter, the polymeric methyltrioxorhenium $(CH_3)_{0.92}ReO_3$ compound, abbreviated to (poly-MTO), is discussed. Crystalline structure, literature results and resistivity measurements under ambient and high pressures carried out on this compound are discussed.

- **Chapter 7**: in this chapter main results and conclusions of the project are summarized.

- **Chapter 8**: perspectives and an outlook are presented here.

Chapter 2

Basic Theoretical Features

In this chapter, a brief discussion about the thermodynamic quantities used in this work is given. Definitions of the nature and classification of phase transitions, as well as critical behavior of thermodynamic physical quantities in second-order phase transitions are presented. A background on the ground states and phase transitions encountered in the phase diagram of the organic conductors studied in the frame of this work is also given.

2.1 Thermal Expansion and Thermodynamic Quantities

Thermal expansion at constant pressure quantifies the temperature (T) dependence of the sample volume (V). Upon increase or decrease of the temperature in the vicinity of a generic phase transition, which might have its origin in magnetic or electronic effects, but should be accompanied by some structural effects, the harmonic approximation is no longer valid and the crystal expands or contracts until it finds the volume where the total free energy is minimized. In this sense, high-resolution measurements of the thermal expansion coefficient can be seen as a powerful thermodynamic experimental tool for detecting phase transitions, since phase transitions of different natures can be observed by using this method. The volumetric thermal expansion coefficient of a solid is given by:

$$\beta(T) = \frac{1}{V}\Big(\frac{\partial V}{\partial T}\Big)_P \tag{2.1}$$

where,

$$\beta(T) = \alpha_a(T) + \alpha_b(T) + \alpha_c(T) \tag{2.2}$$

and α_i is the linear thermal expansion coefficient along the *i* = *a*, *b* and *c* crystal directions. Eq. 2.2 holds for all lattice symmetries if *a*, *b* and *c* are perpendicular to each other [1]. The linear thermal expansion coefficient at constant P reads:

$$\alpha_i = \frac{1}{l}\Big(\frac{\partial l(T)}{\partial T}\Big)_P \tag{2.3}$$

where *l* is the sample length. The physical quantity described by Eq. 2.3 will be frequently used in this work.

The isothermal compressibility of a solid is defined as follows:

$$\kappa_T = -\frac{1}{V}\Big(\frac{\partial V}{\partial P}\Big)_T \tag{2.4}$$

In order to make a link between the volumetric thermal expansion coefficient of a solid and the isothermal compressibility, Eq. 2.1 can be rewritten in the following way:

$$\beta(T) = -\frac{1}{V}\frac{\partial V}{\partial P}\Big|_T \cdot \frac{\partial P}{\partial T}\Big|_V = \kappa_T \frac{\partial P}{\partial T}\Big|_V \tag{2.5}$$

The volumetric thermal expansion coefficient can still be linked with the entropy (S) of the system. To this end, it is useful to work with the Helmholtz free energy $F(V,T)$, defined as follows:

$$F = U - TS \tag{2.6}$$

where U refers to the internal free energy of the system. Making the partial derivatives of Eq. 2.6, one obtains:

$$\frac{\partial F}{\partial T}\Big|_V = -S \tag{2.7}$$

$$\frac{\partial F}{\partial V}\Big|_T = -P \tag{2.8}$$

Leading Eq. 2.8 into Eq. 2.5 results in:

$$\beta = -\frac{1}{V}\frac{\partial V}{\partial P}\Big|_T \Big[\frac{\partial}{\partial T}\cdot\Big(-\frac{\partial F}{\partial V}\Big)\Big|_T\Big]\Big|_V \tag{2.9}$$

Making the derivative of the above equation and substituting Eqs. 2.4 and 2.7, results in:

$$\beta(T) = -\kappa_T \frac{\partial^2 F}{\partial T \partial V} = \kappa_T \frac{\partial S}{\partial V}\Big|_T \tag{2.10}$$

Eq. 2.10 shows the direct connection of the volumetric thermal expansion coefficient to the volume dependence of the entropy. In the following, the volumetric thermal expansion coefficient will be related to the specific heat, which is defined as the amount of heat Q necessary to increase the temperature of the sample, as follows:

$$C(T) = \frac{\Delta Q}{\Delta T} \tag{2.11}$$

In terms of the Helmholtz free energy, the specific heat at constant volume is defined by:

$$C_V(T) = -T\frac{\partial^2 F}{\partial T^2}\Big|_V = T\frac{\partial S}{\partial T}\Big|_V \tag{2.12}$$

Rewriting Eq. 2.10, one has:

$$\beta(T) = -\kappa_T \frac{\partial S}{\partial T}\Big|_V \cdot \frac{\partial T}{\partial V}\Big|_S \tag{2.13}$$

Substituting the last part of Eq. 2.12 in Eq. 2.13 and using $(V/T)\cdot\partial T/\partial V = \partial \ln T/\partial \ln V$ the desired relation between $C_V(T)$ and $\beta(T)$ is, therefore, achieved:

$$\beta(T) = -\kappa_T \cdot C_V(T) \cdot \frac{1}{V} \cdot \frac{\partial \ln T}{\partial \ln V}\Big|_S \tag{2.14}$$

Defining a new quantity

$$\Gamma = -\frac{\partial \ln T}{\partial \ln V}\Big|_S \tag{2.15}$$

Eq. 2.14 becomes

$$\beta(T) = \Gamma_{eff} \cdot \frac{\kappa_T}{V_{mol}} \cdot C_V(T) \tag{2.16}$$

The latter equation is called Grüneisen-Relation [9], where V_{mol} stands for the molar volume and Γ_{eff} is the effective Grüneisen parameter. In general, $\Gamma_{eff}\cdot\kappa_T/V_{mol}$ is slightly temperature dependent. In the Debye-model, the lattice (or phononic) Grüneisen parameter Γ_{pho} is given by:

$$\Gamma_{pho} = -\frac{d \ln \Theta_D}{d \ln V}, \tag{2.17}$$

where Θ_D stands for the Debye temperature. According to Eq. 2.17, the bigger the lattice Grüneisen parameter, the higher the volume dependence of the vibration modes of

the lattice. Strictly speaking, the lattice Grüneisen parameter is a measure of the volume dependence of the anharmonicity of the lattice vibrations, which in turn is responsible for the lattice contribution to the thermal expansion in a solid. The vibrational free energy, entropy, specific heat and thermal expansion result from sums of contributions f_i, s_i, c_i and α_i from independent vibration modes of frequency $\omega_i(V)$, respectively. Hence, the mode Grüneisen parameter is defined in the following way:

$$\Gamma_i = -\frac{d\ln\omega_i}{d\ln V} \tag{2.18}$$

Thus, according to Eq. 2.18, vibration modes whose frequency, ω_i, decreases or *softens* as the volume of the solid decreases will result in a negative Grüneisen parameter and, from Eq. 2.16, such soft modes will be responsible for a negative contribution to the overall thermal expansion of the material [10].

More generally, in addition to the phonon background contribution to the thermal expansion of a material, other contributions, whose origin might be electronic or magnetic, have to be taken into account. This is the case especially at low temperatures, where such contributions may dominate the thermodynamic properties [1]. Hence, the total volumetric thermal expansion coefficient reads:

$$\beta = \beta_{ph} + \beta_{el} + \beta_{mag} = \frac{\kappa_T}{V_{mol}}(\Gamma_{ph}C_{ph} + \Gamma_{el}C_{el} + \Gamma_{mag}C_{mag}), \tag{2.19}$$

where β_{ph} (C_{ph}), β_{el} (C_{el}) and β_{mag} (C_{mag}) refer to the phononic, electronic and magnetic contributions to β (C), respectively, while Γ_{ph}, Γ_{el} and Γ_{mag} are the respective Grüneisen parameters.

If the Grüneisen parameter, which, as above discussed, measures the volume dependence of a characteristic temperature, is assumed to be constant and in the temperature range of interest one of these contributions is predominant, then the same temperature dependence for $C_V(T)$ and $\beta(T)$ should be expected. This is the reason why critical exponents can be obtained via thermal expansion measurements. For the critical temperature of the superconducting transition in the κ-(BEDT-TTF)$_2$Cu(NCS)$_2$ charge-transfer salt $\Gamma \approx 40$ is obtained [11], a value which roughly exceeds by a factor of twenty those obtained for ordinary superconductors such as in Pb, with a Γ = 2.4 [12] or even bigger than those obtained for the layered cuprate $YBa_2Cu_3O_7$ with Γ = (0.36 $\sim$ 0.6) [13]. These findings reveal the high sensitivity of the transition temperature to the pressure in the family of κ-(ET)$_2$X, as discussed in more detail in Ref. [14].

The very basic theoretical aspects related to phase transitions, necessary to understand the results to be discussed in this work, is the topic of the next section.

2.2 Phase Transitions (Basic)

The main focus of this section is to discuss the main differences between first- and second-order phase transitions, due to the fact that frequently it is very difficult to distinguish them in real systems. Before doing so, it is adequate to start with a general discussion about phase transitions. In fact, phase transitions are present in our daily lives. Heating of water, i.e. boiling, for making a tea or placing a form with water in a refrigerator in order to make ice means, from the physical point of view, that we are

changing the state of the matter by changing the temperature. In the same way, phase transitions are observed every day in the metallurgic industry, for instance, where solid iron is heated until it becomes liquid (usually over $\sim 1000^0$C), then mixed with certain amounts of carbon in order to obtain steels. For the materials studied in this work, the understanding of the nature of the metal-to-superconductor and the Mott MI transitions in fully hydrogenated and deuterated salts of the κ-(BEDT-TTF)$_2$Cu[N(CN)$_2$]Br organic conductor, respectively, as well as the understanding of the CO transition in (TMTTF)$_2$X (with X=PF_6, AsF_6 and SbF_6) constitute attractive current topics of research. Hence, understanding the nature of the phase transitions is a very important issue in solid state physics research. As a matter of fact, classification of phase transitions is usually intensively discussed and can be found in the text books, see e.g. [15,16]. Figs. 2.1 a) - f) depict a schematic change of the Gibbs free energy (G), entropy (S) and specific heat[1] (C_p) for a first- and second-order phase transition. According to the Ehrenfest classification, a first-order transition is characterized by a discontinuity of the entropy of the system at the transition temperature T_c upon going from a hypothetical phase 1 to phase 2. As can be seen from Fig. 2.1 a), the two phases coexist at T_c, so that the transition takes place right on the crossing of the Gibbs free energy of both phases, which are represented by straight lines with different slopes. Since the specific heat and thermal-expansion coefficient are proportional to the first derivative of the entropy of the system, this implies a discontinuity or divergence in these quantities. This is shown schematically in Fig. 2.1 c). In contrast to a first-order phase transition, a second-order phase transition, is characterized by a continuous change of the entropy of the system upon going from one phase to the other, as schematically shown in Fig. 2.1 e). Depending on the nature of the transition, this continuous change of the entropy can be observed in a broadening and/or rounding of the phase transition, cf. Fig. 2.1 f). Nevertheless, as mentioned in the introduction of this section, in practice it is sometimes difficult to distinguish a first- from a second-order phase transition for real materials, as the specific heat and thermal expansion may present distinct behaviors from those discussed above. Usually, for a first-order transition instead of a divergent behavior (Fig. 2.1 c)) the transition is accompanied by broadening effects, which in many cases have their origin in the inhomogeneities or impurities of the crystal. In the case of second-order phase transition, there are two particular cases: i) the so-called λ-transition, where the shape of $C_p(T)$ diverges and has some resemblance with the Greek letter λ, being the transition from normal to superfluid in ^{4}He one of the most prominent examples of λ-transitions; ii) mean-field-like behavior, characterized by a step-like discontinuity in the specific heat. In summary, there are materials such as elementary superconductors in the absence of external magnetic field, in which a mean-field-like transition takes place, while in other materials, like the organic conductors[2] studied in this work, transitions roughly similar to those sketched in Fig. 2.1 f) can be observed.

In the following, a generalization of the first-order transitions is made through the deduction of the Clausius-Clapeyron equation. The Gibbs free energy reads:

$$G(P,T,M) = U + PV - TS - MH \tag{2.20}$$

where M and H refer to magnetization and magnetic field, respectively. These terms

[1] The specific heat at constant pressure, i.e. (C_p), is used intentionally here because C_p is the quantity accessible experimentally. The difference between C_p and C_V is given by $(C_p - C_V) = T \cdot V_{mol} \cdot \beta^2 / \kappa_T$.

[2] For a comparison between experimental specific heat data and theoretical prediction by BCS theory for the κ-(BEDT-TTF)$_2$Cu(NCS)$_2$ salt at the superconducing transition, see Ref. [2], Fig. 6.34, p. 205.

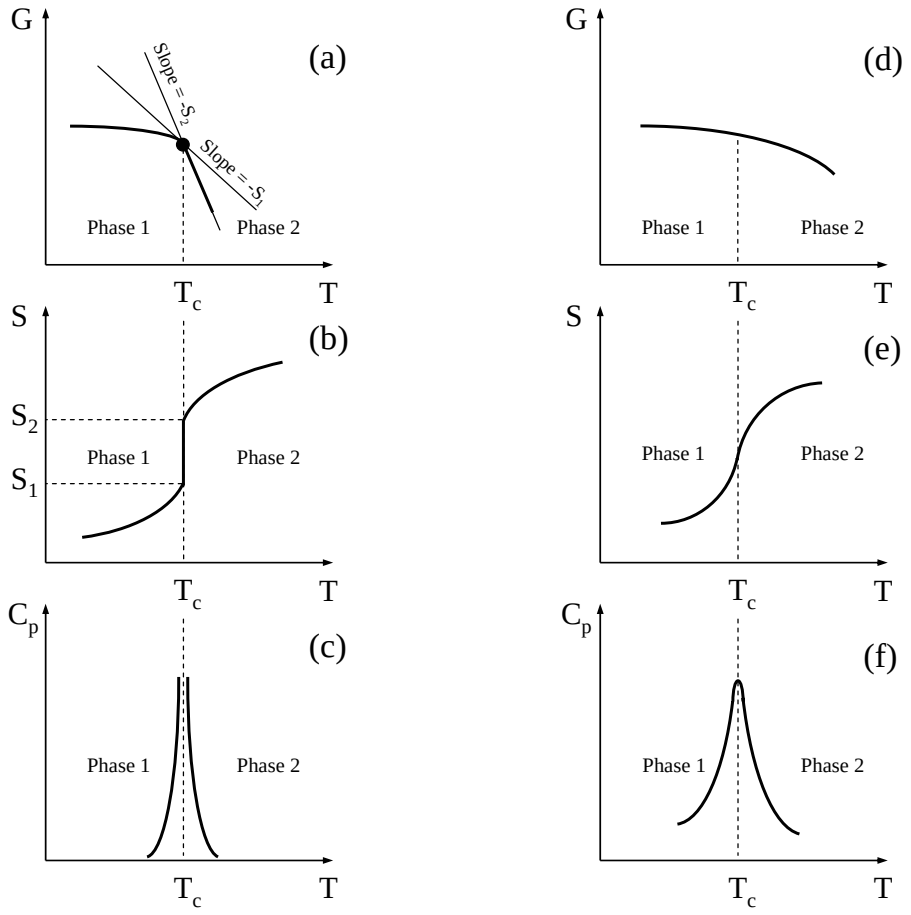

Figure 2.1: Schematic representation of the Gibbs free energy (G), entropy (S) and specific heat (C_p) as a function of temperature for - a), b) and c), first-order and - d), e) and f), second-order phase transition. T_c indicates the transition temperature. In a) different slopes of the free energy (straight lines) indicate the entropy associated with the different phases, the bullet marks the crossing of these two lines at the transition temperature T_c. Details are discussed in the text.

are only relevant if one is dealing with a magnetic system.

In a first-order transition a discontinuity in $G(P, T, M)$ is expected, therefore, a jump in the volume of the solid should be observed. Hence, making the partial derivative of Eq. 2.20 with respect to P, one obtains:

$$V = \left(\frac{\partial G}{\partial P}\right)_{T,H} \tag{2.21}$$

The volume change on passing from phase 1 to phase 2 is given by:

$$\Delta V = V_2 - V_1 = \frac{\partial G}{\partial P}\Big|_T^2 - \frac{\partial G}{\partial P}\Big|_T^1 \tag{2.22}$$

which can be interpreted as a discontinuity in the entropy, which is given by:

$$\Delta S = S_2 - S_1 = \frac{\partial G}{\partial T}\Big|_P^2 - \frac{\partial G}{\partial T}\Big|_P^1 \tag{2.23}$$

At the transition point (closed circle in Fig. 2.1 a)) the Gibbs free energy is the same for both phases. This means that right at the transition temperature, the chemical potential (μ) should be the same for both phases. However, a small change in the temperature reflects a change in the chemical potential of the two phases, as follows:

$$\mu_1 + d\mu_1 = \mu_2 + d\mu_2 \Rightarrow d\mu_1 = d\mu_2 = V_1 dP_1 - TdS_1 = V_2 dP_2 - TdS_2 \tag{2.24}$$

Rearranging the last part of Eq. 2.24, making $S_2 - S_1 = \Delta S$ and $V_2 - V_1 = \Delta V$, the Clausius-Clapeyron equation is finally deduced:

$$\frac{dT_c}{dP} = \frac{\Delta V}{\Delta S} \tag{2.25}$$

The latter equation will be employed in the Section 4.6.2 to estimate the entropy change associated with the Mott MI transition. A finite entropy difference between the two phases corresponds to the amount of latent heat $L = T \cdot \Delta S$, which gives rise to the presence of hysteresis in a first-order phase transition upon warming and cooling the system through T_c.
Based on similar arguments to those discussed above, a relation which makes the connection between the uniaxial-pressure dependence of the critical temperature for pressure applied along the i-axis and the anomalies at T_c in the thermal expansion coefficient and specific heat for a second-order phase transition can be deduced. This relation is called Ehrenfest relation and it is given by:

$$\left(\frac{dT_c}{dP_i}\right)_{P_i \to 0} = V_{mol} \cdot T_c \cdot \frac{\Delta \alpha_i}{\Delta C} \tag{2.26}$$

where $\Delta\alpha_i$ and ΔC refer to the thermal expansion and specific heat changes at the transition temperature, respectively. The index i refers to the crystallographic direction, along which pressure is applied. Strictly speaking, the Ehrenfest relation is valid only for mean-field-like phase transition, where $\Delta\alpha$ and ΔC present step-like behavior.
Another approach for second-order transitions has been proposed by L.D. Landau in a phenomenological theory, of which more details can be found in Ref. [17], see Chapter XIV. The assumption of the existence of an order parameter is the basis of his theory, where the free energy is assumed to be a function of this quantity. The order parameter is an observable and it is the only physical quantity which describes the behavior of a system near the critical temperature of a second-order phase transition. As its name suggests, it measures the amount and kind of ordering around T_c, vanishing continuously

above T_c and having a finite value below T_c[3]. The order parameters for several phase transitions are presented in Table 2.1.

Phase Transition	Order Parameter
Liquid-gas	ρ - ρ_c
Ferromagnetic	Magnetization **M**
Antiferromagnetic	Staggered **M**
Ferroelectricity	Lattice Polarization
Phase Separation	Concentration
Superconductivity	Complex Gap Parameter Δ
Superfluidity	Macroscopic Wave Function Ψ
Spin-Glass	Measure of the temporal spin freezing
Spin-Peierls	Structural Distortion
Charge-Ordering	Splitting of the NMR spectra

Table 2.1: List of several phase transitions and their respective order parameters. Here ρ refers to the liquid density and ρ_c to the critical density in a liquid-to-gas transition.

2.3 Critical Behavior and Universality Classes

Second-order phase transitions are separated in defined groups, usually called universality classes. The latter enable us to classify phase transitions in different systems, as will be discussed in more detail below. In real materials, upon approaching the critical temperature, fluctuations are no longer negligible. Such fluctuations can be viewed as an energetic rearrangement of the system to stay in the current phase. The more the critical temperature is approached, the stronger are the fluctuations. This happens until the new phase dominates the physical properties and the phase transition takes place. The transition is, in many cases, accompanied by broadening effects due to crystal defects or inhomogeneities. This feature will be discussed in Section 4.7 in the analysis of the phase transition at the critical end point of the first-order line in fully deuterated salts of κ-(BEDT-TTF)$_2$Cu[N(CN)$_2$]Br. Amazingly, around T_c some physical quantities tend to obey power laws in the variable $t = |(T - T_c)/T_c|$ which measures the relative distance to the transition temperature. For example, when water turns to steam at a critical pressure, its specific heat as a function of temperature has exactly the same power-law dependence as that of iron when it is demagnetized by having its temperature increased. These power laws characterize the universality classes and are described by the so-called critical-exponents, as follows:

$$C_p^+(T) \sim A^+ \frac{|t|^{-\tilde{\alpha}}}{\tilde{\alpha}}, t > 0.^4 \tag{2.27}$$

$$C_p^-(T) \sim A^- \frac{|t|^{-\tilde{\alpha}}}{\tilde{\alpha}}, t < 0 \tag{2.28}$$

$$M_S(T) \sim B|t|^{\beta}, t < 0 \tag{2.29}$$

[3] A detailed discussion is given also e.g. in Refs. [15,18].

[4] Usually, α is used in the literature to refer to the specific heat critical exponent. In order to avoid any confusion with the linear thermal expansion coefficient $\alpha(T)$ here $\tilde{\alpha}$ is used to refer to the specific heat critical exponent.

$$\chi(T) \sim C|t|^{-\gamma}, t > 0 \tag{2.30}$$

$$M(H) \sim DH^{1/\delta}, t = 0 \tag{2.31}$$

$$\tilde{\alpha} + 2\beta + \gamma = 2.^{5} \tag{2.32}$$

$$\gamma = \beta(\delta - 1) \tag{2.33}$$

Where $t \equiv |(T - T_c)/T_c|$ is the reduced temperature and A^+, A^-, B, C and D are constants. $C_p(T)$, $M_s(T)$ and $\chi(T)$ refer to the specific heat at constant pressure, spontaneous magnetization ($M_s \equiv M(H = 0)$) and magnetic susceptibility, respectively. Eqs. 2.32 and 2.33 give the relation between the critical exponents.

It is striking to note that in the study of the critical behavior of a second-order transition, materials displaying completely different crystal structures as well as quite different subsystems obey the same critical behavior at T_c, giving rise thus to the universality classes. The theoretical values for the critical exponents of different universality classes accompanied by an example of phase transition are listed in Table 2.2.

Model	$\tilde{\alpha}$	β	γ	δ	**Proposed examples of phase transition**
Mean-field	0	0.5	1.0	3.0	Mott MI transition in $(V_{1-x}Cr_x)_2O_3$ [19]
2D Ising	0	0.125	1.75	15	"Preroughening transition" in GaAs [20]
3D XY	0	0.35	1.3	4.80	Superconducting transition in $YBa_2Cu_3O_{7-\delta}$ [21]
3D Heisenberg	-0.115	0.365	1.24	4.82	-
Unconventional Criticality	-1	1	1	2	Mott MI transition in κ-(BEDT-TTF)$_2$Cu[N(CN)$_2$]Cl [22]

Table 2.2: Theoretical models with their respective critical exponents, accompanied by proposed example of phase transition.

From the experimental point of view, the estimate of the critical exponent is a hard task. For instance, owing to the specific heat critical exponent $\tilde{\alpha}$, a reliable estimate of the phonon background is one of the crucial points. In addition, for a reliable estimate of the critical behavior of a system, fine measurements close to T_c ($t \lesssim 10^{-3}$) are necessary. However, for real materials, a broadening of the transition due to inhomogeneities (impurities or crystal defects) is frequently observed in this region. Due to this, T_c cannot be measured directly, but rather it is obtained indirectly via self consistent fittings. Recently, in a stimulating article entitled "Unconventional Critical Behaviour in a Quasi-2D Organic Conductor" published in Nature (Ref. [22]), F. Kagawa and collaborators reported on the criticality at the pressure-induced Mott transition in the organic κ-(BEDT-TTF)$_2$Cu[N(CN)$_2$]Cl charge-transfer salt. In this study, the authors made

[5] This relation is frequently called universal or Rushbrooke relation [15].

use of the isothermal pressure-sweep technique[6], using Helium as a pressure transmitting medium, to explore the critical behavior of this organic salt through conductance measurements. The critical behavior of the conductance data at the critical endpoint was analyzed in the framework of the scaling theory of the liquid-gas transition [18]. More strictly speaking, pressure and temperature were used as the scaling variables (the so-called non-mixing approximation), h and ε, to obtain the critical exponents (δ, β, γ) listed in Table 2.2. Substituting these values in the Rushbrooke relation one obtains $\tilde{\alpha}$ = -1. As pointed out by the authors, the obtained critical exponents do not fit in the known universality classes, indicating the discovery of a new criticality class. As will be discussed in Section 4.7, the Mott criticality of the fully deuterated salt of κ-(BEDT-TTF)$_2$Cu[N(CN)$_2$]Br was studied by means of thermal expansion measurements assuming the proportionality of this quantity to the specific heat, cf. Eq. 2.16. The specific heat critical exponent $\tilde{\alpha}$ obtained via thermodynamic measurements markedly deviates from the *unconventional criticality* claimed by Kagawa and collaborators. Possible explanations for this discrepancy will be also presented in Section 4.7.

2.4 Physics in Low Dimensions and Organic Conductors

The understanding of the macroscopic physical properties of solids, like specific heat, electrical and thermal conductivity, magnetism and superconductivity is directly related to the understanding of the electrons' behavior in this state of matter. Since the discovery of its fundamental charge by Millikan through his wonderful "oil drop experiment", followed by the discovery of the electron's spin by Stern and Gerlach here in Frankfurt (M), the study of this tiny particle and its interactions have been the subject of ongoing intensive research. Interestingly enough, many of the electronic properties of solids are not observed in three dimensional systems, but are intrinsic to systems with reduced dimensionality, the so-called low-dimensional systems. The term "low-dimensional systems" here refers to materials, which present strong anisotropy in the electrical conductivity. This is because their lattice structures resemble chains (one-dimensional (1D)) or layers (two-dimensional (2D)). In fact, a real 1D-system (quasi-1D), has always a finite interchain coupling, whereas a real 2D system (quasi-2D), in turn consists of planes with a weak interplane coupling. Interest in studying quasi-1D molecular materials arose after publication of Little's work [23]. In this article it is predicted that properly designed quasi-1D systems would be the promising materials for the realization of superconductivity at high temperatures. According to Little, the pairing of electrons via their coupling to highly polarisable side-chains in organic materials should result in superconductors with critical temperatures T_c above room temperature, to date unfortunately still not observed. Furthermore, 1D systems are interesting because they offer a perfect scenario for studying electronic correlation effects theoretically. The low dimensionality makes it possible for such systems to be included in the class of problems which can be solved exactly according to theory. Several theoretical 1D models with short-range order, including the isotropic Heisenberg model and Hubbard model in 1D, can be treated exactly using the Bethe-Ansatz [24]. Another important issue in low dimensions is that quantum fluctuations are important and, due to this, long-range order is destroyed. In general, the stability of an ordered phase is threaded to the reduction of the dimensionality [15]. The character of the fluctuations in 1D is directly related to the absence of

[6] As a matter of fact, the critical behavior at the Mott critical endpoint was already studied previously using the same approach by P. Limelette and collaborators [19] on Cr-doped $(V_{1-x}Cr_x)_2O_3$, which is recognized as the canonical Mott insulator system.

long-range order at finite temperatures in systems with short-range interactions, as first pointed out by Landau [17] and later by Mermin and Wagner [25]. The reason for this is that the stability of a phase, in general, depends directly on the dispute between ordering and disordering. On the one hand, in a ferromagnetic system, for instance, the division of the system in different regions in which the order parameter assumes a fixed value is, from the energy point of view, unfavorable due to the formation of domain walls. On the other hand, the above-mentioned division is, from the entropy point of view, favorable since the number of microscopic configurations is increased. However, if the dimension of the system is increased, the problem cannot exactly be solved theoretically. The Landau Fermi-liquid (FL) [26] theory for electrons in 3D is, up to date, the most successful theory to describe the metallic state at low temperatures, where a $R(T)$ $\sim T^2$ behavior of the resistivity is expected. In the latter theory, the renormalization of some parameters, such as mass, gives rise to the concept of the quasi-particles. The latter incorporate the main information of the interacting many-body system and can be visualized as charged particles which are surrounded by a distorted charge distribution. The FL theory describes satisfactorily the majority of metals in 3D, but fails in the case of 1D. A theoretical description of the behavior of electrons in 1D was presented firstly by Luttinger [27]. One of the most interesting features in the Luttinger's model, usually called Tomonaga-Luttinger Liquid (TLL), is that fluctuations of charge and spin density can behave independently, i.e. in the frame of the TLL model spin-charge separation is predicted. Although several evidences in favor of Luttinger's model have been reported in the literature, see e.g. [28, 29], a generally accepted experimental proof of the TLL is still lacking. Some particularities of the electron gas in 1D are discussed below.

2.4.1 Instabilities of the Electron Gas in 1D

It is well known from the literature that electron-phonon interaction in quasi-1D conductors can induce two distinct kinds of transitions: i) the Peierls phase transition [30], which is the MI transition accompanied by a characteristic modulation of the electronic density, also called "charge-density wave" (CDW) transition or ii) a spin-density wave (SDW) transition, which in turn is characterized by a periodic modulation of the spin density [31]. In fact, the Peierls transition is a direct consequence of the strong coupling between vibrational modes of the lattice and electrons in the vicinity of the Fermi energy level, provoking thus the instability of the electron gas in 1D. This can be better understood by analyzing the shape of the Fermi surface (FS) in different dimensions. A schematic representation of the shape of the FS for different dimensionality is shown in Fig. 2.2. As the figure demonstrates, the FS in 1D presents a peculiarity, it consists of two parallel sheets separated by the wave-vector $\mathbf{Q}$ = ($2k_F$, 0, 0) resulting in a perfect nesting[7]. Note that for the quasi-1D case, due to the weak interchain coupling, the FS is slightly warped and the nesting becomes less effective. In contrast to a 1D system, however, in a 2D system, the FS is a closed cylinder, disfavorable for nesting. For this reason, the metallic state is stable down to low temperatures in such systems, while for a three-dimensional system its shape is spherical.

Experimentally, a CDW transition can be detected by means of X-ray diffraction experiments [33]. The presence of a superstructure associated with the CDW gives rise to an additional periodicity in the diffraction pattern, referred to as satellite reflections.

[7]Perfect nesting of the Fermi surface means that the dispersion energy $E_k = E_{k+Q}$ for all wave-vectors k on the Fermi surface. In other words, this means that all the sites which differ by $\mathbf{Q}$ = ($2k_F$, 0, 0) have the same energy and as a consequence the FS can be mapped onto itself by the translation of the $2k_F$ wave-vector.

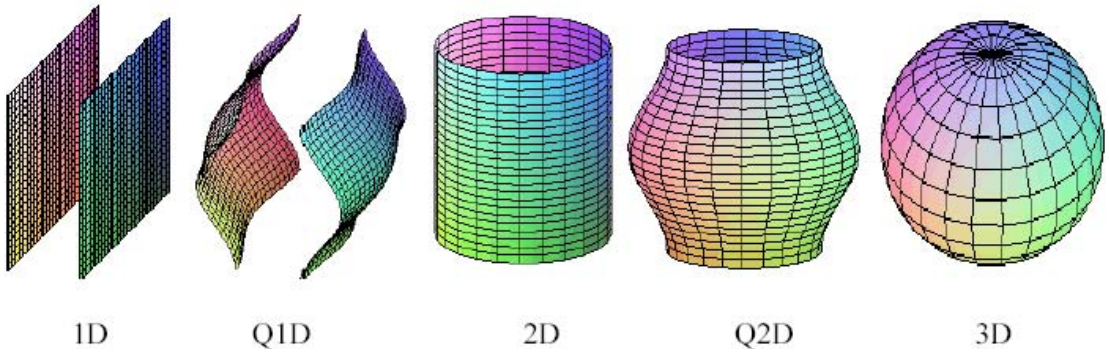

Figure 2.2: By changing the dimensionality of the system, the Fermi surface assumes different topologies. Here 1D refers to one-dimensional, Q1D to quasi-one-dimensional, 2D to two-dimensional, Q2D to quasi-two-dimensional and 3D to three-dimensional. Picture taken from Ref. [32].

Unlike a CDW transition, the SDW transition is not accompanied by lattice distortion, so that X-ray experiments fail to detect it. Hence, to detect a SDW transition experimentally another method should be employed. In the case of the quasi-1D $(TMTSF)_2X$ salts with X = PF_6, for example, NMR experiments are adequate for this task. The spatial variation of the spin density leads to a spatial variation of the internal field at the nuclear sites, which below the transition temperature changes the resonance line.

2.4.2 Low-Dimensional Organic Conductors

Based on the previous section, it is interesting to note that depending on the dimensionality as well as intensity of the electron-electron and/or electron-phonon or even spin-phonon interactions, the system can assume distinct ground states. But, in which materials can such dimensionality effects be observed? The study of the physical properties of low-dimensional systems in real materials still presents a challenge and is a fascinating field of research. Among materials in which such properties can be observed are organic conductors. This class of materials can be viewed as an actual *playground* for both experimentalists and theoreticians, see, e.g. [2] for a recent review. In the field of organic conductors, the most prominent examples of quasi-1D systems are $(TMTTF)_2X$ (Fabre-salts) and $(TMTSF)_2X$ (Bechgaard-salts), where TMTTF, TMTSF and X, denote tetramethyltetrathiafulvalene, tetramethyltetraselenafulvalene and a monovalent anion (X = PF_6, AsF_6, SbF_6, ClO_4, Br, etc), respectively. This family is usually referred to as Fabre-Bechgaard salts, in honor of the scientists J.M. Fabre and K. Bechgaard, who were the first to synthesize these materials. Concerning the structure, in the Fabre-Bechgaard salts, the donor molecules (TMTTF or TMTSF) are arranged in a certain fashion so that they form weakly interacting stacks (quasi-1D structure), favoring the formation of nesting, thus leading the system to an insulating state. By applying a pressure of 6.5 kbar on the compound $(TMTSF)_2PF_6$, D. Jérome and collaborators suppressed the SDW state and observed, for the first time, superconductivity (T_c = 1.2 K) in an organic compound. This was in the year 1980 and can be seen as a landmark in the history of organic conductors. Hence, in order to achieve a superconducting state at higher temperatures, the dimensionality of the system should be increased to avoid the nesting of the FS. According to this idea, the first organic compound based on the donor molecule BEDT-TTF which stands for (bis(ethylenedithio)-tetrathiofulvalene) was synthesized. In this new generation of organic conductors, the above-mentioned face-to-face stacking of the

Fabre-Bechgaard salts is exchanged by a strong side-by-side overlap between π-orbitals of neighboring (BEDT-TTF) molecules. The physical properties of κ-(BEDT-TTF)$_2$X and (TMTTF)$_2$X based charge-transfer salts will be discussed in Chapters 4 and 5, respectively. In the following, the mechanism responsible for the metallic behavior of organic conductor studied here is discussed.

2.4.3 Electronic Transport in Organic Conductors

The generation of charge carriers together with their displacement throughout the crystal are the two requirements which should be fulfilled to obtain metallic conductivity.

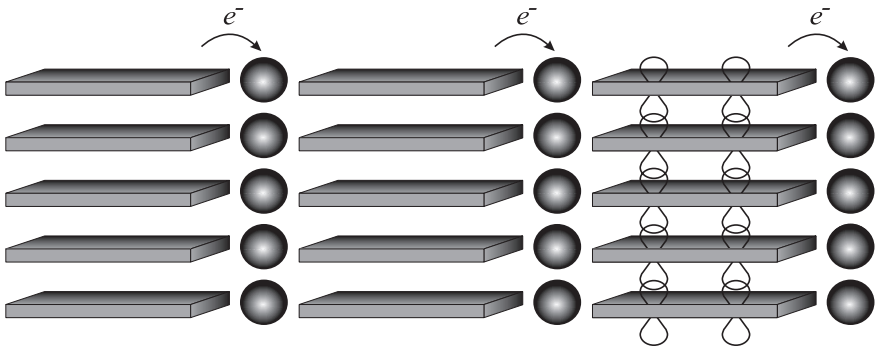

Figure 2.3: Schematic representation of the charge-transfer process for a AD (one donor molecule D and one acceptor molecule A) type generic organic conductor. In this example, plates represent stacked planar donor molecules, which are separated by chains of anions (balls). The intermolecular π-orbital overlap between the donor molecules is represented on the right side. Picture taken from Ref. [34].

In the case of the organic materials investigated in this work, these two requirements are achieved by means of the so-called charge-transfer process. Fig. 2.3 demonstrates schematically the charge-transfer process for a hypothetical organic conductor. In this process, a donor molecule - for the organic conductors studied in this work one has two-donor molecules of (BEDT-TTF) or (TMTTF) (to be discussed in Chapters 4 and 5, respectively) - transfers one electron to the counter ion. For this the donor molecule should have a low ionization energy and the counter anion the appropriate electronic affinity, so that the former can be easily oxidized by the latter. Hence, based on this charge-transfer process, depending on the constitute atoms of the counter ion it can adopt a closed-shell configuration and, as a consequence, a hole is left in the pair of donor molecules. Due to the dense crystalline packing, during the process of formation of the solid, an overlap of the molecular orbitals of neighboring molecules occurs, cf. shown on the right side of Fig. 2.3, and charge carriers become delocalized giving rise to metallic conductivity. In the case of organic conductors of the κ-(BEDT-TTF)$_2$X family, the conduction band originates from the overlap of the π-electron orbitals of the (BEDT-TTF) aromatic rings, which form a conduction band, resulting in a quasi-2D electronic structure. The dimerization leads to a half-filled conduction band or, strictly speaking, each dimer donates one electron to the counter ion, remaining thus on average +0.5e per (BEDT-TTF) molecule. Consequently, the conductance band is partly filled and the material is a metal. The room-temperature conductivity of the quasi-2D κ-(BEDT-TTF)$_2$Cu[N(CN)$_2$]Br salt is of about 50 Ω^{-1}cm^{-1}, which is roughly a factor 10^{-4} lower than the electrical conductiv-

ity of ordinary metals such as Cu [51]. This relatively low conductivity value is basically due to two factors: i) There is one, two or more (depending on the anion) conduction electrons per unit cell (volume is about 3000 $Å^3$; this value depends on the anion, see Table 4.1), resulting in a very low conduction electron density of about 10^{21} cm^{-3}, which is roughly one order of magnitude lower than that of ordinary metals. ii) The large number of atoms in the unit cell enhance the scattering processes yielding therefore in a low electrical conductivity.

The effects of electronic correlation are discussed briefly below.

2.4.4 Electronic Correlation Effects

One of the main challenges of condensed matter physics currently refers to the understanding of electron-electron and electron-phonon interactions in low-dimensional materials. The study of these interactions has opened up a new hot field of research: strongly correlated electron systems. A general aspect of many strongly correlated electron systems is the nearness of a superconducting to an antiferromagnetically ordered insulating state. This can be observed in low-dimensional organic systems [35, 36] studied in this work, heavy fermion superconductors [37] and layered high-T_c superconductors [38]. Due to this proximity between superconducting and antiferromagnetic states, it has been speculated that magnetic fluctuations might play a dominant role in the pairing, see e.g. [39], but whether this is true remains to be seen. An accurate and precise theoretical description of strongly correlated electron systems is an actual challenge for theoreticians. An insight into the complexity of describing such systems theoretically can be gained by analyzing the so-called non-relativistic solid state physics operator (Eq. 2.34) [40], where N_n refers to the nuclei with labelled atomic number Z_n and masses M_n, sitting at positions $\boldsymbol{R}_n$ (n = 1, ..., N_N), with kinetic energy (T_n) and nuclei-nuclei electrostatic interaction (V_{n-n}). Similar terms are assumed for the electrons, i.e. (T_e) and (V_{e-e}), at positions $\boldsymbol{r}_i$ (i = 1, ..., N_e)[8]. The interaction between electrons and nuclei is described by the term V_{e-n}. Considering the latter terms and taking the quantum mechanic momentum operator $\boldsymbol{p} \equiv -i\partial/(\partial \boldsymbol{r})$ and $\boldsymbol{P} \equiv -i\partial/(\partial \boldsymbol{R})$ for electrons and nuclei, respectively, the Hamiltonian for solid state physics reads:

$$H = \sum_{n=1}^{N_N} \frac{\boldsymbol{P}_n^2}{2M_n} + \frac{e^2}{2} \sum_{n\neq m=1}^{N_N} \frac{Z_n Z_m}{\mid \boldsymbol{R}_n - \boldsymbol{R}_m \mid} + \sum_{i=1}^{N_e} \frac{\boldsymbol{p}_i^2}{2m} + \frac{e^2}{2} \sum_{i\neq j=1}^{N_e} \frac{1}{\mid \boldsymbol{r}_i - \boldsymbol{r}_j \mid} - e^2 \sum_{n=1}^{N_N} \sum_{i=1}^{N_e} \frac{Z_n}{\mid \boldsymbol{R}_n - \boldsymbol{r}_i \mid} \tag{2.34}$$

The first term on the right side of this Hamiltonian describes the motion of nuclei (T_n), the second one the interaction between nuclei (V_{n-n}), the third one the motion of electrons (T_e), the fourth one the interaction between electrons (V_{e-e}), whereas the last one shows the interaction between electrons and nuclei (V_{e-n}). This Hamiltonian describes a quantum-mechanical many-particle problem and, due its complicated nature the Schrödinger equation for it cannot be solved exactly, at least without appealing

[8] The terms T_n, V_{n-n}, T_e, V_{e-e} and V_{e-n} do not appear explicitly in Hamiltonian 2.34. These terms are used here to a better understanding of the physical meaning of each term in Hamiltonian 2.34.

to approximations [41], as discussed in more details in Ref. [40]. Note that the problem is complex enough even without taking into account spin-orbit coupling, dipole-dipole interaction and gravitational effects. Contrasting with the complexity of the above Hamiltonian (Eq. 2.34), the most successful theoretical approach developed to deal with electron-electron interaction was introduced by J. Hubbard. The Hubbard-Hamiltonian, written in second-quantization notation, is given by:

$$H = \sum_{i,j} t_{ij} a^{\dagger}_{i\sigma} a_{j\sigma} + \sum_{i} U n_{i\uparrow} n_{i\downarrow} \tag{2.35}$$

where t_{ij} is the hopping term from site i to site j in the lattice, $a^{\dagger}_{i\sigma}$ is the creation operator, which creates an electron on site i with spin σ and $a_{i\sigma}$ is the correspondent annihilation operator; U is the on-site Coulomb repulsion potential[9], $n_{i\uparrow}$ and $n_{i\downarrow}$ refer to the number operator for spin up and down, respectively, i.e. $n_{i\sigma} = a^{\dagger}_{i\sigma} a_{i\sigma}$. For systems in which inter-site Coulomb interaction is not negligible, the 1D dimerized extended Hubbard model has been successfully employed. In this case, the Hamiltonian is given by:

$$H = t_1 \sum_{i\,even,\,\sigma} (a^{\dagger}_{i\,\sigma} a_{i+1\,\sigma} + h.c.) + t_2 \sum_{i\,odd,\,\sigma} (a^{\dagger}_{i\,\sigma} a_{i+1\,\sigma} + h.c.) + U \sum_{i} n_{i\uparrow} n_{i\downarrow} + V \sum_{i} n_i n_{i+1} \tag{2.36}$$

where t_1 and t_2 are, respectively, the intra- and inter-dimer transfer integrals and V is the nearest-neighbor Coulomb repulsion. The Hamiltonian 2.36 is called the extended Hubbard model. The latter has been successfully used in the description of the properties of several strongly correlated electronic systems. In particular, this model has been successfully employed in the description of the CO transition, where the inter-site Coulomb repulsion plays a crucial role (Section 2.6). In the following, a background on the ground states and phase transitions, encountered in the phase diagrams of the organic conductors studied in this work, is presented.

2.5 Magnetic Properties of Organic Conductors

2.5.1 Bonner-Fisher Model

When an external magnetic field H is applied on a material, a spin magnetization M is then induced. The latter quantity is defined as the spin magnetic moment per unit volume. In ordinary metals, the spin susceptibility χ_s (χ_s = M/H) of the conduction electrons is practically temperature independent and well described via the Pauli susceptibility. For a precise description of the magnetic properties of strongly correlated systems electron-electron interactions are not negligible and the exchange interaction between the spins has to be taken into account. In particular, if the system is an insulator, electrons are localized, but spin degrees of freedom are still active. In such cases, the

[9]The on-site Coulomb repulsion can be seen as the energy that would be necessary to place 2 electrons on the same site.

exchange interaction between two spin operators at sites i and $i+1$, i.e. S_i and S_{i+1}, can often be described by the homogenous antiferromagnetic (AF) Heisenberg Hamiltonian:

$$H = -J\overrightarrow{S}_i \cdot \overrightarrow{S}_{i+1} \tag{2.37}$$

with J being the coupling constant of the exchange interaction between $\overrightarrow{S}_i$ and $\overrightarrow{S}_{i+1}$. If the AF Heisenberg chain of N spins $\overrightarrow{S}_i$ is now placed in a magnetic field $\overrightarrow{H}$, it is then described by the Hamiltonian:

$$H = -J\sum_{i=1}^{N}\overrightarrow{S}_i \cdot \overrightarrow{S}_{i+1} - g\mu_B\sum_{i=1}^{N}\overrightarrow{H}\cdot\overrightarrow{S}_i \tag{2.38}$$

where g refers to the g-factor and μ_B to the Bohr magneton. The temperature dependence of the spin susceptibility of an isotropic finite spin chain with $3 \leq N \leq 11$ was calculated numerically by Bonner and Fisher [42]. The results were extrapolated to obtain the spin susceptibility of the infinite chain ($N \rightarrow \infty$). In addition, it was found that for a uniform Heisenberg chain, the spin susceptibility χ_s has a smooth maximum value at $k_B T_{max}^{\chi_s} \simeq 0.64 \cdot |J|$, coinciding with a maximum in specific heat/thermal expansion at $k_B T_{max}^{C,\alpha} \simeq 0.48 \cdot |J|$, see also Johnston *et al.* [43]. Later, Eggert, Affleck and Takahashi developed an advanced theoretical model [44] (the so-called EAT model) using the Bethe ansatz to describe the spin susceptibility. The EAT model and the model proposed by Bonner and Fisher differ considerably only at low temperatures, i.e. for $T \leq 0.2 \cdot |J|$.

2.5.2 Spin-Peierls Transition

In contrast to the CDW and SDW transitions discussed above, the spin-Peierls (SP) transition is not due to the instability of the FS in 1D. A SP transition is a magneto-elastic transition which takes place in S = 1/2 quasi-1D AF materials. Due to the formation of singlets (S = 0), the magnetic free energy decrease exceeds the gain in elastic energy of the lattice due to the dimerization thus causing the SP transition. A schematic representation of the SP transition is shown in Fig. 2.4.

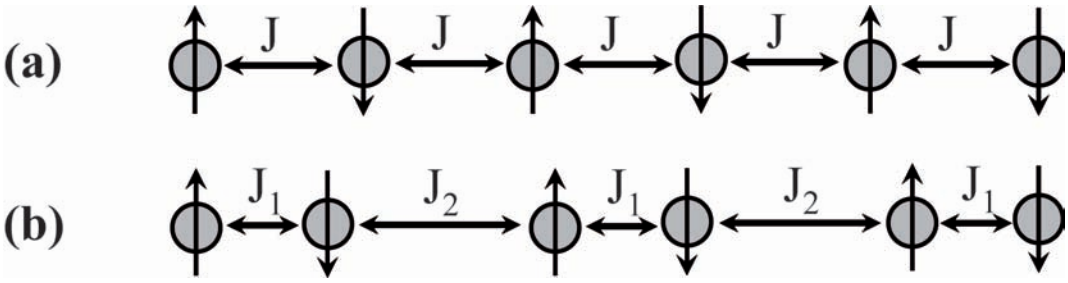

Figure 2.4: Circles represent hypothetical lattice sites and arrows indicate the electron spin. (a) The S = 1/2 AF Heisenberg chain with a uniform exchange coupling constant J; (b) The dimerized chain below T_{SP} with two different coupling constants J_1 and J_2.

The SP transition can be detected experimentally via temperature-dependent spin susceptibility measurements. The susceptibility of a uniform S = 1/2 AF Heisenberg chain has a finite value when $T \rightarrow 0$, indicating thus that for this spin system the energy

activation spectrum is gapless. However, when the chain is elastically distorted to form dimers during the SP transition, the susceptibility of the resulting alternated chain goes exponentially to zero as $T \rightarrow 0$. This indicates that the dimerization produces an energy gap between the singlet (S = 0) and the triplet (S = 1/2) states.

2.6 Charge-Ordering Transition

A charge-ordering (CO) transition[10] can be defined as the self-arrangement of charge carriers in a well-defined superstructure. The latter is a direct consequence of strong electronic correlation effects: if the inter-site Coulomb repulsion V is sufficiently strong, electrons will tend to avoid each other. The reduction of the total electrostatic energy of the system is achieved by the formation of a non-uniformly distributed charge configuration. As discussed above, a Peierls transition requires a metallic state above the critical temperature. This is not the case for the CO transition. If the system is metallic above the CO critical temperature (T_{CO}), the CO transition will be then accompanied by a MI transition. The latter situation is, for example, observed in the $(TMTTF)_2SbF_6$ compound, where a CO accompanied by a MI transition takes place at $T_{CO,MI} \simeq 154$ K. This can be understood intuitively, since the charge carriers organize themselves in distinct patterns and therefore the material becomes insulating. More strictly speaking, this is because of the opening of a gap in the density of states, due to the formation of the superstructure, see, e.g. [46]. Below T_{CO} spin degrees of freedom are still active and, at low temperatures magnetic transitions like SP or AF can take place. The CO transition has been studied theoretically employing the extended Hubbard model (Hamiltonian 2.36) [7]. Using the Hamiltonian 2.36 and the mean-field approximation, Seo and Fukuyama predicted the existence of a CO transition in the quasi-1D organic conductors $(TMTTF)_2X$ before its experimental observation. These calculations were carried out at T = 0 assuming the band filling fixed at quarter filling in a weakly dimerized 1D chain, as shown schematically in Fig. 2.5.

In the following the essence of the CO transition is discussed. Fig. 2.5 gives a schematic description of the CO transition in the $(TMTTF)_2X$ family. According to Fig. 2.5 a) and the mean-field calculations performed in [7], if $t_1 >> V$, the electron will be able to move within the dimer and therefore the spin of each site will be the same, i.e. $S_z(1) = S_z(2) = -S_z(3) = -S_z(4)$, with S_z(i) being the spin moment at the i^{th} site. In this case, the charge will be equally distributed within the dimer. However, if the inter-dimer Coulomb repulsion V is not negligible the situation becomes different. Seo and Fukuyama showed[11] (Fig. 2.6) that, for the quasi-1D $(TMTTF)_2X$ organic conductors, in the presence of finite V (Fig. 2.5 b)), considering the ratio $U/t_2 = 5$[12], i.e. the on-site Coulomb repulsion (Fig. 2.5 c)) is roughly of the same order of magnitude than the inter-site transfer integral, a CO phase transition can occur if the inter-site Coulomb repulsion exceeds a critical value V_c. Experimentally, V_c is achieved by cooling the system or by applying pressure. The consequence of this is that, in order to minimize the total electrostatic energy of the system, at a critical temperature T_{CO} a charge disproportionation (δ) will occur along the chain, so that charge-rich sites will alternate with charge-poor sites, as shown in the inset of Fig. 2.6.

[10] Charge-ordering transition is frequently referred to in the literature as charge-disproportionation.

[11] In fact, it was already showed by Hubbard over 30 years ago that for the (TCNQ) charge-transfer salts if the on-site and near-neighbor electrostatic interactions play the major role, a periodic arrangement of the charge pattern should occur, giving rise to a Wigner crystal [47].

[12] The ratio U/t_2 is referred to as reduced inter-site Coulomb interaction.

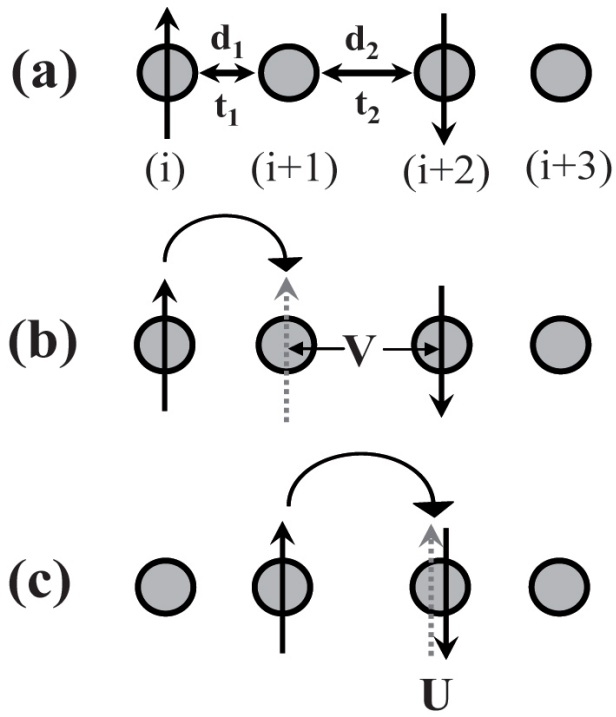

Figure 2.5: Schematic representation of a quarter-filled dimerized AF spin chain. a) For i = 1, the pairs of molecules (1-2) and (3-4) form dimers; transfer integrals t_1 and t_2 are the intra- and inter-dimer, respectively, with $t_1 \geq t_2$. b) V represents the inter-site Coulomb interaction. c) U represents the on-site Coulomb interaction. Arrows indicate the electron spin. Picture after [45].

This charge modulation is usually referred to in the literature as a $4k_F$ CDW. In the quarter-filled $(TMTTF)_2X$ family, this can be easily understood because its periodicity is twice the distance between the TMTTF molecules along the chain direction (*a*-axis), i.e. charge-rich sites alternate with charge-poor sites in a 1010 pattern, where 1 and 0 refer to charge-rich and charge-poor sites, respectively. More detail on the CO transition in the $(TMTTF)_2X$ family will be presented in Chapter 5. Concluding this section, it is useful to mention that evidence for a CO phase has been also observed in other compounds. For example, by means of infra-red (IR) spectroscopy, a phase transition to a CO state was observed in the quasi-2D conductor α-$(BEDT\text{-}TTF)_2I_3$ [48], via NMR studies in the quasi-1D conductor $(DI\text{-}DCNQI)_2Ag$ [49].

2.7 Neutral-ionic transition

The neutral-ionic (NI) phase transition can, as its name suggests, be defined as the phase transition from a neutral crystal (van der Waals interaction) to an ionic (ionic binding) one, for a recent review see, e.g. [50]. In order to gain a better understanding about the NI transition, let us consider a quasi-1D charge-transfer salt with mixed-stack, i.e. along the stacks, donor (D) and acceptor (A) alternate in a — $D^{+\rho}A^{-\rho}D^{+\rho}A^{-\rho}D^{+\rho}$ — fashion, where ρ refers to the degree of charge transfer from the donor to the acceptor. For an ideal case, ρ = 0 for the neutral- and ρ = 1 for the fully ionic-phase. Mixed-stack is, in principle, a necessary condition for the occurrence of a NI transition. In fact, in such systems there is direct competition between two energies: the Madelung electrostatic energy (M), which defines the binding energy of an ionic crystal [51], and the

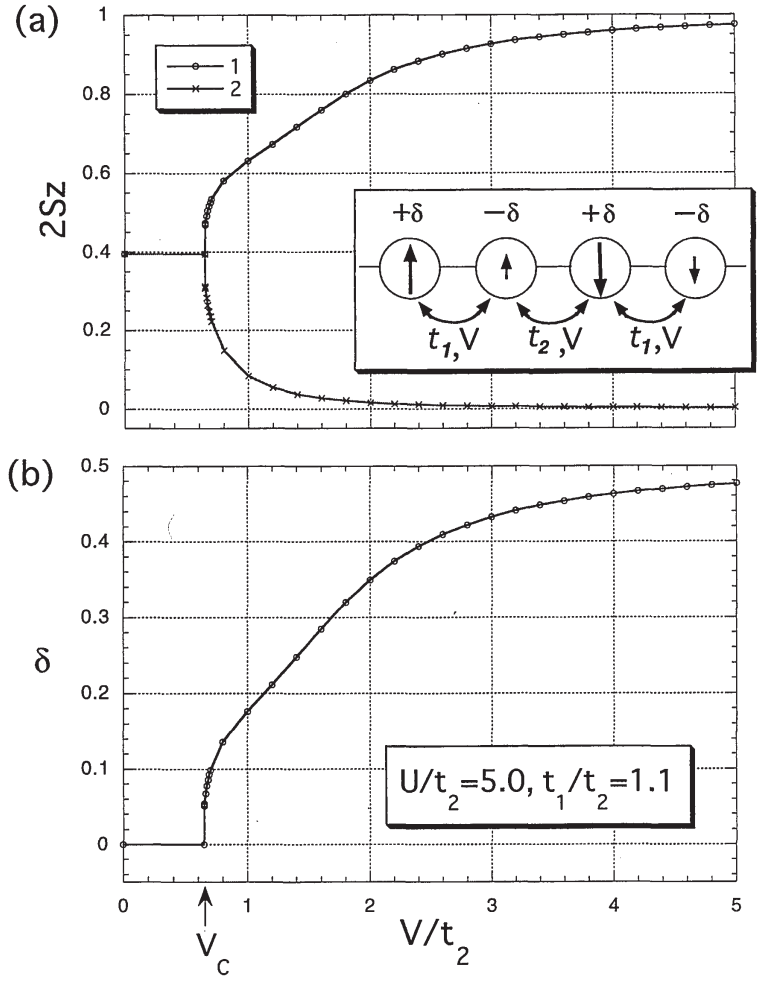

Figure 2.6: a) Absolute value of the spin moment S_z per molecule as a function of the reduced inter-site Coulomb interaction V/t_2. Inset: circles represent charge distribution with their respective spin-densities, $+\delta(-\delta)$ refers to rich(poor) charge sites. b) Charge disproportionation (δ) as a function of V/t_2. Above the critical value V_c, a charge-ordering transition takes place. Pictures taken from Ref. [7].

net ionization energy ($I - A$) i.e. the necessary energy to ionize the donors (I) less the electronic affinity of the acceptor A, which correspond to the necessary energy for the formation of a D^+A^- like neutral crystal. The first observation of a NI occurred in the Tetrathiafulvalene-Chloranil (TTF-CA) charge-transfer salt [52] and since then this material has been recognized as the prototype system for studying the NI transition. Up to now, however, there are a few new materials, in which a NI transition has been observed [50]. According to S. Horiuchi *et al.* [50], generically a set of signatures in the physical properties can be checked experimentally to identify a NI transition in a generic material: a) color change, due to the appearance of a new absorption band in the visible spectral region; b) jump or kink in the electrical resistivity, due to the change of the band gap energy provoked by lattice deformation; c) peak or cusp-like anomaly in dielectric constant caused by change of polarization; d) frequency shift of vibrational modes in the mid-infrared spectra; e) appearance of new bands of vibronic modes due to the electron-molecular vibration coupling; f) structural changes. Features a), d) and f) were observed at the NI transition in (TTF-CA) [53]. A model to describe the NI phase transition for the

latter material was proposed by J. Hubbard and J.B. Torrance [54]. This model can be easily understood by analyzing Fig. 2.7.

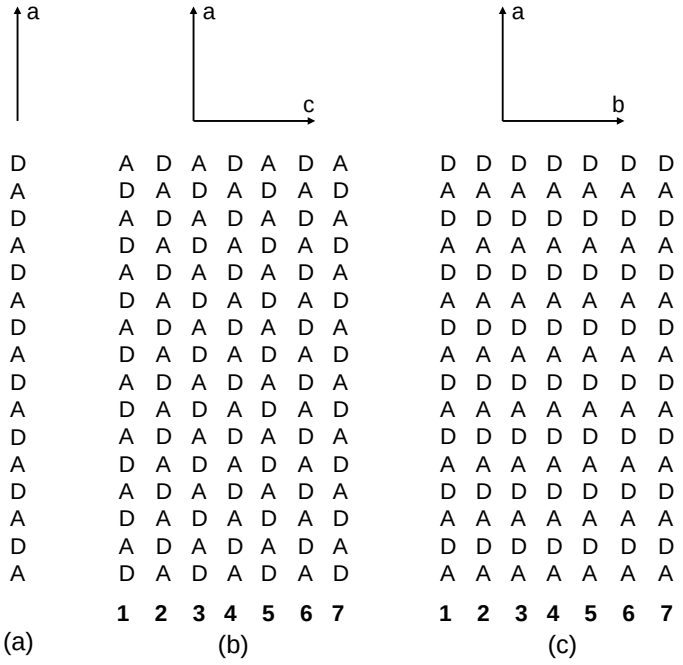

Figure 2.7: Model of the NI phase transition proposed in Ref. [54] for (TTF-CA). (a) Single mixed-stack along the *a* direction, D and A refer to donor and acceptor, respectively. (b) Arrangement of the stacks in the *ac* plane. (c) Arrangement of the stacks in the *ab* plane, showing the repulsion between stacks. Picture after Ref. [54].

According to the authors, at a critical temperature T_1, a single stack will change from a neutral to a completely ionized state, discontinuously, thereby undergoing a first-order phase transition (Fig. 2.7(a)). Now, considering a plane of molecules in the structure of (TTF-CA), as for example the *ac* plane shown in Fig. 2.7(b), one can see that each donor molecule has acceptors as intrastack and interstack nearest neighbors. According to this arrangement of the stacks in the *ac* plane, it is expected that stacks are either fully neutral or fully ionic, so that upon cooling the system from T to T_{NI}, being $T_{NI} < T$, the plane *ac* plane will *continuously* change from neutral to ionic. In other words, if the stack No. 4 is assumed to ionize as $T \rightarrow T_{NI}$, it will induce ionization of the neighboring stacks 3 and 5, which in turn will induce ionization on the stacks 2 and 6, and so on. Hence, according to this model, an attractive Coulomb interaction between stacks in the *ac* plane will make the transition in this plane easier. The temperature T_{NI} is determined by M_{NI} = $I - A$, being M_{NI} the 2D sum over the attractive interstack interaction in the *ac* plane, as highlighted in Fig. 2.7(b). A distinct situation is encountered in the *ab* plane, where the stacks repel each other. Hence, if stack No. 4 were to ionize as $T \rightarrow T_{NI}$, it will not only inhibit the ionization on the stacks 3 and 5, but also the ionization on any other stacks in the *bc* plane, so that at T = T_{NI} at most one stack in this plane will ionize. Upon further cooling, more and more stacks will ionize in the *ab* plane due to the gain of a net energy, proportional to $T_{NI} - T$, by ionizing a stack, so that by cooling the system further, the 3D lattice will be completely ionized. The present discussion will be used in Section 5.5, where evidences for a NI transition in TMTTF salts will be presented.

2.8 The Mott Metal-Insulator Transition

In the field of strongly correlated electron systems, the Mott transition is one of the central themes of study. According to Mott's [55, 56] definition and, in contrast to the usual insulating state, successfully described in the frame of the band theory, the Mott MI transition is induced purely by electron-electron interactions. In other words, the Mott MI transition is directly linked to the competition between kinetic and correlation energy, i.e. wave-like character (delocalized) states versus particle-like (localized) states, see, e.g. [57]. This is because at low densities correlations play a crucial role on the electron gas, as discussed in the following. If one assumes r as the average electronic spacing in a solid, the Coulomb potential energy reads:

$$U = \frac{e^2}{r} \tag{2.39}$$

Solving the Schrödinger equation for a particle (in our case, the electron) confined in a box of width r, one obtains a zero-point kinetic energy, which is given by:

$$K_e = \frac{\hbar^2 k^2}{2m_e} \tag{2.40}$$

where $\hbar$ is the Planck constant divided by 2π, k is the wave-vector and m_e is the electron mass. Eq. 2.40 can still be written as follows:

$$K_e = \frac{\hbar^2}{2m_e r^2} \tag{2.41}$$

Eqs. 2.39 and 2.41 tell us that the kinetic and potential energy of the electrons vary as $1/r$ and $1/r^2$, respectively. Hence, at high densities, i.e. for small r values, the kinetic energy of the electron gas K_e is high enough to allow electrons to move from one site to another. However, at low densities, i.e. large r values, the situation changes. In such a situation, the charge transport process can be described simply by taking one electron from one site M, i.e.

$$M \rightarrow M^+ + e^- \tag{2.42}$$

and placing it on the neighbor site:

$$M + e^- \rightarrow M^- \tag{2.43}$$

The reaction 2.42 requires a certain ionization potential energy (I), while 2.43 gives back a certain amount of energy, namely the electron affinity energy (A). Hence, the necessary energy to transfer one electron from one site to its neighbor in the limit of large r is given by:

$$\Delta E = I - A \tag{2.44}$$

The interaction between the electron and the hole it left behind occurs via Coulomb interaction. The more electrons are excited, the stronger the electron gas will screen the electron-hole (exciton). The screening potential has the following form [58]:

$$V = -\frac{e^2}{r}e^{-\lambda r} \tag{2.45}$$

According to Eq. 2.45, the hole is exponentially screened by the electron gas. The physical consequence of this is that at a given critical concentration, screening effects become weaker and correlation effects play the major role. This occurs when the screening radius λ^{-1} is larger than the separation between electron and hole, i.e. larger than the Bohr radius (a_0). The latter condition can be written as follows:

$$\lambda^{-1} \gtrsim a_0 \tag{2.46}$$

Employing the Bohr radius and the screening constant [58], which is given by:

$$\lambda^2 = \frac{16\pi^2 e^2 m N^{1/3}}{h^2} \tag{2.47}$$

where N is the number of electrons per unity of volume, one obtains the critical electron density (N_c) at which the Mott transition occurs:

$$a_0 N_c^{1/3} \gtrsim \frac{1}{4} \tag{2.48}$$

Thus, at low densities, in order to minimize their energy, electrons have the tendency to occupy localized states. In other words, for an electronic system with $1/2$ filled band, for instance, if the on-site Coulomb repulsion U is comparable to the width of the band W, then the probability of double occupancy is decreased, i.e. the probability of two electrons being on the same site will be decreased. At a critical value of $U/W \approx 1$ the metallic state is no longer stable and a Mott MI transition takes place. For the charge-transfer salts of the κ-(BEDT-TTF)$_2$X family, due to the reduced dimensionality and low electronic density, screening effects are considerably reduced, so that electronic correlation effects are no longer negligible and a Mott MI insulator can be observed. Based on the above discussion, a genuine Mott MI transition can be viewed as the MI transition driven purely by electronic correlations effects. Still in debate is the question, first raised over thirty years ago, of whether lattice degrees of freedom play a role for the Mott transition in real materials. Recently, theoretical studies in the frame of the dynamical mean-field theory (DMFT) have been predicting a lattice anomaly at the Mott transition in *response* to the softening of electronic degrees of freedom. In fact, discontinuous changes of the lattice parameters at the Mott transition were observed in Cr-doped V_2O_3 [59]. The actual role of lattice degrees of freedom for the Mott transition in the fully deuterated κ-(BEDT-TTF)$_2$X organic charge-transfer salts [4] is one of the central topics to be discussed in Chapter 4.

Chapter 3

Experimental Features

In this chapter, a description of the experimental aspects related to this work is presented. In the first part, the main aspects related to high-resolution thermal expansion experiments, which are the central part of this work, are discussed. The second part is dedicated to the discussion of the resistivity measurements under ambient and high pressures using a ^{4}He-gas technique.

3.1 Thermal Expansion Measurements

As already mentioned in previous sections, thermal expansion coefficient measurements are a very useful and powerful tool to detect phase transitions in solid state physics research. The combination of thermal expansion and specific heat data enables us to determine the volume dependence of the characteristic temperatures and may serve also as a check of their direct measurements as a function of hydrostatic pressure. Furthermore, in contrast to specific heat which is an isotropic property, anisotropic effects may be studied via thermal expansion measurements. The measurements presented in this work were performed by employing an ultra-high-resolution capacitance dilatometer, built after [60], with a maximum resolution of $\Delta l/l = 10^{-10}$, in the temperature range 1.3 (pumping of Helium bath) to 200 K under magnetic fields up to 10 T. In order to avoid external vibrations, the cryostat is equipped with shock absorbers. A detailed description of the dilatometer used in this work has been presented in several works [61–63]. The principle of measurement is described in the following. As sketched in Fig. 3.1, the cell, which is entirely made of high-purity copper to ensure good thermal conductivity and covered with gold[1], is constituted basically of a frame (brown

[1]This gold layer should work like a protection. Nevertheless, after some years in use, two striking anomalies have been observed at $T \simeq 212$ K and 230 K. These anomalies are assigned to the formation of copper-oxide (CuO) [64] in the body of the cell. Due to this, experimental data taken in this T window are not reliable.

line) and two parallel pistons (orange), the upper one being movable. The sample is placed between these two pistons and by moving the upper piston carefully the starting capacitance is then fixed. The lower piston is mechanically linked to a parallel plate capacitor, as schematically represented by springs in Fig. 3.1. The variation of the sample length, i.e. contraction or expansion, as the temperature is lowered or increased, together with cell effects corresponds exactly to the change of the distance between the plates of the capacitor[2] and consequently to a change of the capacitance, so that very tiny length changes can be detected. The most remarkable characteristic in this capacitance dilatometer is its high resolution ($\Delta l/l = 10^{-10}$), corresponding to absolute length changes of Δl = 0.01 Angstrom for a sample of length 10 mm. This resolution is roughly five orders of magnitude higher than that of conventional methods like neutrons or X-ray diffraction [1] and is mainly due to the high resolution of the capacitance bridge[3] and the high quality of the plate capacitor in the dilatometer cell, which allows the detection of very small changes[4] in the capacitance of the system. However, the above-mentioned resolution holds until $T \simeq 40$ K, where a precise PID temperature control becomes difficult due to the large time constant involved in the experiment. As deduced in Ref. [60], the sensitivity of the measurements is proportional to the square of the starting capacitance (C^2). This means that the higher the starting capacitance, the higher the sensitivity. However, samples of the organic charge-transfer salts studied, mainly those of (BEDT-TTF) based charge-transfer salts, are very sensitive to the pressure exerted by the dilatometer, so that one cannot set a starting capacitance too high, since this would consequently lead to a break in the sample. Hence, the starting capacitance[5] for measurements under normal pressure (see Subsection 3.1.1) was limited to ∼18 pF.

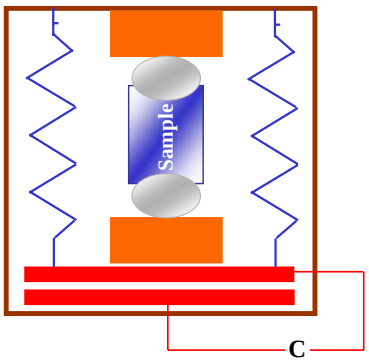

Figure 3.1: Schematic representation of the cell used for the thermal expansion measurements. Details are discussed in the text.

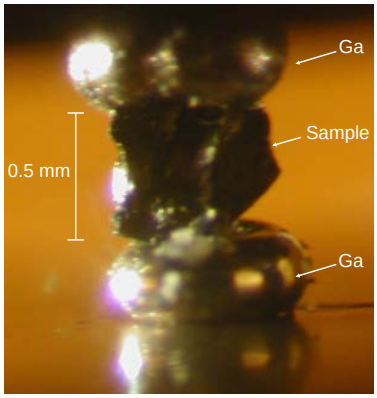

Figure 3.2: Sample of the fully deuterated organic conductor κ-(BEDT-TTF)$_2$Cu[N(CN)$_2$]Br mounted into the cell of the thermal expansion setup.

For measurements under magnetic fields a magnet power supply (model PS120-3) from Oxford Instruments was used. In all performed measurements under magnetic

[2] In this construction, the distance between the plates of the capacitor is about 100 μm. In order to avoid stray electric fields the capacitor is surrounded by guard rings [60].

[3] Two different high precision capacitance bridges have been used in these experiments: (i) Andeen Hagerling - Model 2500A 1 kHz and (ii) General Radio - Model 1616.

[4] Changes of about 10^{-7} pF can be detected in such experiments.

[5] The empty capacitance of the system reads 16.7 pF.

fields reported here, the field was applied parallel to the measured direction. For the directional-dependent thermal expansion measurements, the alignment of the crystal orientation was made using an optical microscope and guaranteed with an error margin of $\pm 5^o$.

The fixation of the sample into the cell was carried out making use of two Gallium-spheres (gray ellipses in Fig. 3.1, also indicated in Fig. 3.2) [62]. These spheres work like holders for the sample. Gallium is an ideal material for this task due its low melting point T_M= 29.78 ^{0}C, enabling the sample to be mounted into the cell with the help of a soldering iron to make liquid Ga.

Furthermore, according to the literature, although Ga presents a small anisotropy in its expansivity, it does not present any anomalous behavior from room temperature down to low temperatures, cf. [65] and references therein.

The data were corrected only for the thermal expansion of copper of the cell body with no further processing like splines or any other kind of mathematical fittings. From the length changes of the sample $\Delta l(T) = l(T) - l(T_0)$ (T_0 is a fixed temperature), which is the physical quantity measured[6], the linear thermal expansion coefficient (Eq. 2.3) was approximated by the differential quotient, as follows:

$$\alpha(T) \approx \frac{\Delta l(T_2) - \Delta l(T_1)}{l(300K) \cdot (T_2 - T_1)} \tag{3.1}$$

where T=(T_1 + T_2)/2, being T_1 and T_2 two subsequent temperatures of data collection.

The control of the measurement was made by use of an interface program in ®*Test Point* language, supplied by MCC (Measurement Computing Corporation) company. In fact, this program was written and first used by Dr. Jens Müller [62] and later improved and further used by Dr. Andreas Brühl [63].

Unless otherwise stated, in order to guarantee thermal equilibrium in all thermal expansion measurements reported here, a very low temperature sweep rate of $\pm\,1.5\,\mathrm{K/h}$ was used.

3.1.1 Thermal Expansion Measurements Under Quasi-Uniaxial Pressure

One of the challenges in the context of thermodynamic measurements is the realization of high-resolution thermal expansion measurements under hydrostatic pressures. Up to now, no such experiments have been reported in the literature. However, by changing the starting capacitance and taking into account the area of contact between the Ga-spheres and the sample, one can perform quasi-uniaxial thermal expansion experiments under pressures up to $\sim$ 100 bar employing the above-described setup. The term "quasi-uniaxial" is used here in the sense that one may have a pressure-gradient on the sample volume, as indicated by the arrows in Fig. 3.3. The upper and lower vertical arrows indicate the pressure exerted by the dilatometer on the Ga-spheres. The dependence between the force (F) exerted by the springs and the capacitance change (ΔC) can be easily measured and is given by:

$$\frac{\Delta F}{\Delta C} = 0.124 \frac{\mathrm{N}}{\mathrm{pF}} \tag{3.2}$$

[6]Worthwhile to notice is that by means of the capacitance dilatometry used here only length changes are measurable. The present method does not enable us to measure absolute length changes of the sample.

Making use of Eq. 3.2 the pressure exerted by the dilatometer on the sample can be estimated. For example, taking the area (A) of contact between the sample and the Ga sphere of 0.2×10^{-6} m^2 and a capacitance change of 2 pF and using the definition of pressure $P = F/A$, results in a quasi-uniaxial pressure P of roughly 12 bar.

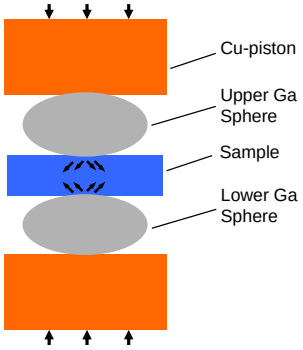

Figure 3.3: Schematic mounting of the sample into the cell of the dilatometer under quasi-uniaxial pressure. The arrows indicate schematically the pressure distribution on the sample volume.

Hence, a slight change of the contact area and/or starting capacitance results in a significant change of the pressure exerted by the dilatometer on the sample. The crucial point of such experiments lies in the assembling and disassembling of the sample holder from the cryostat without damaging the sample, as such procedure is necessary to set the new starting capacitance (new pressure). As will be discussed in Chapter 4, for the (BEDT-TTF) based charge-transfer salts a hydrostatic pressure of a few hundred bar is enough to make a significant sweep across a wide range of the pressure-temperature phase diagram. Measurements under quasi-uniaxial pressure, to be discussed in Section 4.6.4, will show that a quasi-uniaxial pressure of a few tenth of bar changes the shape of the thermal expansion coefficient curves dramatically, indicating therefore that the properties of this material are altered.

3.1.2 Cryostat and Thermometry

The above-described dilatometer was placed in a ^{4}He glass cryostat, whose sketch is shown in Fig. 3.4. ^{3}He was used as the exchange gas.

^{3}He is appropriate to be used as contact gas due to its higher thermal conductivity in comparison with ^{4}He as well as due to the absence of superfluid phase in the Kelvin temperature range. In order to reduce thermal radiation, the external surface of the inner glass dewar is metallized. The sample temperature in the range $T \leq 25$ K was measured by use of a calibrated resistance germanium thermometer, whereas for $T \geq 25$ K, a calibrated resistance platinum thermometer was used. For measurements under magnetic field, similar thermometers placed in the compensated zone of the superconductor magnet were employed.

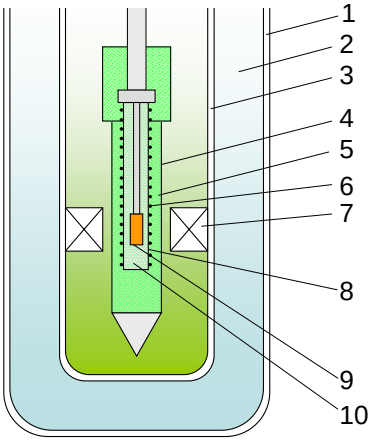

Figure 3.4: Sketch showing the main part of the glass cryostat, in which the dilatometer is assembled. 1) Outer vacuum space; 2) Liquid Nitrogen space; 3) Isolation vacuum space; 4) Inner vacuum cap; 5) ^{3}He contact gas space; 6) Heater; 7) Magnet; 8) Copper heat cap; 9) Dilatometer; 10) ^{3}He contact gas (sample space).

3.2 Resistivity Measurements Under Pressure

Although it is more than seventy years ago that the first studies related to the properties of materials under pressure were performed [66]

(with P.W. Bridgman being awarded with the Nobel Prize in 1946 for his work in this area), it was just in 1986 with the discovery of high T_c superconductors, that more interest in the critical behavior of these materials as a function of applied pressure was shown. Attempts at finding out superconductivity at high temperatures induced by application of pressure have increased the interest in this field of research. In fact, due to their simplicity, the investigation of the transport and magnetic properties at low temperatures is undoubtedly one of the most important tools for the basic characterization of a new material. In strongly correlated electron systems, pressure application may vary the effective electronic interactions, thus giving rise to phase transitions. From the experimental point of view, nowadays, different types of pressure cells have been used to study the physical properties of materials. As shown by Bridgman [66], cylindrical steel pressure vessels can be used for hydrostatic pressures up to maximum 50 kbar. Such vessels are usually used for performing electrical [67] and magnetic [68, 69] measurements in such pressure ranges. However, to achieve higher pressures, diamond pressure cells, which in general enable the increase of pressure up to 300 kbar, have been successfully used for performing thermal [70], optical [71] as well X-ray diffraction studies [72]. In the following, a description of the ^{4}He-gas pressure cell, which was used in this work for resistivity measurements under pressure, is presented.

3.2.1 Electrical Contacts and Plug

All resistivity measurements presented in this work were carried out by employing the standard ac-technique. An ac resistance bridge model LR-700 from the company Linear Research was used for that purpose. Moreover, the standard four-point contacts were used in all measurements. As is well known, the advantage of the four-point method is that one does not take into account the contacts resistance. In this method, current is applied on the external contacts and the voltage is measured on the internal contacts, as shown in Fig. 3.5.

Gold wires of 25 μm diameter were used to make the electrical contacts. To fix the gold wires on the samples, carbon paste (black points in Fig. 3.5) was used. The specific resistivity (ρ) can be directly obtained by using the well-known expression $\rho = R \cdot A/l$, being R the measured resistance, A the cross section area and l the distance between the internal contacts.

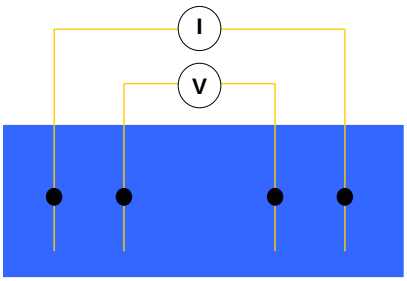

Figure 3.5: The standard four-point probe contacts configuration, as described in the text.

The sample holder, also called plug, of the pressure cell is equipped with eight metal pins, to which the sample contacts are connected using silver or carbon paste. A calibrated InSb semiconductor pressure sensor is connected to the other additional four pins. After preparing the sample and connecting it to the sample holder, the plug should be sealed by a metal seal ring with a diameter of 8 mm and then screwed into the pressure cell. The screw must be inserted very firmly so that the metal seal is crushed, making the connection very tight. For this task, according to the manufacturer [73], a torque of 34 Nm should be applied. Since the plug metal seal ring is strongly distorted by this process, it can be used once only and it must be changed when the cell is disassembled for further measurements.

3.2.2 Cryostat, Thermometry and ^{4}He-Gas Pressure Cell

The pressure cell is placed into a ^{4}He continuous flux cryostat supplied by the firm Cryogenic. For $T \leq 25\,\mathrm{K}$, the temperature of the sample was measured employing a calibrated Lakeshore Cernox-1080 thermometer, whereas for $T \geq 25\,\mathrm{K}$, a calibrated resistance Pt thermometer was used.

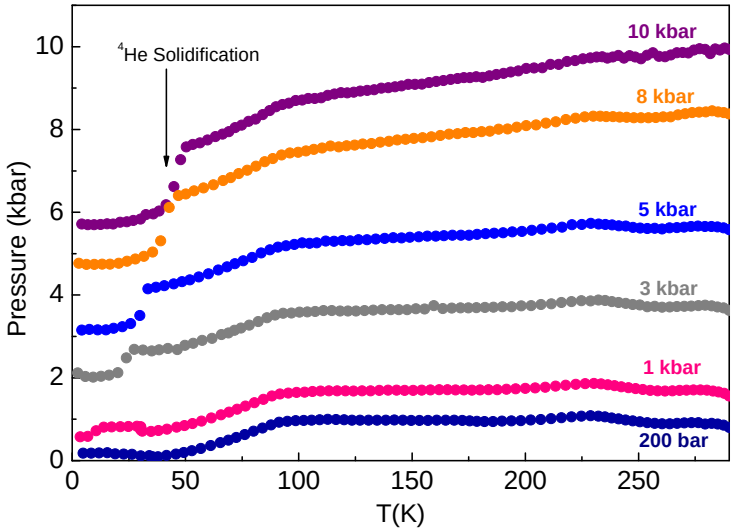

Figure 3.6: Pressure as a function of T obtained using an InSb pressure sensor. Arrow indicates solidification of ^{4}He, as discussed in the text.

For measuring the electrical resistivity under hydrostatic pressure on the conducting poly-MTO (Section 6.3), a ^{4}He-gas pressure cell - Model GC 10 OD/ID 26/7 mm purchased from the Unipress-Warsaw company - was employed [73]. By means of a CuBe capillary tube of internal (external) diameter 0.3(3.0) mm, the latter is connected to a compressor, supplied by the same company. The compressor is then used to generate the desired pressure. This pressure cell permits the application of pressure to the samples within the range from 200 bar, which can be easily generated simply by using the pressure of a ^{4}He bottle, to 11 kbar, which in turn requires the use of the above-mentioned compressor. The body of the cell is a thick-walled cylinder with 26 mm outer diameter, 7 mm inner diameter and 110 mm length. It is made of a good heat-conducting 25 copper/beryllium alloy, being 75% copper, 25% beryllium.

As is known from the literature, one of the main problems, upon performing experiments under pressure using liquid or gas-like pressure transmitter media, concerns the pressure loss during the cool down. This is because upon cooling, depending on the applied pressure, the liquid or gas will freeze. Fig. 3.6 depicts the dependence of pressure as a function of temperature for various pressure values. The pressure values indicated in Fig. 3.6 refer to the applied pressure on the sample at room temperature. Two remarkable features are observed in this data set: i) Upon cooling, a pressure drop around $T \simeq 90\,\mathrm{K}$ is observed in all performed measurements. This feature can be related to some particular change of the physical properties of the studied sample of the compound poly-MTO (to be discussed in Section 6.3); ii) The solidification of ^{4}He as a function of temperature and pressure, which implies a reduction of pressure, is clearly

observed in these experiments, as indicated by the arrow in Fig. 3.6, in agreement with literature data for the phase diagram of ^{4}He [74]. As will be discussed in Section 6.3, the solidification of ^{4}He can be also observed in an abrupt change of the resistivity of poly-MTO.

During the realization of the present work, an oil clamped cell, to be used for magnetic measurements on inorganic magnetic systems using a commercial SQUID magnetometer, was installed and tested. This pressure cell enables magnetic measurements under pressure up to 10 kbar. The most relevant experimental aspects related to magnetic measurements under pressure employing this cell are presented in Appendix 1.

Chapter 4

κ-(BEDT-TTF)$_2$X Organic Conductors

This chapter is concerned with the physical properties of the quasi-2D κ-(BEDT-TTF)$_2$X charge-transfer salts. The major part of the chapter is dedicated to the physics of the fully deuterated salts of κ-phase-(BEDT-TTF)$_2$Cu[N(CN)$_2$]Br. The motivation for studying (BEDT-TTF)-based organic conductors has arisen mainly because this class of materials has been recognized as a prototype system for studying electron-electron correlation effects in 2D. The electronic properties of these substances have been intensively discussed in several reviews, see e.g. [14, 75–85] and more recently [2]. Here the main literature results linked with the present work will be discussed.

4.1 The (BEDT-TTF) Molecule

The basic entity which furnishes the structure of the present class of organic conductors is the (BEDT-TTF) molecule, usually abbreviated simply to ET (hereafter ET will be used instead of BEDT-TTF), shown in Fig. 4.1. Due to the two different possible configurations of the ethylene groups in their extremes, known as staggered and eclipsed configurations, the ET molecule is not completely planar. It is believed that the degrees of freedom of the ethylene groups can influence the electronic properties of the salts of the κ-family, cf. [86] and references therein. Another remarkable aspect related to this molecule is that by means of infra-red real-space imaging spectroscopy on partially deuterated κ-(ET)$_2$Cu[N(CN)$_2$]Br, it was observed that the vibration mode $a_g(\nu_3)$, which is a symmetric stretching mode of the central C=C bonds, is very sensitive to the difference between metallic and insulating states [87].

In the following, the various phases, in which ET charge-transfer salts can crystallize, are discussed briefly.

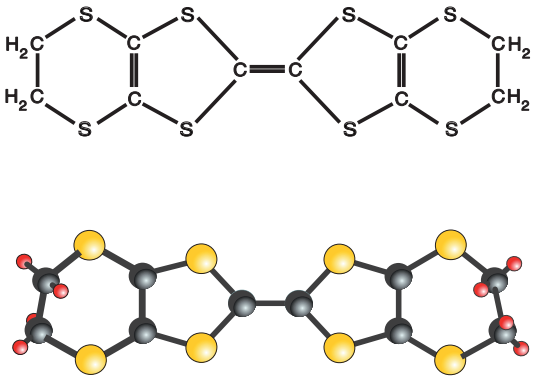

Figure 4.1: (BEDT-TTF), or simply ET, molecule, which is the basic entity that furnishes the quasi-2D (BEDT-TTF)-based charge-transfer salts studied in this work. Picture after [79].

4.2 Phases and Triangular Dimer Model

During the crystallization process, the ET molecules can assume different spatial arrangements giving rise to different phases. Several thermodynamically stable phases, usually referred to by the Greek characters α, β, θ, λ and κ, are known. This work is focussed on salts of the κ-phase family. Interestingly enough, different crystalline arrangements imply different band filling and consequently different physical properties. A detailed discussion about each phase is presented in Refs. [2, 85]. A schematic representation of the main known phases is sketched in Fig. 4.2. As can be seen from the figure, the packing pattern of the κ-phase differs distinctly from the others in the sense that it consists of two face-to-face ET molecules. The two molecules interact with each other via overlap between the highest occupied molecular orbitals (HOMOS), as the HOMOS of each molecule are partially occupied [85].

Due to the intrinsic strong dimerization in the κ-(ET)$_2$X family, pairs of ET molecules can be treated as a dimer unity and the system can be described by the Hubbard model on an anisotropic triangular lattice, as shown in Fig. 4.3. The anion X defines the ratio between the interdimer hopping terms t and t', as for example, for the κ-(ET)$_2$Cu$_2$(CN)$_3$ salt t'/t = 1.06 [78], suggesting an almost perfectly frustrated triangular lattice in this compound, to be discussed in more detail in Section 4.5.

It is well to note that, more recently, a new phase, called mixed phase, with alternating α- and κ-type arrangements of the ET molecules, has been synthesized [89]. More details of the structure of the κ-(ET)$_2$X family, which is the phase studied in this work, are discussed in the next section.

4.3 Crystal Structure

The crystallographic structure of κ-(ET)$_2$Cu[N(CN)$_2$]Br [90] is displayed in Fig. 4.4. The structure of the latter substance is orthorhombic with the space group *Pnma* with four dimers and four anions in a unit cell. An interesting aspect is that although the compounds κ-(ET)$_2$Cu(NCS)$_2$ and κ-(ET)$_2$Cu$_2$(CN)$_3$ [92] also belong to the κ-phase family, their crystallographic structure is monoclinic. Since the counter anion X$^-$ = Cu[N(CN)$_2$]Br$^-$ assumes a closed-shell configuration, metallic properties are observed only within the ET layers, which lie in the crystallographic *ac*-plane and correspond to the large face of the crystal. In the perpendicular direction to the referred

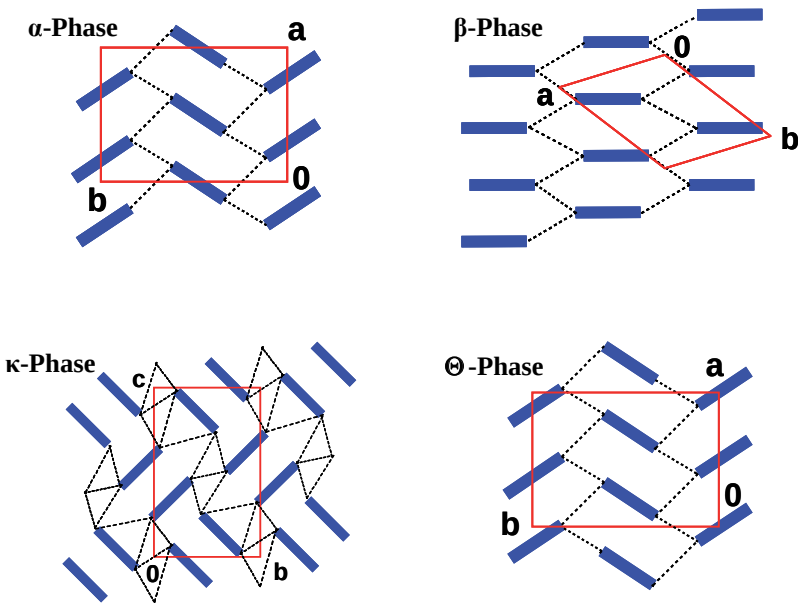

Figure 4.2: Schematic top-view, i.e. view along the long axis of the ET molecule, of the α-, β-, κ- and θ-phase of the ET-based organic conductors. The ET molecules and the unit cells are represented by blue and red rectangles, respectively. The dashed lines indicate the π-orbital overlaps. Picture after [45].

layers, i.e. *b*-direction[1], the insulating anion layer partially blocks charge transfer, so that the conductivity along this direction (perpendicular to the layers) is reduced by a factor $\sim$100 - 1000, depending on the anion. For that reason these materials are called quasi-2D conductors.

As displayed in Fig. 4.5, the $Cu[N(CN)_2]Br^-$ polymeric anion structure is composed of planar triply-coordinated Cu(I) atoms with two bridging dicynamide $[(NC)N(CN)]^-$ ligands, forming a zig-zag pattern chain along the *a*-axis. The terminal Br^- ions, which overlap slightly with the central N atoms of neighboring polymeric chains, make the third bond at each Cu(I) atom [75].

As Fig. 4.6 demonstrates, the anion $Cu_2(CN)_3^-$ differs distinctly from the $Cu[N(CN)_2]Br^-$ anion in that it does not form chains, but a planar network of triangularly coordinated Cu(I) ions and bridging cyanide groups. One of the cyanide groups (labelled N/C11 in Fig. 4.6) is located on an inversion center and therefore must be crystallographically disordered [92]. As will be discussed in the Section 4.8, this particular arrangement is likely to be responsible for the absence of the so-called glass-like transition in κ-$(ET)_2Cu_2(CN)_3$.

Directional-dependent thermal expansion experiments, to be discussed in Section 4.6, will show that the more pronounced lattice effects, associated with the Mott MI transition for κ-D8-Br, occur along the in-plane direction which is parallel to the anion chains direction (*a*-axis). In addition, in Section 4.6 a model based in the collective vibration modes of the CN groups of the polymeric anion chains will be proposed to explain the negative thermal expansion along the *a*-axis above $T_g \simeq 77$ K.

The lattice parameters of the κ-$(ET)_2X$ charge-transfer salts investigated in this work are listed in Table 4.1.

[1]For the κ-$(ET)_2Cu_2(CN)_3$ salt, *a*-axis is the out-of-plane direction.

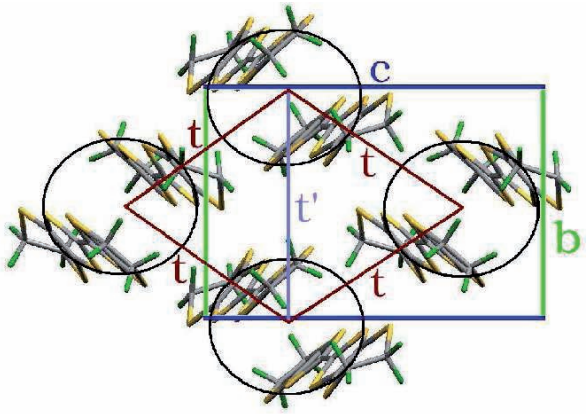

Figure 4.3: Top view of the crystal structure of the κ-(ET)$_2$X salt. The largest hopping terms between the dimers are indicated by t and t'. Note that the hopping terms t, t' and t form a triangular lattice. Picture taken from Ref. [85].

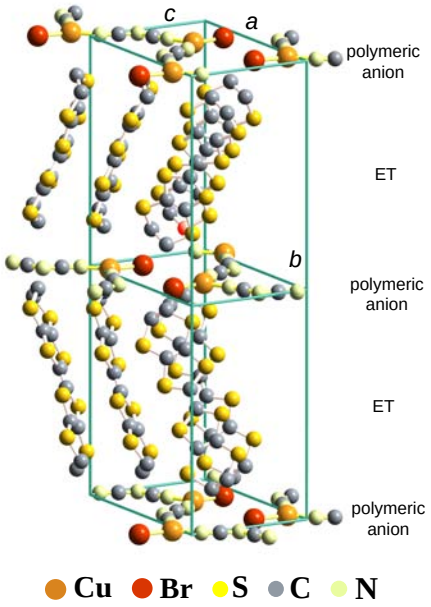

Figure 4.4: The crystallographic structure of κ-(ET)$_2$Cu[N(CN)$_2$]Br. *a* and *c* are the in-plane axes, while *b* is along the out-of-plane direction. ET and polymeric anion indicate layers of ET molecules and anions, respectively. The various atoms are represented by different colors, as indicated in the label. For clarity, protons at the end of the ET molecules are omitted.

4.4 Sample Preparation

Deuterated (98%) bis(ethylenedithiolo)-tetrathiofulvalene (D8-ET) was prepared according to Hartke *et al.* [93] and Mizumo *et al.* [94] by reduction of carbon disulfide with potassium in dimethylformamide and subsequent reaction with deuterated (98%) 1.2-dibromoethane. The intermediate thione $C_5D_4S_5$ was coupled with triethylphosphite in inert atmosphere at 1200 ^{o}C and recrystallized several times from chlorobenzene. By investigating the CH_2 and CD_2 stretch vibrations mode, no signs of any CH_2 or CDH vibrations could be detected, cf. [95]. Hence, the grade of deuteration of κ-(D8-ET)$_2$Cu[N(CN)$_2$]Br is at least 98 % [96]. As discussed in details in Ref. [97],

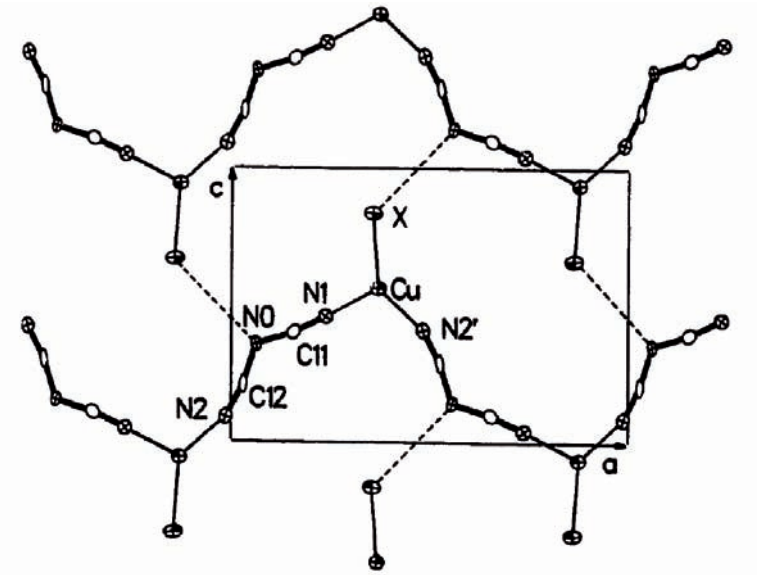

Figure 4.5: Structure of the $Cu[N(CN)_2]X^-$ (X here refers to Br or Cl) polymeric anion layers in κ-$(ET)_2Cu[N(CN)_2]X$, view along the *b*-axis. Dashed lines highlight the X...N weak contacts between the anion chains. Rectangle indicates the contour of the unit cell. Picture taken from Ref. [91].

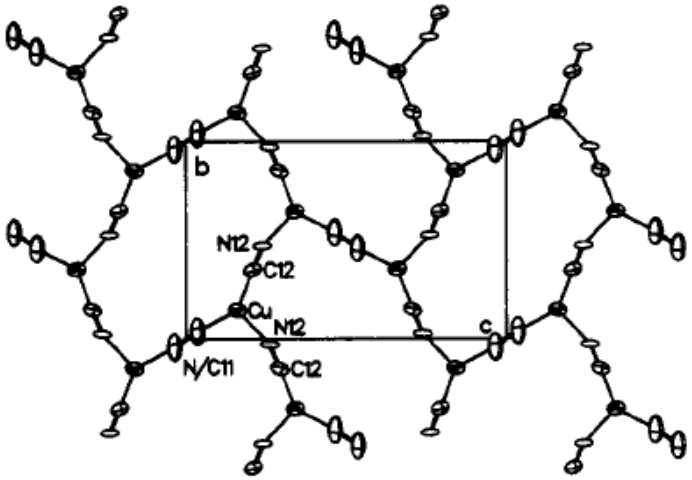

Figure 4.6: Polymeric anion layer of $Cu_2(CN)_3^-$ in κ-$(ET)_2Cu_2(CN)_3$, view along the *a*-axis. Rectangle indicates the contour of the unit cell. The various atoms are represented by ellipsoids with 50% probability. Picture taken from Ref. [92].

by employing the preparation technique described above, hydrogenated single crystals of the same substance resulted in samples whose resistivity revealed reduced inelastic scattering and enhanced residual resistivity ratios. In general, the crystals have bright surfaces in shapes of distorted hexagons with dimensions of approximately $1 \times 1 \times 0.4$ mm^3. Due to the small size of the crystals, the experimental challenge lies in assembling them in the dilatometer, as described in the Section 3.1. The samples of the deuterated and hydrogenated κ-$(ET)_2Cu[N(CN)_2]Br$, κ-$(ET)_2Cu[N(CN)_2]Cl$ and κ-$(ET)_2Cu_2(CN)_3$ salts used for measurements in this work are listed in Table 4.2. The fully deuterated (hydrogenated) salts of κ-$(ET)_2Cu[N(CN)_2]Br$ will be subsequently referred to as κ-D8-

Anion	*a*(Å)	*b*(Å)	*c*(Å)	V(Å^3)	α	β	γ	Structure
D8-Br	-	-	-	-	$\perp$	$\perp$	$\perp$	Orthorhombic
H8-Br	12.949	30.016	8.539	3317	$\perp$	$\perp$	$\perp$	Orthorhombic
H8-Cl	12.977	29.977	8.480	3299	$\perp$	$\perp$	$\perp$	Orthorhombic
$Cu_2(CN)_3$	16.117	8.5858	13.397	1701.2	$\perp$	113.42^0	$\perp$	Monoclinic

Table 4.1: Lattice parameters at room temperature and structure of the investigated κ-(ET)$_2$X salts [91, 92]. Data for κ-D8-Br are not available in the literature. $\perp$ corresponds to 90^o.

Br (κ-H8-Br). Samples of κ-(ET)$_2$Cu$_2$(CN)$_3$ studied here were prepared according to Ref. [92].

Anion X	Crystal Number	Measured Direction	Batch
D8-Br	1	*a*, *b*, *c*	A2907*
D8-Br	2	*a*, *b*	A2995*
D8-Br	3	*a*, *b*, *c*	A2907*
D8-Br	4	-	A2907*
H8-Br	7	*b*	A2719*
H8-Cu$_2$(CN)$_3$	1	*a*	SKY 1050**
H8-Cu$_2$(CN)$_3$	1	*c*	KAF 5078**
H8-Cu$_2$(CN)$_3$	2	*b*	KAF 5078**
H8-Cl	1a	*b*	MJB1020**

Table 4.2: Samples of the organic conductor κ-(ET)$_2$X on which thermal expansion measurements were performed. * refers to samples provided by Prof. Dr. D. Schweitzer (University of Stuttgart) and ** to samples provided by Dr. J. Schlueter (Argonne National Laboratory - USA). Crystal #4 was used to perform preliminary studies of Raman spectroscopy. In Ref. [4] crystal #2 is referred to as crystal #3.

In the next section, the phase diagram and main literature results of the κ-(ET)$_2$X family connected to this work are introduced.

4.5 κ-(ET)$_2$X: State of the Art

Charge-transfer salts of the κ-(ET)$_2$X family have been recognized as strongly correlated electron systems. Among other features, the latter statement is based on the unusual metallic behavior inherent to these systems, as will be discussed below. Band structure calculations suggest that these materials should be metals down to low temperatures [85]. However, due to correlation effects, the phase diagram embodies various phases, including paramagnetic (PI) and antiferromagnetic (AF) Mott insulator, superconductor and anomalous metal, see Fig.4.7.

A remarkable feature is the competition between antiferromagnetic ordering and superconductivity, cf. Fig. 4.7. The similarities between the present charge-transfer salts and high-T_c superconductors have been discussed in the literature, see e.g. [78, 98, 99]. The major difference between these two classes of materials is that while for the high-T_c superconductors one deals with a *doping-controlled* Mott transition, for the charge-transfer salts to be discussed here one has a *bandwidth-controlled* Mott transition. In addition, no spin-glass phase between the two above-mentioned phases is observed in organic conductors. A possible explanation for this feature is the higher quality of organic

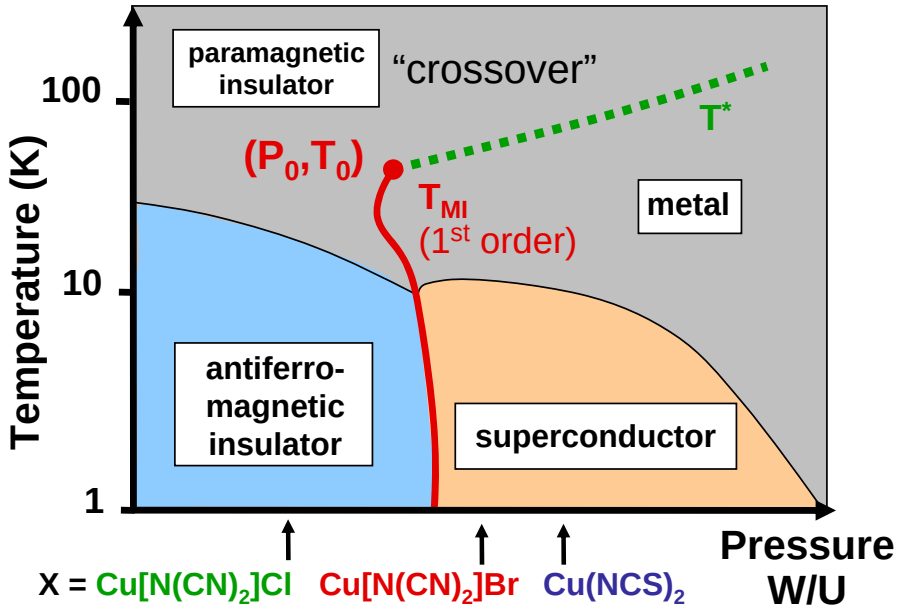

Figure 4.7: Conceptual P-T phase diagram for the κ-(ET)$_2$X family, after [106]. Arrows indicate the positions of the various salts with their anion X at ambient pressure. Application of hydrostatic pressure implies a reduction of the ratio of the on-site Coulomb repulsion relative to the bandwidth U/W.

single crystals in comparison with those of cuprates [99]. The symmetry of the superconducting order parameter in these materials, i.e. s- or d-wave type[2], is still a topic of debate in the literature, see e.g. [100] and references therein. From the experimental point of view, a remarkable feature is the tunability of such systems. In contrast to the high-T_c superconductors, where the ground states are tuned by doping, i.e. band filling, and therefore disorder is unavoidable, the ground states of organic conductors can be tuned by chemical substitution and/or applying external pressure. Pressure mainly affects the bandwidth W and as a consequence the ratio U/W is changed. A pressure of a few hundred bar, which is easily attainable in our laboratory, is enough to make a wide sweep over relevant regions of the pressure-temperature (P-T) phase diagram[3].

4.5.1 Phase Diagram and Experiments

The phase diagram shown in Fig. 4.8 has been mapped by NMR and ac susceptibility [36], transport [102] and ultra-sonic [101] measurements under helium gas pressure on the salt with X=Cu[N(CN)$_2$]Cl. In this phase diagram, the antiferromagnetic transition

[2]For an s-wave superconducting state, the order parameter is finite at every point on the Fermi surface, while for a d-wave type it vanishes at certain points (nodes) on the 2D Fermi surface and changes its sign. Experimentally, the distinction between s- and d-wave type can be made by measuring the specific heat at very low temperatures. As for an s-wave state the order parameter parameter presents finite values at every point on the Fermi surface, it is expected that for $T << T_c$ the specific heat obeys an activated behavior, i.e. $C_V \propto \exp(-\Delta_0/k_B\,T)$, where Δ_0 is the gap value at $T = 0$. For a d-wave state, the situation is different: given the existence of nodes at the Fermi surface, the density of states $D(E)$ grows linearly as one moves away from the Fermi energy, i.e. $D(E) \propto \mid E - E_F \mid$ for $\mid E - E_F \mid << \Delta$. As $C_V/T \propto D(E)$, it follows that at very low temperatures $C_V \propto T^2$ [85].

[3]For the Mott insulator V_2O_3, for example, a pressure of a few kbar is required to cross the first-order line in the P - T phase diagram [19].

line, not observed in ultra-sound experiments [101], was obtained by NMR relaxation rate [36]. From the splitting of NMR lines, the estimated magnetic moment per dimer is (0.4 - 1.0) μ_B. The superconductivity line was determined from ac susceptibility [36] whereas the *S*-shaped first-order MI transition line via ultra-sound [101], transport [102] and ac susceptibility [36] measurements.

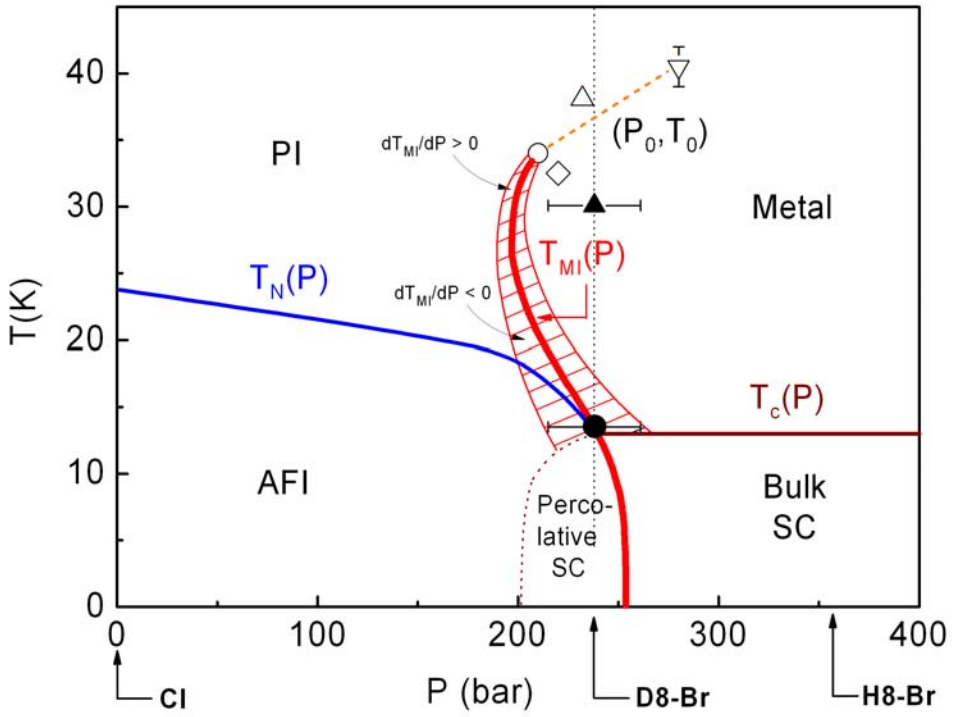

Figure 4.8: Phase diagram of κ-(ET)$_2$Cu[N(CN)$_2$]Z, with Z = Br or Cl. Lines indicate the respective phase transitions. D8-Br and H8-Br (position estimated according to [103]) refer to the positions of κ-D8-Br and κ-H8-Br, respectively. Orange broken line indicates the anomalous metal region. Thin solid lines (red), delimiting the hatched area, denote positions of anomalies observed via ultrasonic measurements (see Fig. 4.10). Vertical (black) dotted line indicates T sweeps, illustrating a crossing of the *S*-shaped line. PI, AFI and SC refer to paramagnetic insulator, antiferromagnetic insulator and superconductivity, respectively. Closed circle refers to T_{MI} coinciding with T_N at this point in the phase diagram, cf. the discussion in the Section 4.6.2. Positive and negative slopes of dT_{MI}/dP are shown, indicating that upon crossing the MI line when $dT_{MI}/dP > 0$, i.e. going from the PI state to the metallic state, the entropy of the system is increased, while crossing the MI line when $dT_{MI}/dP < 0$, i.e. going from the metallic state to the AFI state, the entropy associated with the metallic state is decreased due to the magnetic ordering.

This first-order MI line ends in a critical point (P_0, T_0), which has been studied by several groups [36, 101, 102, 104]. A conclusive understanding of the latter feature is still lacking. Among possible scenarios, this critical end-point has been discussed in analogy with the liquid-gas transition, see e.g. Ref. [105]. In this scenario, above (P_0, T_0) the metallic state cannot be distinguished from the paramagnetic insulating state. The latter scenario seems, however, to be unlikely, since above (P_0, T_0) distinct anomalies reminiscent of phase transition lines are observed. By means of resistivity measurements under pressure, the critical behavior in the vicinity of (P_0, T_0) was investigated

by Kagawa *et al.* [22]. As already mentioned in Section 2.3, these authors found critical exponents which do not fit in the known universality classes, and they assigned this to the quasi-2D structure of the present substances. This will be discussed in more detail in Section 4.7. The tunability of the system from the insulating to the metallic side of the phase diagram, crossing the first-order MI line by application of pressure, is indicative of a bandwidth-controlled Mott transition. Owing to the position of the salts with different anions X, as shown in Fig. 4.8, the fully hydrogenated salt with X = Cu[N(CN)$_2$]Br is a superconductor with $T_c \simeq 12$ K, the highest T_c under ambient pressure among all organic compounds up to now, whereas the ground state of the salt with X = Cu[N(CN)$_2$]Cl is an antiferromagnetic insulator with $T_N \simeq 27$ K. Interestingly enough, exchanging the hydrogen atoms of the ethylene end groups of the ET molecules by deuterium in the compound with X = Cu[N(CN)$_2$]Br results in a shift of the latter towards the boundary of the *S*-shaped first-order line. It is due to their close position to this line [3], that κ-D8-Br hereafter, have been attracting particular interest. Deuterium substitution implies a slight difference between the C-H and C-D bond lengths. Since D has a higher mass than H, C-D bonds have a smaller stretching frequency than the C-H bonds. Hence, during the stretching vibration the D-atoms displacement from their equilibrium position is smaller than that estimated for H atoms. Therefore, the C-D bonds are slightly smaller than the C-H bonds. Furthermore, the contact between the C-D$_2$ end groups and the anions is weaker than that between the C-H$_2$ end groups and the anions. As a consequence, the lattice of the fully deuterated salt is softer than the lattice of the fully hydrogenated. This process is usually called "chemical pressure". In fact, application of pressure (chemical or external) leads to a variation of the distance between the ET molecules and, as a consequence, the bandwidth *(W)* is changed. The ratio U/W is believed to be the key parameter which defines the ground states of these substances [106].

Interestingly enough, for the salt with the anion X = Cu$_2$(CN)$_3$ magnetic ordering is absent in the whole insulating region. The pressure-temperature phase diagram of the κ-(ET)$_2$Cu$_2$(CN)$_3$ salt is shown in Fig. 4.9.

The main literature results of the κ-(ET)$_2$X family are discussed below.

4.5.2 Literature Results

As mentioned in the introduction of this section, the metallic state of κ-(ET)$_2$X presents some distinct properties as compared to those of conventional metals. For instance, in the κ-H8-Br salt, the out-of-plane resistance as a function of temperature has a non-monotonic behavior [97] with a maximum around 90 K, which was observed to be sample-dependent. This maximum is followed by a sudden drop and the resistivity sharply changes its slope around $T^* \simeq 40$ K. At $T_c \simeq 11.5$ K superconductivity is observed. On applying pressure, T^* shifts to higher temperatures and disappears at roughly 2 kbar. From about $T^* \simeq 40$ K down to $T_c \simeq 11.5$ K the resistance obeys a T^2 behavior frequently assigned to a coherent Fermi liquid state. NMR studies revealed a peak in the spin-relaxation rate divided by temperature $(1/TT_1)$ around T^* for the present compound [107]. The anomalous metallic behavior around T^* was also observed by thermal, magnetic, elastic and optical measurements, cf. [97] and references therein. The origin of the T^* anomaly is still controversial. Ultrasonic velocity measurements under pressure on the compound κ-(ET)$_2$Cu[N(CN)$_2$]Cl performed by Fournier *et al.* [101] revealed the existence of two new lines in the phase diagram (not indicated in Fig. 4.8). The experimental findings obtained by Fournier *et al.* are shown in Fig. 4.10. From this data set, pronounced anomalies, depending on the pressure, are observed below around 40 K. The maximum amplitude of the softening in the sound velocity ($T \approx 34$ K, $P \approx 210$ bar)

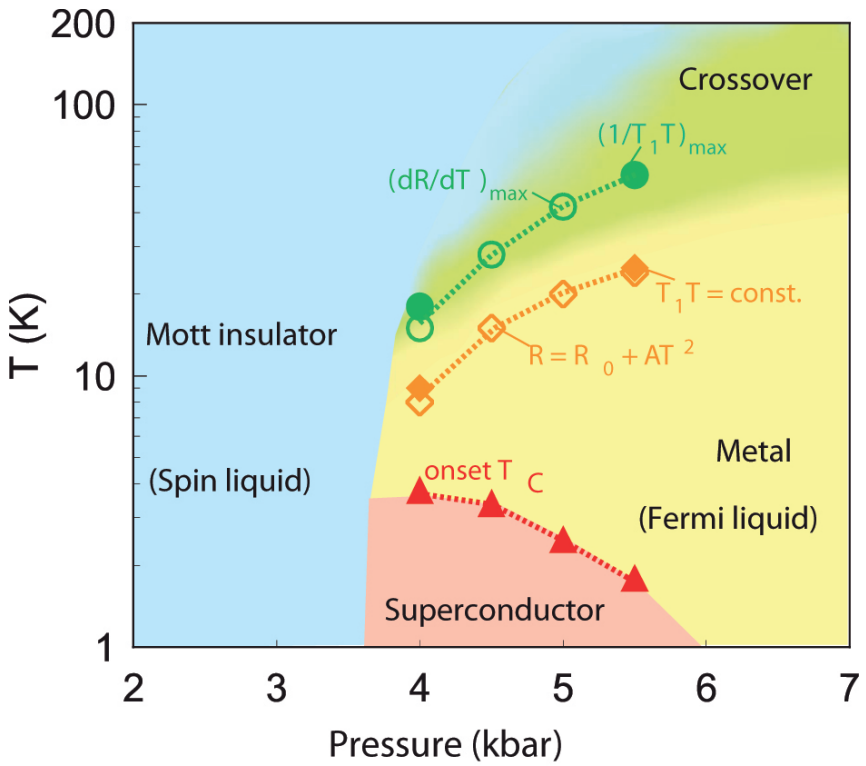

Figure 4.9: P-T phase diagram of the κ-(ET)$_2$Cu$_2$(CN)$_3$ salt, obtained from resistance and NMR measurements under pressure using an oil pressure cell. The Mott transition and crossover lines correspond to the temperature, at which the maximum in the quantities spin-lattice relaxation rate divided by temperature $(1/T_1T)$ and dR/dT are observed, cf. labels indicated in the figure. The upper limit of the Fermi-liquid region (yellow area) was fixed as the temperature where the resistance R no longer follows the $R_0 + AT^2$ relation and $(1/T_1T)$ is constant. The superconducting transition line was obtained via in-plane resistance measurements. Picture taken from Ref. [111].

marks the critical end point (P_0, T_0) and corresponds to a softening of roughly 20 % of the sound velocity. On increasing the pressure, the peak position shifts its position to higher temperatures. Below P_0 the anomaly becomes gradually less pronounced and saturates at around 32 K. The peak position was thus used by the authors to draw the two *crossover* lines in the phase diagram (Fig. 4.11).

As can be seen in Fig. 4.11, these two lines merge into the critical end-point of the first-order line. Interestingly enough, the line above (P_0, T_0) coincides with the T^* anomaly mentioned above. The authors assigned these two lines to *crossover* lines. However, as discussed in Refs. [75, 97] the proposed *crossover* hypothesis seems to be inconsistent, since the transition temperature T^* obtained from resistivity measurements coincides with the correspondent signatures in thermal expansion experiments, as expected for a real phase transition. The large anomalies in the sound velocity observed by Fournier *et al.* were discussed in terms of a diverging compressibility of the electronic degrees of freedom. As a matter of fact, acoustic and lattice anomalies are, according to dynamical mean-field theory (DMFT) calculations, expected at the Mott MI transition as a reaction to the softening of the electronic degrees of freedom, cf. [108, 109]. The explanation for this is that in the metallic state the conduction electrons contribute more to the cohesion of the solid than in the insulating one. Based on this argument, according to Ref. [108],

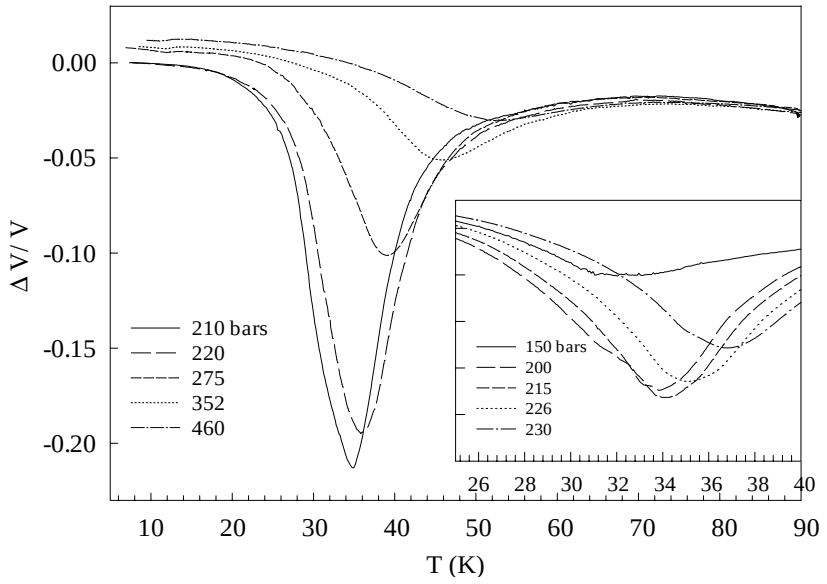

Figure 4.10: Main panel: Relative ultrasonic velocity as a function of temperature under pressure for the κ-$(ET)_2Cu[N(CN)_2]Cl$ salt. The various pressure values are indicated in the label of the figure. Inset: Data for pressures below 230 bar. Picture extracted from [101].

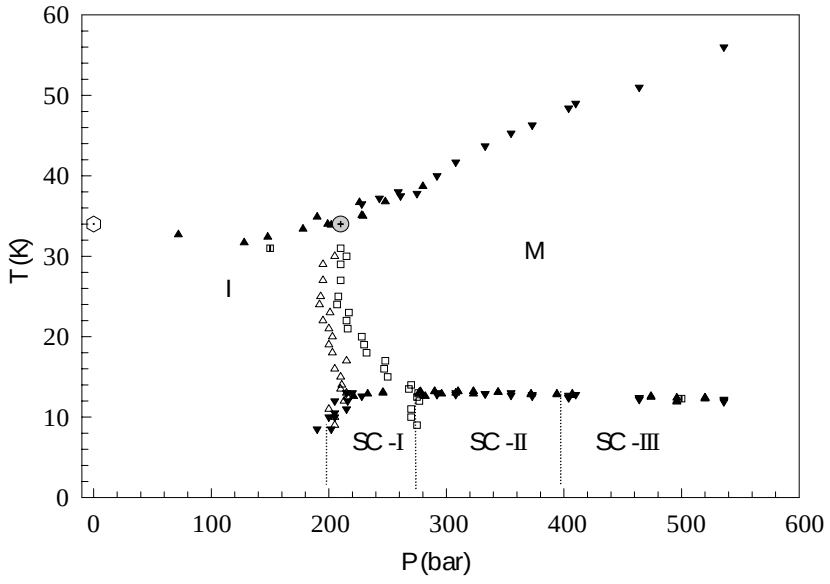

Figure 4.11: Phase diagram obtained from ultrasound experiments under pressure for the κ-$(ET)_2Cu[N(CN)_2]Cl$ salt. Different symbols refer to the various anomalies observed on three different samples. The critical point (P_0, T_0) is indicated by the gray circle. SC-I and -II indicate metastable superconductivity, while SC-III indicates bulk superconductivity. Dotted hexagon indicates the pressure point, obtained from microwave resistivity measurement at ambient pressure. Picture extracted from Ref. [101].

as an effect of the localization, discontinuous changes of the lattice parameters are expected at the Mott transition. The actual role of lattice degrees of freedom for the present

material is one of the main topics of the present study and will be discussed in the Section 4.6.

Owing to the magnetic properties of the κ-(ET)$_2$X family, several studies employing different experimental methods have been carried out on the salt with X = Cu[N(CN)$_2$]Cl [127–129]. By means of resistance measurements, for instance, varying temperature, pressure and magnetic field, a magnetic-field-induced Mott MI transition was observed by F. Kagawa *et al.* [130]. From the analysis of their NMR line shape, relaxation rate and magnetization data, K. Miyagawa *et al.* [129] were able to describe the spin structure of this state. Below T = 26 - 27 K, they found a commensurate antiferromagnetic ordering with a moment of (0.4 - 1.0) μ_B/dimer, as already mentioned in Section 4.5.1. The observation of an abrupt jump in the magnetization curves for fields applied perpendicular to the conducting layers, i.e. along the *b*-axis, was discussed in terms of a spin-flop (SF) transition. Furthermore, a detailed discussion about the SF transition, taking into account the Dzialoshinskii-Moriya exchange interaction, was presented by D.F. Smith *et al.* [131,132]. Similarly to that for the pressurized chlorine salt, a magnetic-field-induced MI transition was also observed in partially deuterated κ-(ET)$_2$Cu[N(CN)$_2$]Br [133]. In addition, a discussion on the phase separation and SF transition in κ-D8-Br was also reported in the literature [116].

The Mott insulator κ-(ET)$_2$Cu$_2$(CN)$_3$ is another system that has been intensively studied in the last five years [5,110,111]. Among all charge-transfer salts of the κ-family, the latter compound presents a peculiarity: the ratio of the hopping terms t and t' is close to unity, more precisely 1.06 [78], leading to a nearly perfect isotropic $S = 1/2$ triangular lattice with the coupling constant[4] J = 250 K. Magnetic susceptibility and NMR measurements revealed no traces of long-range magnetic ordering down to 32 mK [110]. Based on these results, this system has been proposed to be a candidate for the realization of a spin-liquid state [112]. Amazingly, upon applying pressure (see Fig. 4.9), the system becomes a superconductor [111], i.e. superconductivity appears in the vicinity of a spin-liquid state! Recently, however, specific heat experiments revealed the existence of a hump at 6 K, insensitive to magnetic fields up to 8 T (Figs. 4.13 and 4.12).

This feature was assigned to a crossover[5] from the paramagnetic Mott insulating to the quantum spin-liquid state [5]. Below 6 K, the specific heat presents a distinct T-dependence, including a T-linear dependence in the temperature window 0.3 - 1.5 K, as predicted theoretically for a spin-liquid [113]. The spin entropy in this T-range is roughly 2.5% of $R \ln 2$ [114], indicating that below 6 K only 2.5% of the total spins contribute for the supposed spin-liquid state. Extrapolating the low-T specific heat data, the authors found a linear specific heat coefficient $\gamma = (20 \pm 5)$ mJ mol^{-1} K^{-2}, which is sizable given the insulating behavior of the material and contrasts with a vanishing γ value for the related compounds κ-(ET)$_2$Cu[N(CN)$_2$]Cl and fully deuterated κ-(ET)$_2$Cu[N(CN)$_2$]Br, cf. [5] and references therein. A sophisticated theoretical model entitled *Amperean Pairing Instability* has been proposed by Lee *et al.* [115] to describe a possible spin-liquid state in κ-(ET)$_2$Cu$_2$(CN)$_3$. In this model, a pairing of excitations with fractionary spins (spinons) should occur on the Fermi surface at low temperatures. Using a complicated theoretical approach the authors deduce that this pairing of spinons accompany a spontaneous break of the lattice symmetry, which in turn should couple to a lattice distortion (analogously with the Spin-Peierls transition, discussed in Section 2.5.2) and should be

[4] This coupling constant (J = 250 K) was obtained by fitting the magnetic susceptibility using the triangular-lattice Heisenberg model.

[5] This "crossover" has been frequently referred to as "hidden ordering".

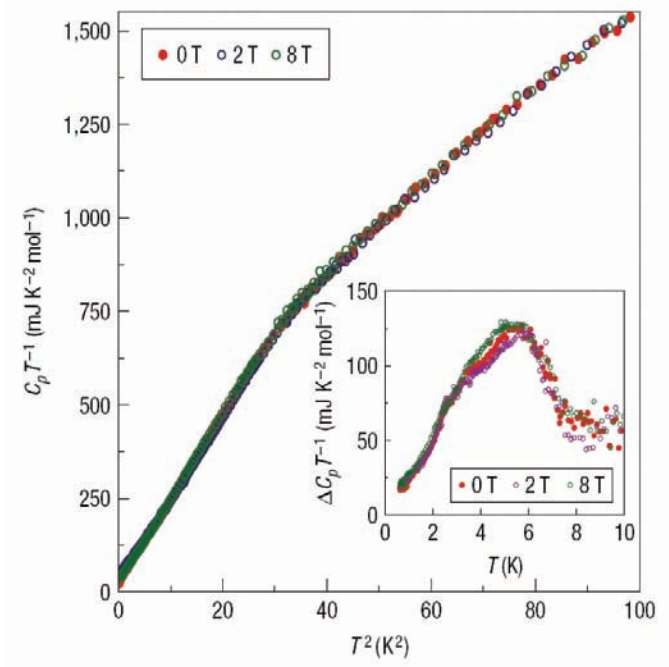

Figure 4.12: Main panel: Specific heat data for κ-(ET)$_2$Cu$_2$(CN)$_3$ in a C_pT^{-1} versus T^2 plot until 10 K. A broad hump anomaly around T = 6 K can be clearly observed. Inset: Specific heat data for κ-(ET)$_2$Cu$_2$(CN)$_3$, considering that the data of κ-(ET)$_2$Cu(NCS)$_2$ give a phonon background. Picture extracted from Ref. [5].

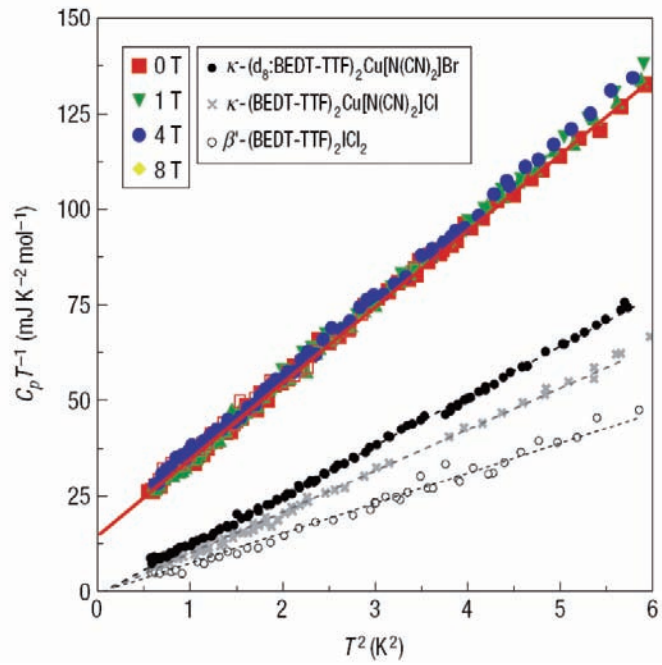

Figure 4.13: Low-temperature specific heat data for κ-D8-Br, κ-(ET)$_2$Cu[N(CN)$_2$]Cl and κ-(ET)$_2$Cu$_2$(CN)$_3$ salts in a C_pT^{-1} versus T^2 plot. Red solid line indicates the existence of a T-linear contribution. Data under magnetic fields for the κ-(ET)$_2$Cu$_2$(CN)$_3$ salt are also shown. Picture taken from [5].

detectable experimentally via X-ray scattering. Nevertheless, Ramirez [114] pointed out that before a final declaration of the realization of a spin-liquid, some points should

be clarified, among them the transition observed in the specific heat at 6 K. In order to obtain more information about this exciting system, high-resolution thermal expansion measurements have been performed in the frame of this work. The results will be discussed in the Section 4.8.

4.6 Thermal Expansion Measurements on Fully Deuterated Salts of κ-(ET)$_2$Cu[N(CN)$_2$]Br ("κ-D8-Br")

As part of this research, intensive investigations on the thermal expansion of the entitled organic compound were performed [4]. As otherwise stated, in order to reduce cooling-rate dependent effects, a cooling rate of ~ -3 K/h through the so-called glass-like transition around 80 K was applied[6]. Fig. 4.14 shows the linear thermal expansion coefficient (upper part) along the in-plane *a*-axis for crystals #1 and #3 together with the out-of-plane resistivity $\rho_\perp$[7] (lower part) for crystal #1. Upon cooling, $\rho_\perp$ passes over a maximum around 45 K, then rapidly drops and flattens abruptly around 30 K. The resistivity remains metallic down to about 20 K, below which the slope sharply increases (cf. upper inset in Fig. 4.14) indicating the transition to an insulating state. An almost identical $\rho_\perp$ behavior was found for crystal #3 and the crystal studied in Ref. [103], except for small differences around the maximum and some details in the insulating regime. For all three crystals, $\rho_\perp$ vanishes below about 11.5 K. A zero resistivity accompanied by a tiny signature in the $\alpha_i(T)$ data is consistent with percolative superconductivity in a minor metallic phase coexisting with an antiferromagnetic insulating ground state for κ-D8-Br [116][8], cf. the phase diagram in Fig. 4.8.

As can be seen from Fig. 4.14, the main features in the resistivity have their clear correspondence in the coefficient of thermal expansion. The rather abrupt flattening of $\rho_\perp$ is accompanied by a huge maximum in $\alpha(T)$ centered at a temperature $T_p \simeq 30$ K[9]. As will be discussed below, this effect can be assigned to a second-order phase transition. Upon further cooling, $\alpha(T)$ reveals an even bigger negative peak indicating yet another phase transition. The accompanying change in $\rho_\perp$ from metallic to insulating behavior suggests this peak to be due to the MI transition[10]. A similar $\alpha_a(T)$ behavior is observed for crystal #2 although with slightly reduced ($\sim 20\%$) peak anomalies at T_p and T_{MI}. This

[6] This cooling speed (~ -3 K/h) was employed in the temperature range $\sim$85 - 65 K. From room temperature down to $\sim$85 K as well as from 65 K down to 4.2 K, an average cooling speed of -40 K/h was employed.

[7] Resistivity measurement shown in Fig. 4.14 was carried out by Christian Strack, Ph.D. thesis (in preparation), Goethe University - Frankfurt (M) - Germany.

[8] In Ref. [3], Kawamoto *et al*. performed ac susceptibility measurements on κ-D8-Br after slow (0.2 K/min) and rapid (100 K/min) cooling. From the measurements after slow cooling, below the onset of superconductivity at T_c = 11.5 K, they did not observe a jump in the real part of the ac susceptibility, as expected for bulk superconductivity, but a gradual transition towards low temperatures. From the latter behavior they estimated the superconducting volume fraction of 20 % at most. In the case of the measurements after rapid cooling, according to the authors, the superconducting fraction is reduced to 1 - 2 %.

[9] In order to avoid any confusion, T_p is used here to refer to the anomalous behavior of $\alpha(T)$ and $R(T)$ in the vicinity of the critical end-point (P_0, T_0) for κ-D8-Br.

[10] In employing $\alpha = -80 \cdot 10^{-6}\,\mathrm{K}^{-1}$, obtained from the height of the anomaly in the thermal expansion coefficient for crystal #1 (Fig. 4.14), using the entropy change $\Delta S = -0.074\,\mathrm{Jmol}^{-1}\mathrm{K}^{-1}$ at the Mott MI transition, whose detailed deduction is presented in Section 4.6.2, results in a jump of the specific heat of about $0.2\,\mathrm{Jmol}^{-1}\mathrm{K}^{-1}$. Details of this estimate are provided in Appendix 2. This value corresponds roughly to 0.4% of the background at T_{MI} in the specific heat (specific heat measurements on κ-D8-Br crystal #1 performed by Sebastian Köhler - Physics Institute - group of Prof. Dr. Michael Lang - Goethe University - Frankfurt (M) - Germany), employing ac calorimetric method, so that no signatures in the specific heat at T_{MI} could be detected.

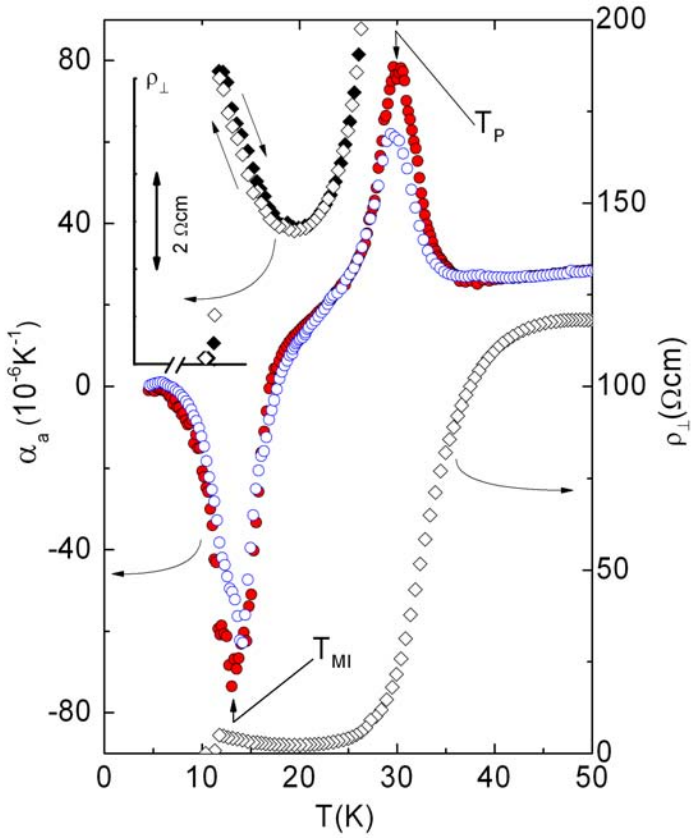

Figure 4.14: Thermal expansion coefficient (left scale) along the in-plane a-axis, $\alpha_a(T)$, for crystals #1 (red) and #2 (blue) and out-of-plane resistivity (right scale), $\rho_\perp$, for κ-D8-Br crystal #1. Upper inset shows a zoom of the low temperatures $\rho_\perp(T)$ data on the same T scale as used in the main panel.

reduction might be related to small misalignments of the crystal as well as to different pressures exerted by the dilatometer on the crystals, approximately 4 bar for crystal #1 and 6 bar for crystal #2. More information on the character of the transitions can be gained by looking at the relative length changes $\Delta l_i(T)/l_i$ = ($l_i(T)$ - l_i(300 K))/l_i(300 K), ($i = a, b, c$), shown in Fig. 4.15.

As Fig. 4.15 demonstrates, the dominant effects occur along the in-plane a-axis, i.e. parallel to the polymeric anion chains, see Fig. 4.5. Here a pronounced S-shaped anomaly is revealed at T_p which lacks any sign of hysteresis upon cooling and warming, at least in the resolution of the present experiments, a generic feature of a second-order phase transition with strong fluctuations. On further cooling through T_{MI}, the a-axis shows a rapid increase of about $\Delta a/a = 3.5 \cdot 10^{-4}$ within a narrow temperature range, indicative of a slightly broadened first-order transition. For the latter feature, the observation of a small but significant hysteresis of about 0.4 K, shown in the lower inset of Fig. 4.15, which complies with the hysteresis in $\rho_\perp(T)$ (upper inset Fig. 4.14), confirms the first-order character of the transition. The corresponding anomalies along the out-of-plane b-axis are less pronounced. Surprisingly, for the second in-plane c-axis, anomalous behavior in $\Delta l/l$ can neither be discerned at T_p nor at T_{MI}. The reliability of the previous results is supported by the same anisotropy observed for crystal #3, investigated in Ref. [103]. Based on the quasi-2D electronic structure of the present material, as shown in the upper

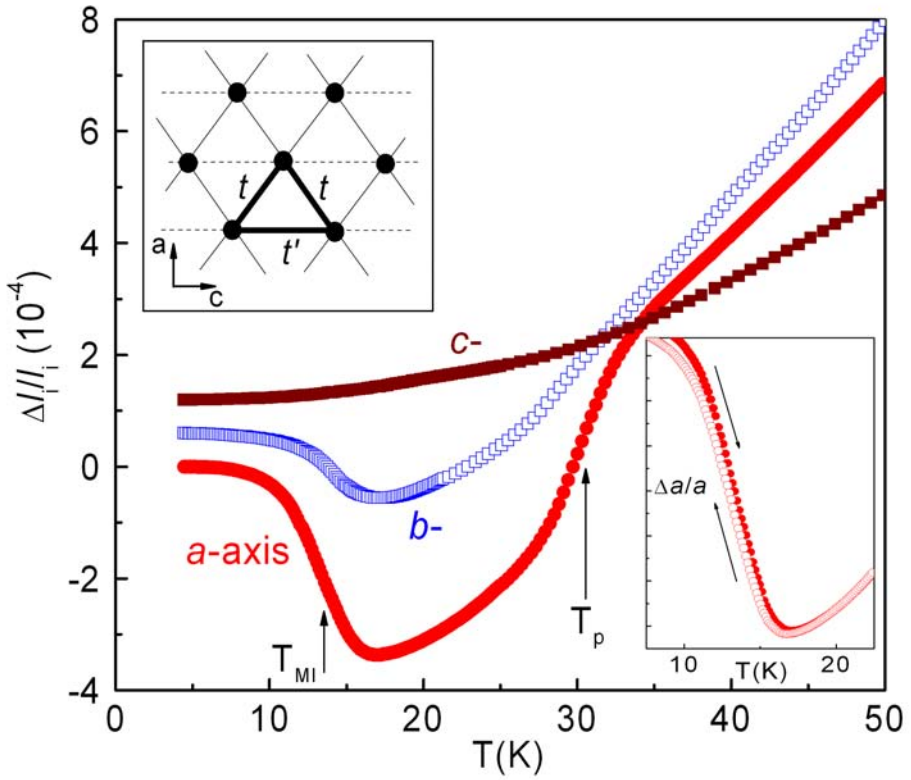

Figure 4.15: Relative length changes for κ-D8-Br crystal #1 along the in-plane a- and c- and out-of-plane b-axis. The data have been offset for clarity. Lower inset shows hysteretic behavior in $\Delta a/a$ at T_{MI} measured at very low sweeping rates of $\pm 1.5\,\mathrm{K/h}$. Upper inset depicts the 2D triangular-lattice dimer model with transfer integrals t and t', dots represent dimers of ET molecules.

inset of Fig. 4.15, which is characterized by dimers on a triangular lattice, the observed anisotropic lattice effects at the Mott transition is a very remarkable and unexpected result and deserves to be analyzed in more detail. The dominant effects in the *a*-axis, along which no dimer-dimer overlap exists, comply with the hypothesis that the diagonal hopping terms, t, play an important role in this process. Since these hopping terms have a component along the *c*-axis, which is likely to be even softer than the out-of-plane *b*-axis and second in-plane *a*-axis[11], a pronounced effect along the *c*-axis would then be automatically expected at T_{MI}. Note that along the *c*-axis a direct dimer-dimer interaction t', as indicated in the upper inset of Fig. 4.15, exists, making a zero-effect along this axis even more amazing. A possible explanation for this feature would be an accidental cancellation of counteracting effects associated with t and t', which seems to be unlikely. In addition, it is not clear how these in-plane interactions may produce comparatively strong effects in the out-of-plane *b*-axis. Another remarkable aspect is that the negative

[11] According to Ref. [117], the uniaxial compressibilities $k_i = 1/l_i(dl_i/dP)$ for the parent compound κ(ET)$_2$Cu(NCS)$_2$ are strongly anisotropic with $k_1 : k_2 : k_3 = 1 : 0.53 : 0.17$ (ratio estimated under 1 bar), where k_1 refers to the compressibility along the in-plane *c* direction, k_2 along the second in-plane *b*-axis and k_3 along the direction parallel to a projection of the long axis of the ET molecules, i.e. along the out-of-plane *a*-axis.

effect along the out-of-plane *b*-axis corresponds to a negative Poisson ratio [118]. These findings provide strong evidence that there should be a coupling of the π electrons to other degrees of freedom, namely to the lattice, thus indicating that the Mott MI transition in the present material cannot be understood by only taking into account a purely 2D electronic scenario [4].

4.6.1 Anisotropic Lattice Effects in κ-D8-Br and Rigid-Unit Modes

The relative length changes up to 200 K along the *a*-, *b*- and *c*-axes are shown in Fig. 4.16[12]. In the following, a possible explanation for the unusual anisotropic lattice effects observed in κ-D8-Br is presented.

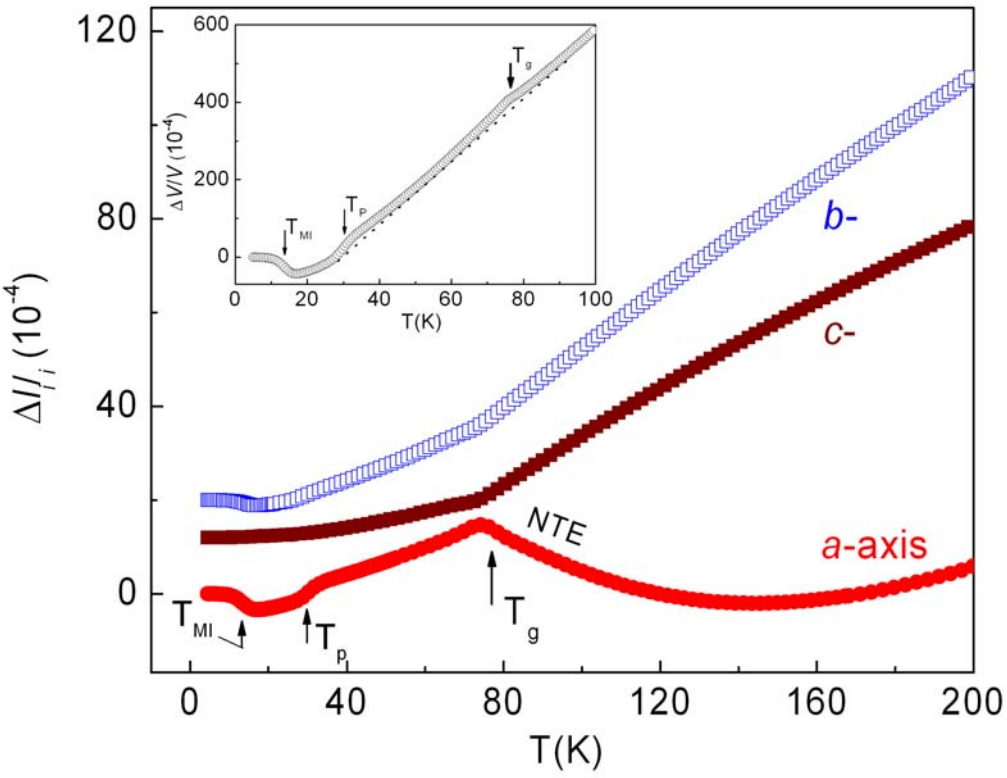

Figure 4.16: Main panel: Relative length changes along the in-plane *a*- and *c*-axis, and out-of-plane *b*-axis for κ-D8-Br crystal #1 up to 200 K. Data along the *b*- and *c*-axes are shifted for clarity. Position of T_g estimated according to [86]. NTE indicates negative thermal expansion along the in-plane *a*-axis in the range $T_g < T \lesssim 150$ K. Inset: Relative volume change $\Delta V/V = \Delta a/a + \Delta b/b + \Delta c/c$ versus T. Low temperature data will be used for estimating the entropy change associated with the Mott MI transition (Section 4.6.2).

Upon cooling, strongly anisotropic effects are observed. Note that more pronounced effects are observed along the in-plane *a*-axis, which is marked by a minimum around 150 K and an abrupt change in slope at T_g. This feature will be discussed in more detail below. An interpretation in terms of disorder due to the freezing-out of the orientational

[12]The correspondent thermal expansion coefficient for this data set can be encountered in Ref. [119].

degrees of freedom of the terminal ethylene groups was proposed by J. Müller *et al.* [86]. By substituting the terminal [$(CH_2)_2$] groups by [$(CD_2)_2$], one observes a shift of T_g to higher temperatures. A feature that is expected due to the higher mass of the [$(CD_2)_2$] in comparison to the mass of the [$(CH_2)_2$] groups, which in turn implies a higher relaxation time at a given temperature. Hence, the model proposed by J. Müller *et al.* is supported by the isotope effect, but it does not explain the negative thermal expansion along the in-plane *a*-axis observed above T_g, namely in the interval $T_g < T \lesssim 150$ K. Recently, high-resolution synchrotron X-ray diffraction experiments [120] have provided indications that such an anomaly is not solely linked to the freezing-out of the ethylene groups. The claims of the authors are based on the comparison between the estimated number of the disordered ethylene groups (staggered configuration) at 100 K (∼11 %) with those at extrapolated zero temperature (3 ± 3 %). They conclude that such transition is most likely related to structural changes, probably involving the insulating polymeric anion chains. Upon further cooling, the anomalies at T_p and T_{MI}, already discussed in detail in the previous section, show up. From Fig. 4.16 it becomes clear that the lattice effects at T_g, T_p and T_{MI} are more pronounced along the polymeric anion chain *a*-axis, being a negative thermal expansion (NTE), i.e. a decrease of length with increasing temperature, observed below T_{MI} (due to charge carriers localization) and also in the temperature window $T_g < T \lesssim 150$ K. It should be noted that the in-plane anisotropy at both T_{MI} and T_g corresponds to an orthorhombic distortion. Recently, NTE was also observed by Goodwin *et al.* in other materials containing cyanide bridges in their structures, cf. [121, 122] and references therein. These authors proposed a simple model [122] to explain the origin of this unusual behavior[13]. In this model, the transverse vibrational displacement of the CN units, away from the metal-metal axes (Fig. 4.17 b) and c)), is assigned to be the mechanism responsible for NTE in these materials.

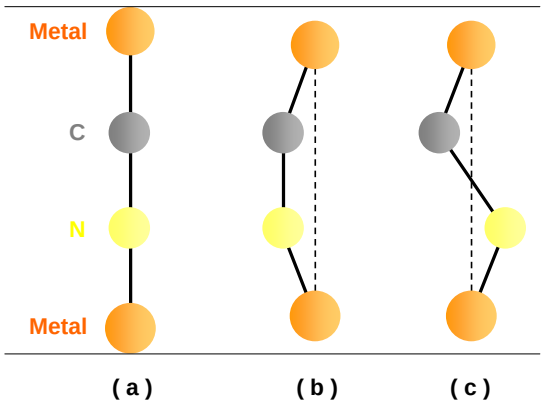

Figure 4.17: Schematic representation of the M-CN-M linkage. a) Linear configuration. b) Displacement of the C and N atoms away from the metal-metal axis in the same direction. c) Displacement in the opposite direction. Note that the total length along the metal-metal axis is reduced due to the displacement of the C-N atoms. This is the mechanism which gives rise to negative thermal expansion. Picture after Ref. [122].

[13] In fact, NTE is also observable in other materials. For example, the NTE of liquid water below 4 ^{0}C is connected with a breaking of the tetrahedral H bonding. Below 4 ^{0}C, NTE is required to overcompensate the increase of entropy due to such structural transition [10]. Another example can be found in ZrW_2O_8. This material exhibits NTE over a wide temperature window of 50 - 400 K [123]. The origin of this anomalous behavior is assigned to its structural arrangement, which is composed of rigid ZrO_6 octahedra and WO_4 tetrahedra. Rigid-unit modes in this material show up due to the fact that each WO_4 unit has one vertex not shared by another unit.

As can be seen from Fig. 4.17 b) and c), the displacement of the C and N atoms away from the metal-metal axis has the effect of decreasing the distance between the metal atoms as the temperature is increased. According to the authors of Ref. [122], in polymeric crystalline materials, these vibrational modes will not occur separately, but rather they will affect the vibration modes of other metal-CN-metal linkages, giving rise to NTE phenomenon. Nevertheless, the deformation of the metal-cyanide bridge will carry a high energy penalty. Hence, assuming that the metal coordination geometries are preserved, the vibration modes illustrated in Fig. 4.17 b) and c) can be observed only if they are coupled with the crystal lattice in the form of phonon modes. Yet, according to Goodwin *et al.*, such modes are referred to as rigid-unit modes (RUM) and can be experimentally observed in the low energy window 0 - 2 THz, i.e. in the range of typical phonon frequencies [124]. Given the polymeric nature of the anion $Cu[N(CN)_2]Br^-$ (Fig. 4.5), the above-described model is a good candidate to explain why NTE is observed only along the in-plane anion chain *a*-axis. The latter might have their origin in the RUM of dicynamide $[(NC)N(CN)]^-$ ligands along the anion polymeric chain. Note that the contraction of the lattice with growing T above T_g along the *a*-axis is accompanied by an expansion along the *b*- and *c*-axes (Poisson effect). In addition, preliminary Raman studies (not shown here) carried out on κ-D8-Br (crystal #4) in cooperation with Prof. Dr. Peter Lemmens and Patrick Scheib - Physikzentrum - TU Braunschweig - revealed the appearance of a double peak structure in the frequency window 50 - 200 cm^{-1} at 20 K (below T_g), not observed at 130 K (above T_g, but below the onset of NTE)[14]. Note that this frequency window fits roughly into the above-mentioned energy window predicted for RUM. Interestingly enough, the double peak structure is not observed at 5 K (below T_{MI}), indicating that vibration modes in this energy window are no longer active below T_{MI}. A more complex process should be involved in the negative thermal expansion expansion below T_{MI}, where a negative Poisson effect is observed. Hence, these results support the idea of strong coupling between lattice and electronic degrees of freedom at the Mott transition. Still owing to the anomalous lattice effects above T_g, based on the above discussion, it seems that the freezing out of the orientational degrees of freedom of the ethylene end-groups alone[15] cannot be responsible for a NTE along the *a*-axis. A possible scenario to explain this feature would be the existence of a complicated entwinement between the ethylene end groups and the vibration modes of the polymeric anion chain, not knowingly reported as yet in the literature. According to this idea, the ethylene end groups delimit cavities, where the anions are trapped [91], so that below T_g an anion ordering transition occurs in a similar way to the anion ordering transition observed in the quasi-1D $(TMTCF)_2X$ charge-transfer salts [146]. Further systematic Raman and infra-red studies are necessary to provide more information about the nature of the glass-like transition.

4.6.2 Entropy Change Associated with the Mott MI Transition

More information about the physics in the vicinity of the Mott MI transition can be obtained on estimating the entropy change associated with the MI transition. Employing the Clausius-Clapeyron equation (Eq. 2.25) with $\Delta V = (V_I - V_M)$ and $\Delta S = (S_I - S_M)$,

[14] Further studies are required to verify if such splitting shows up above or below T_p.

[15] As pointed out in Ref. [11], the glass-like anomaly is not observed in the organic superconductors β''-$(ET)_2SF_5CH_2CF_2SO_3$ (T_c = 5 K, large discrete anion) and in κ-$(ET)_2I_3$ (T_c = 3.5 K, linear anion) as well as in the nonsuperconducting α-$(ET)_2KHg(SCN)_4$ (polymeric anion), but a smooth Debye-like behavior along the three crystallographic directions up to 200 K. It is appropriate to mention here that the glass-like anomaly is not observed in the κ-$(ET)_2Cu_2(CN)_3$ salt, to be discussed in Section 4.8.

the respective difference in volume and entropy between the insulating (I) and metallic (M) states, and using $dT_{MI}/dP = (-2.7 \pm 0.1)$ K/MPa, which is obtained from the slope of the *S*-shaped line at T_{MI} in Fig. 4.8 and $\Delta V/V = (4.2 \pm 0.5) \cdot 10^{-4}$, derived from inset of Fig. 4.16, one finds $\Delta S = -0.074\,\mathrm{Jmol^{-1}K^{-1}}$. This small entropy change at T_{MI} represents only a fraction of the entropy associated with the metallic state of the κ-H8-Br salt at $T \simeq 14$ K of $S = \gamma \cdot T \simeq 0.375\,\mathrm{Jmol^{-1}K^{-1}}$, with a Sommerfeld coefficient γ = 0.025 $\mathrm{Jmol^{-1}K^{-2}}$ [125]. Electronic specific heat data published in the literature [126] revealed that by means of gradual deuteration it is possible to tune the system from the metallic to the insulating side of the phase diagram, thereby γ decreases towards zero in the insulating phase. Based on these literature results, one can assume that γ of the fully deuterated salt discussed here, above the T_{MI} should actually be significantly smaller than that of the fully hydrogenated salt. Hence, the small entropy change of $-0.074\,\mathrm{Jmol^{-1}K^{-1}}$ obtained here indicates that the high spin entropy of the paramagnetic insulator at elevated T must have been almost completely removed. In addition, this finding is consistent with the Néel temperature T_N coinciding with T_{MI} at this point in the phase diagram [119].

4.6.3 Magnetic-Field Effects on κ-D8-Br

Based on the previous sections, more insights into the role of the lattice degrees of freedom for the Mott insulating state in κ-D8-Br can be gained by thermal expansion experiments under magnetic fields. In the following, the effects of magnetic fields in the vicinity of the Mott MI transition are discussed. Before doing so, it is advisable to carefully analyze the low-temperature range in zero magnetic field. The thermal expansion coefficient along the out-of-plane *b*-axis in zero magnetic field is displayed in Fig. 4.18 together with the resistance[16] data normalized to its value at room temperature. Upon cooling, a negative anomaly around T = 13.6 K is observed. The latter is associated with the Mott MI transition and reflects the change of the lattice parameter upon crossing the first-order MI line, as discussed in previous sections. The anomaly in $\alpha(T)$ is directly correlated with an increase of the resistance around the same temperature, which confirms that the anomaly in $\alpha(T)$ is undoubtedly related to the Mott MI transition. The drop of the resistance at T_c = 11.6 K, accompanied by a tiny kink (indicated by the arrow) in $\alpha(T)$, are signatures of percolative SC in minor portions of the sample volume coexisting with the AFI ordered state, see e.g. [134]. In the temperature range 13 K $\lesssim T \lesssim$ 15 K, a jump in the resistivity data is observed. In fact, such jumps in resistivity measurements are frequently observed in organic charge-transfer salts. The huge expansivity of the crystal induces stress on the electrical contacts giving rise to such jumps. In general, the appearance of jumps in resistivity data are attributed to cracks. For the (TMTTF)$_2$X and (TMTSF)$_2$X salts, in particular, such jumps in resistivity are assigned to stress caused by localized defects and/or by mechanical twinning [76].

Fig. 4.19 shows the thermal expansion coefficient along the *b*-axis at low temperatures under magnetic fields of 0.5, 1, 2, 4, 6 and 10 T. The first physical information obtained from these data is that upon cooling under magnetic field up to 10 T, T_{MI} remains unaffected, at least within the resolution of our experiments. Upon further cooling under a low field of 0.5 T, however, a second anomaly around T_{FI} = 9.5 K (FI refers to field-induced) takes place. The latter becomes even more pronounced under 1 and 2 T and saturates under a field of $\sim$4 T. A careful analysis of the data in Fig. 4.19 reveals the existence of a double-peak structure for fields exceeding 1 T. Nevertheless, further

[16] Resistance measurement shown in Fig. 4.18 was carried out by Christian Strack, Ph.D. thesis (in preparation), Goethe University - Frankfurt (M) - Germany.

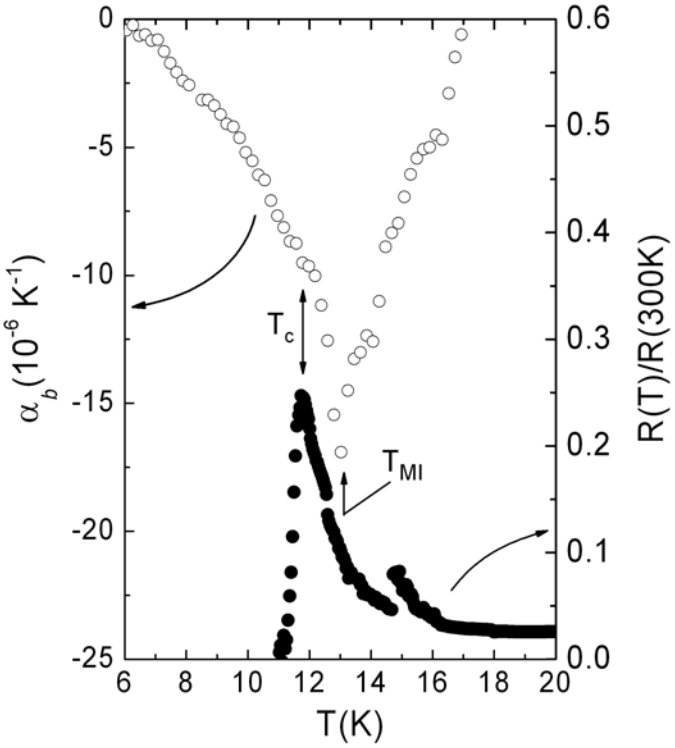

Figure 4.18: Thermal expansion coefficient along the *b*-axis (left scale) together with the resistance data normalized to its value at room temperature (right scale) for κ-D8-Br crystal #3. T_{MI} refers to the MI transition temperature and T_c denotes the percolative SC critical temperature. Jumps in the resistance around 13 K and 15 K are most likely related to the large expansivity of the material in this temperature range, as discussed in the text.

experiments are required in order to obtain more information on this issue. No such field-induced effects were observed along the *a*- and *c*-axis (not shown). As known from the literature, orientational field-dependent magnetic phenomena may indicate a spin-flop (SF) transition. The SF transition occurs when the system is in an AFI state and a magnetic field, exceeding a certain critical value (critical field), is applied parallel to the easy-axis. In the present case, this field dependence of $\alpha(T)$ is indicative of a SF transition with strong coupling between the spin and lattice degrees of freedom. As can be seen from Fig. 4.19, $H_c < 0.5$ T (H_c refers to the critical field) for κ-D8-Br, which is consistent with a critical field $H_c \sim 0.4$ T for the chlorine salt, deduced in Ref. [129]. The reason why the anomaly in $\alpha(T)$ at $T = T_{FI}$ becomes more pronounced for fields higher than H_c, however, cannot be explained by the hypothesis of a SF transition, so that an additional phenomenon should be related to this feature. As pointed out by Ramirez *et al.* in Ref. [136], the appearance of sharp peaks in thermodynamic quantities, like specific heat or thermal expansion, under finite magnetic fields have been observed in a few systems and constitute a rare physical phenomenon. In the following, two possible scenarios are discussed to explain this unusual feature: i) Resistance measurements on 50 % and 75 % deuterated κ-(ET)$_2$Cu[N(CN)$_2$]Br under field sweep (field applied along the out-of-plane *b*-axis) at $T = 5.50$ and 4.15 K, respectively, revealed an abrupt change from SC to high resistive states for fields exceeding 1 T [135]. This behavior is interpreted by the authors as being evidence of a FI first-order SC-to-Insulator transition. Hence,

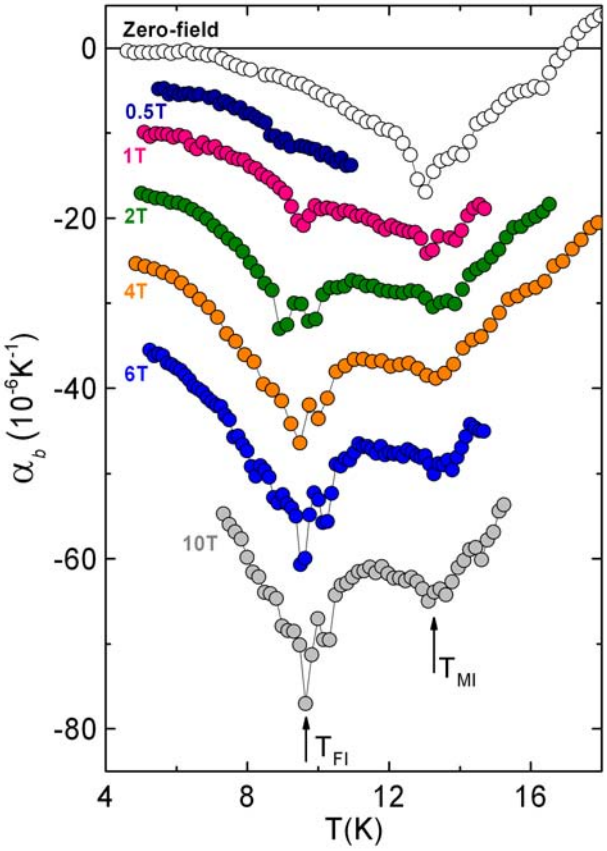

Figure 4.19: Thermal expansion coefficient perpendicular to the conducting layers under selected fields, as indicated in the label of figure, for κ-D8-Br crystal #3. T_{MI} refers to the metal-insulator transition temperature and T_{FI} to the field-induced phase transition temperature, as discussed in the main text.

based on these observations, for fields exceeding H_c the present results may be interpreted as evidence for the suppression of the percolative SC, giving rise to an insulating state induced by magnetic field, which in turn is accompanied by an abrupt change of the lattice parameter. ii) A second interpretation for these sharp peaks in α_b induced by magnetic field is that upon exceeding the critical field H_c, percolative superconductivity is destroyed, the remaining electrons spin do not couple with the applied magnetic field due to the correlated motion among them. These field-decoupled spins[17] are strongly coupled to the lattice and give rise to the minimum at T_{FI}. The present results do not enable us to determine the exact orientation of these field-decoupled spins. It is important

[17]The term field-decoupled spins is used in Ref. [136] to refer to similar effect (double peak structure) observed in specific heat measurements under magnetic field for the "spin ice" compound $Dy_2Ti_2O_7$. According to the authors of Ref. [136], when a magnetic field is applied parallel to the [100] crystallographic direction, due to correlated motion among the spins, half the spins have their Ising axis orientated perpendicular to the magnetic field. The latter are called decoupled-field spins. It was observed that magnetic fields exceeding a certain critical value lead to the ordering of these field-decoupled spins. Monte Carlo calculations, also reported by the authors in Ref. [136], support the proposed model. The term "spin ice" is used by the authors to refer to the spin orientations in analogy with the degeneracy of ground states observed in ice (H_2O in solid phase), where hydrogens atoms are highly disordered and gives rise to a finite entropy as $T \rightarrow 0$. This is because the oxygen atoms form a well defined structure, but the hydrogen atoms remain highly disordered due to two inequivalent O-H bond lengths, as first pointed by L. Pauling [137].

to stress here that the above-discussed scenarios are "possible scenarios", so that the actual physical origin of the features observed at T_{FI} remains unclear. Another remarkable feature in Fig. 4.19 is, that for fields $H > H_c$ in a temperature window between T_{MI} and T_{FI}, an intermediary phase appears, probably paramagnetic, indicated in the schematic phase diagram shown in Fig. 4.20. It could be speculated that this feature can be seen as a separation of the T_N and T_{MI} lines in the phase diagram. A possible physical description to this would be related to the energetic competition between the AFI ordered and the paramagnetic phases after crossing the MI first-order line, resulting thus in a decrease of T_N with increasing of magnetic field. Similar experiments were carried out in two other κ-D8-Br crystals (crystals #1 and #2). For both crystals, however, in contrast to the sharp anomaly at $T_{FI} \approx 9.5$ K under magnetic fields shown in Fig. 4.19, the effects of magnetic fields result in a smooth change of $\alpha(T)$ around the same temperature. Two factors should be considered as a possible explanation to this: i) crystal alignment upon mounting the sample into the dilatometer. As reported in the literature, see e.g. [138], SF transitions are strongly dependent of the direction of the applied magnetic field. A minute misalignment between the magnetic field and the easy-axis can give rise to a suppression of the transition; ii) sample inhomogeneities. This would imply, for instance, that portions of percolative SC vary from sample to sample, reflecting therefore differences in their magnetic properties [3].

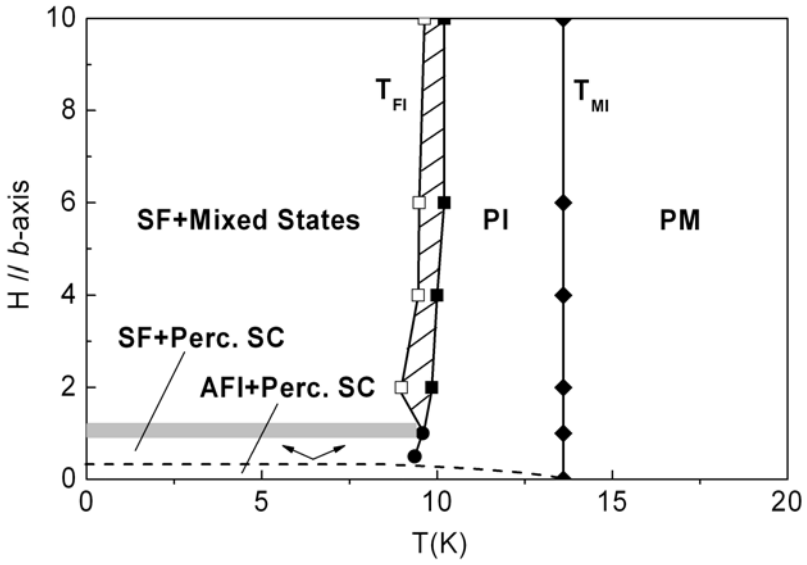

Figure 4.20: Speculative H-T diagram for κ-D8-Br for magnetic fields applied along the easy-axis (*b*-axis). Symbols refer to the peak anomaly in $\alpha(T)$. Lines represent the various phase transitions discussed in the main text. PM and PI denote paramagnetic metal and paramagnetic insulator, respectively. Hatched region indicates T window in which a double-peak structure in $\alpha(T)$ is observed. SF stands for spin-flop and Mixed States refers to a possible coexistence of spin-flopped and field-decoupled spins, as discussed in the text.

The present findings are summarized in the schematic diagram depicted in Fig. 4.20. The dashed line around $\sim$0.5 T separates the AFI from the SF phase, while the thick line marks the (partial) suppression of percolative SC giving place to field-decoupled and/or flopped spins, referred to as mixed states. Concluding this section, the thermal expansion findings on κ-D8-Br under magnetic field reveal the insensitivity of the Mott

MI transition temperature under fields up to 10 T, which is in accordance with the proposal of a Mott insulating state with a hole localized in a dimer. A field-induced phase transition at T_{FI} = 9.5 K is observed, indicative of a SF transition with strong magnetoelastic coupling, accompanied by an enhancement of $\alpha(T)$ due to the suppression of the percolative SC under magnetic fields above 1 T. Further experiments, like magnetostriction measurements, will shed more light on the above-discussed magnetic field-induced effects.

4.6.4 Thermal Expansion Under Quasi-Uniaxial Pressure

Given the high anisotropy of the κ-(ET)$_2$X charge-transfer salts, thermal expansion measurements under quasi-uniaxial pressure could provide more insights to better understand the transitions at T_{MI}, T_p and T_g. The effect of quasi-uniaxial pressure on the sample was studied for crystal #2 as shown in Fig. 4.21. In these experiments, a pressure of (65 $\pm$ 5) bar was applied along the out-of-plane *b*-axis. Roughly speaking, pressure application along the *b*-axis means a change of the contact between the polymeric-anion chains and the ET molecules and/or enhancement of the tilt of the ET molecules.

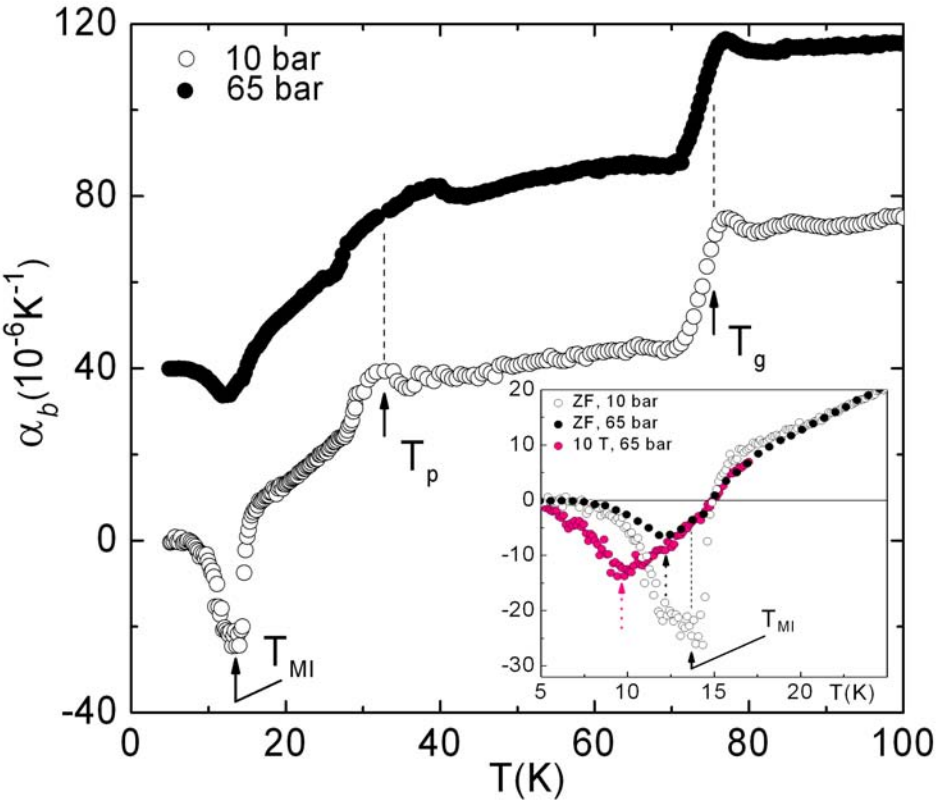

Figure 4.21: Main panel: Thermal expansion coefficient along the out-of-plane *b*-axis for κ-D8-Br crystal #2 under ambient (10 bar) and quasi-uniaxial pressure of 65 bar. Dashed lines are guide for the eyes. Data are shift for clarity. Inset: blowup of the low-T $\alpha_b(T)$ data together with measurement under pressure (65 bar) and magnetic field of 10 T. ZF refers to zero magnetic field. Black dashed arrow indicates the peak position under quasi-uniaxial pressure of 65 bar, while pink dashed arrow highlights a shift of the peak position to lower T when a magnetic field of 10 T is applied.

As can be seen in the main panel of Fig. 4.21, a quasi-uniaxial pressure of 65 bar is enough to change the shape of the thermal expansion curves at T_{MI} and T_p dramatically. These findings reveal that the anomalies in $\alpha(T)$ at T_{MI} and T_p are strongly affected upon applying pressure, while T_g remains practically unaffected. Since κ-D8-Br is located on the boundary of the Mott MI insulator transition (Fig. 4.8), this feature might be associated with a shift of its position from the insulating to the metallic side of the phase diagram. Assuming the peak position T_{MI} = 13.6 K as the transition temperature under ambient pressure (actually under roughly 10 bar) and T_{MI} = 11.8 K[18] as the transition temperature under quasi-uniaxial pressure (65 bar), one obtains $dT_{MI}/dP_b \simeq -33$ K/kbar. This value is roughly one order of magnitude smaller than the hydrostatic pressure dependence of T_{MI} ($dT_{MI}/dP \simeq -380$ K/kbar), estimated from the slope of the MI line in Fig. 4.8 at T = 11.8 K. Such discrepancy might reflect the anisotropy in the uniaxial-pressure effects. However, the shift of T_p (T_{MI}) to high (low) temperatures is in prefect agreement with a positive (negative) pressure dependence of T_p (T_{MI}) in the phase diagram (Fig. 4.8). Applying a magnetic field of 10 T (pink curve in the inset of Fig. 4.21), the peak position of the transition, indicated by black and pink dashed arrows, shifts to lower temperatures. As T_{MI} is insensitive to magnetic fields up to 10 T (Section 4.6.3), this observation suggests that the anomaly in $\alpha(T)$ under quasi-uniaxial pressure should be triggered by superconductivity. The present thermal expansion results under quasi-uniaxial pressure can be seen as a starting point for experiments under hydrostatic pressure (in preparation), which will provide important information about the physics in the vicinity of the Mott MI transition region in the phase diagram.

4.6.5 Influence of the Cooling Speed on T_g in κ-D8-Br

In this section, the influence of the cooling speed through the glass-like ($T_g \approx 77$ K) transition on T_{MI} and T_p is discussed. In fact, the role of the cooling speed on the physical properties of fully and partially deuterated salts of κ-(ET)$_2$Cu[N(CN)$_2$]Br has been intensively discussed in the literature, e.g. in Refs. [134, 139]. As shown in Fig. 4.22, the thermal expansion coefficient along the in-plane *a*-axis for a crystal of κ-D8-Br was measured after cooling the sample through the so-called glass-like phase transition by employing two distinct cooling speeds (-3 K/h and -100 K/h).

A broadening of the transition, accompanied by a reduction in the size of the peak anomaly at $T_p \simeq 30$ K, which is related to the critical end point of the first-order line in the phase diagram, and the Mott MI temperature $T_{MI} \simeq 13.6$ K, is observed for fast cooling (-100 K/h). Another remarkable feature is that the peak position of the T_p = 30 K anomaly shifts toward lower temperatures, while the anomaly at T_{MI} = 13.6 K shifts slightly to higher temperatures. Based on these observations, one can conclude that the increase of the cooling speed through T_g results in an opposite effect to that observed upon applying quasi-uniaxial pressure (Section 4.6.4). The observed shift of T_g towards higher temperatures under fast cooling is in agreement with literature results [86]. Resistivity measurements on κ-D8-Br salts [96,140], synthesized by employing the same method as that used for the salts studied in this work, revealed that by fast cooling speed[19] the resistance increases dramatically below $T_g \simeq 80$ K, superconductivity is suppressed giving way to a residual resistance ratio of $\sim$5. This feature together with the observed enhancement of

[18] T_{MI} is used here to refer to the MI transition temperature. However, this transition might eventually be related to the pressure-induced bulk superconduting transition, i.e. a shift of κ-D8-Br from the insulating to the metallic side in the phase diagram induced by quasi-uniaxial pressure.

[19] In Ref. [96] Griesshaber refers to a cooling rate of ~ -1 K/min as a slow cooling, while the rapid cooling rate is not mentioned.

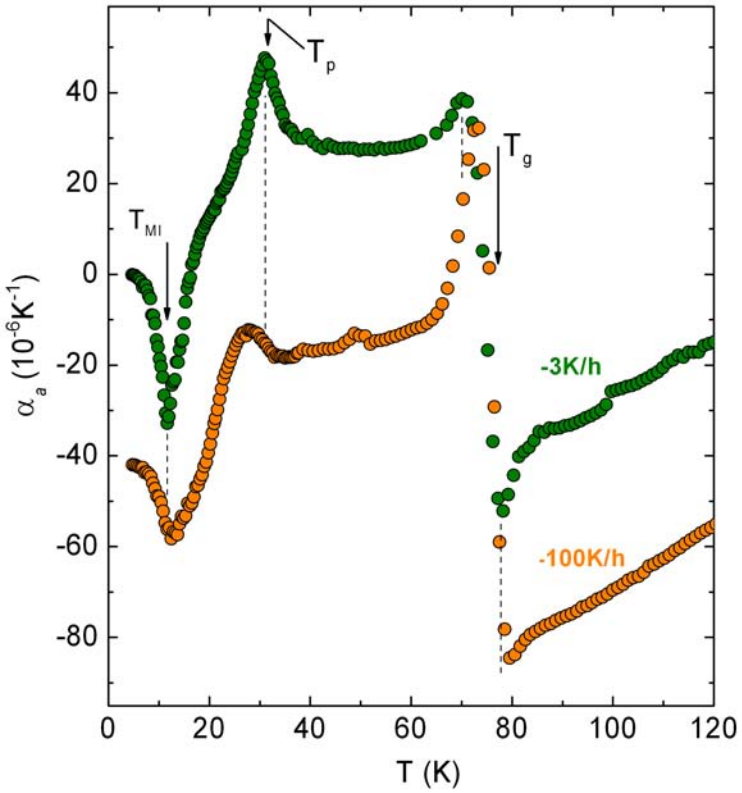

Figure 4.22: Thermal expansion coefficient as a function of temperature for κ-D8-Br crystal #3 along the in-plane *a*-axis. Measurements taken on warming after employing different cooling speeds (-3 K/h and -100 K/h). Data are shifted for clarity. Arrows indicate the respective phase transitions for the slowly cooled crystal. Dashed lines are used to show the shift of T_{MI} (towards higher temperatures), T_p (towards lower temperatures) and T_g (towards higher temperatures) under fast cooling across T_g.

the anomaly in α_a on fast cooling (Fig. 4.22) can be assigned to an increase of the scattering provoked by the randomly distributed potential of the polymeric Cu[N(CN)$_2$]Br$^-$ anion. A similar situation is encountered in the quasi-1D (TMTSF)$_2$ClO$_4$ superconductor salt, where by rapid cooling (>50 K/min) superconductivity is destroyed giving way to a first-order anion-ordering transition at T = 24 K, which in turn is accompanied by a SDW transition around 6 K [76].

4.7 Mott Criticality

In this section the critical behavior at the end-point of the first-order line will be discussed. As mentioned in the previous section, the thermal expansion coefficient is related to the specific heat via the Grüneisen relation (Eq. 2.16). This implies that in the vicinity of the transition at T_p, the same scaling laws apply and, as a consequence, the same critical behavior should be obeyed for both quantities. This approach has been verified by various groups, see e.g. [21, 141]. Hence, the observation of the huge anomaly observed in the thermal expansion coefficient at T_p, cf. Fig. 4.14, exceeding the back-

ground expansivity by a factor 3 - 4, has prompted the study of the critical behavior by means of a thermodynamic probe[20] with high sensitivity. Fig. 4.23 shows the phase transition anomaly in $\alpha_a(T)$ for crystals #1 and #2 on expanded scales. As can be seen, for both samples the transition is not very sharp, rather yielding some broadening in a temperature window of several Kelvin.

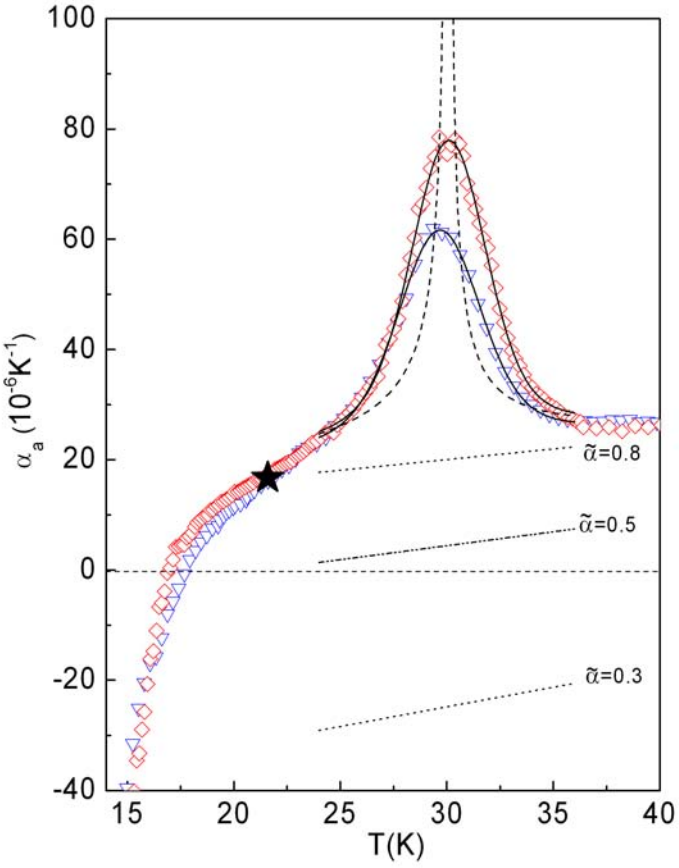

Figure 4.23: Expansivity along the a-axis for κ-D8-Br crystals #1 ($\diamond$) and #3 ($\bigtriangledown$) near T_p. Solid lines are fits as described in the text for $\tilde{\alpha}$ = 0.8 with a Gaussian distribution of T_p. Dashed line represents the pure singular contribution for crystal #1. Straight lines show background contributions implied in fits for $\tilde{\alpha}$ values given in the figure. Star marks the universal background point discussed in the text.

In the outer flanks of the maximum, the slope of $\alpha(T)$ increases steeply. Closer to the center of the peak, however, the slope is significantly reduced giving rise to a rounded maximum. Such broadening effects are generally encountered in the immediate vicinity of the transition and are attributed to sample inhomogeneities. In the following, the fitting procedure employed to study the criticality around (T_0, P_0) is discussed in details. The anomalies will be analyzed in terms of a power-law behavior in the reduced temperature variable t. The smearing of the transition is accounted for by a Gaussian dis-

[20]Employing the Ehrenfest relation (Eq. 2.26), the size of the anomaly expected at T_p in the specific heat can be estimated. Taking the anomaly height $\Delta\alpha$ = 80 $\times$ 10^{-6} K^{-1}, the molar volume V_{mol} = 5 $\times$ 10^{-4} m^3/mol, dT_p/dP = 100 K/kbar estimated from the slope in Fig. 4.8 and T_p = 30 K results in ΔC = 1.2 Jmol^{-1} K^{-1}. Specific measurements around T_p have not been reported in the literature.

tribution for T_p with width δT_p[21]. The function used in the fittings of the linear thermal expansion coefficient in the temperature range 24 - 36 K is given by:

$$\alpha(T) = \int \underbrace{\frac{A^{\pm}}{\tilde{\alpha}} \mid t \mid^{-\tilde{\alpha}}}_{\text{Singular contribution}} \underbrace{G(\overline{T}_p, T_p, \delta T_p)}_{\text{Distribution of the transition temperatures}} dT_p + \underbrace{B + ET}_{\text{Non-singular contributions including phonons}} \tag{4.1}$$

As indicated in Eq. 4.1, the first term in the integral describes the singular contributions with the amplitudes A^+ and A^- for $t > 0$ and $t < 0$, respectively, while the linear term comes from the phonons, but can also include a small non-singular electronic contribution. The estimation of this linear term deserves special attention. Fig. 4.24 shows the expansivity for samples #1, #2, #3 and κ-H8-Br #7. A careful analysis of these data sets reveals that, independent of the presence and size of the critical contribution at T_p, all curves intersect at a single point (T, α) $\simeq$ (21 K, 16 $\times$ 10^{-6} K^{-1}), indicating thus that this point should reflect the pure non-singular background contribution. Hence, a constraint to a meaningful background is that it should extrapolate to this point.

Using Eq. 4.1, simultaneous fits were performed on crystals #1 and #2 assuming the same linear background, same amplitude ratio A^+/A^-, same critical exponent $\tilde{\alpha}$, but individual T_p values, since the critical temperatures for both crystals differ slightly. A good fit for both data sets, also satisfying the above-mentioned background, is obtained for $\tilde{\alpha}$ = 0.8, A^+/A^- = 0.79, and $\bar{T}_p$ = 30.1 K, δT_p = 1.59 K for crystal #1 and $\bar{T}_p$ = 29.6 K, δT_p = 1.74 K for crystal #2, cf. solid line in Fig. 4.23. It should be mentioned that $\tilde{\alpha}$ values in the range 0.65 - 0.95, with small changes in the other parameters accordingly, result in fits of similar quality and still comply with the background constraint. In contrast, the residual of the fit increases substantially upon decreasing $\tilde{\alpha}$ to well below 0.65. This is accompanied by a suppression of the background to even negative values for $\tilde{\alpha} < 0.5$, clearly incompatible with the background constraint (see for example, the background implied by the fits for $\tilde{\alpha}$ = 0.5 and 0.3 in Fig. 4.23). As clearly indicated by these simultaneous fits, and confirmed by independent fits to the individual data sets for crystals #1 and #2, a large positive critical exponent $\tilde{\alpha}$ is the only possible, physically meaningful description of the expansivity data. The critical exponent derived here of ($\tilde{\alpha} \simeq 0.8 \pm 0.15$) is much larger than those of known universality classes with $-0.12 \leq \tilde{\alpha} \leq 0.14$ (Table 2.2) and the mean-field value $\tilde{\alpha}$ = 0 observed at the Mott critical endpoint of Cr-doped V_2O_3 [102]. In particular, it greatly conflicts with the criticality reported in Ref. [22] from conductivity measurements on pressurized X = Cu[N(CN)$_2$]Cl. Employing the universal relation (Eq. 2.32), the exponents found there of $(\delta, \beta, \gamma) \approx (2, 1, 1)$ give $\tilde{\alpha} = -1$. The reason for this discrepancy is unclear but might be related to the significant broadening effects, which have not been included in the analysis in [22]. The exponent found here, however, is

[21] This analysis is consistent with the idea that in the critical region, the internal energy of the lattice depends strongly upon $T - T_p$, while T_p in turn depends on the lattice constant. This is equivalent to assume that $t = (T - T_p(T))/T_p$, so that in the critical region a distribution of T_p values has to be taken into account in order to look for a power law to compare with a theoretical approach which assumes fixed lattice constants. This aspect was discussed by Kadanoff *et al.* in Ref. [18] p. 408.

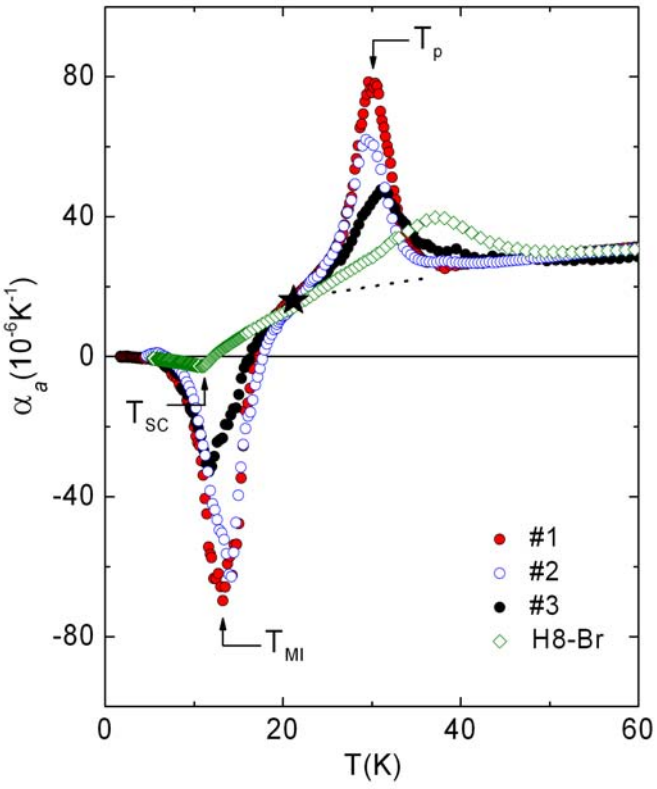

Figure 4.24: Blow-up of the expansivity data along the in-plane *a*-axis for three different samples of κ-D8-Br and one sample of κ-H8-Br (data taken from [103]). Dotted line represents the background for the critical exponent $\tilde{\alpha}$ = 0.8, shown in Fig. 4.23. Star indicates the universal background point, as discussed in the main text.

rather close to $\tilde{\alpha}$ = 0.5 expected for a tricritical[22] point [15]. Such a scenario would imply a symmetry breaking associated with the Mott MI transition. Interestingly enough, an even larger exponent $\tilde{\alpha}$ = 0.93 was reported for the compound $La_{0.7}Ca_{0.3}MnO_3$ [141], also characterized by a strong electron-phonon coupling, showing a similar $\alpha(T)$ anomaly to the one observed here for κ-D8-Br.

4.8 Thermal Expansion Measurements on κ-(ET)$_2$Cu$_2$(CN)$_3$

Fig. 4.25 shows the thermal expansion coefficient along the in-plane *c*-axis for crystal #1 of the entitled salt. Upon cooling, α_c decreases monotonously down to T_{min} $\simeq$ 30 K. Around T = 150 K, indications of a small and broad hump are observed. In Ref. [110], Shimizu and collaborators observed an enhancement of the spin relaxation rate above 150 K, which was attributed to the freezing of the thermally activated vibration of the ethylene end groups. Note that no traces of a glass-like anomaly around T = 77 - 80 K are observed. This behavior is quite distinct from that observed in κ-

[22] A tricritical point is defined as the point where a first-order transition evolves into a second-order phase transition [15].

(ET)$_2$Cu[N(CN)$_2$]Cl [86] and κ-D8-Br (discussed in previous section) and κ-H8-Br [86], where clear signatures in the thermal expansion coefficient show up at $T_g \simeq 77$ K. This discrepancy indicates that the lattice dynamic for the κ-(ET)$_2$Cu$_2$(CN)$_3$ salt is different from that of the above-mentioned compounds. In fact, according to the RUM model, discussed in previous sections, the absence of a glass-like anomaly in κ-(ET)$_2$Cu$_2$(CN)$_3$ can be understood in the following way: the anion $Cu_2(CN)_3^-$ (Fig. 4.6) consists of a 2D network of Cu(I) and bridging cyanide groups [92]. As the $Cu_2(CN)_3^-$ anion is arranged in a network fashion, which is quite different from the polymeric arrangement of Cu[N(CN)$_2$]Cl$^-$ and Cu[N(CN)$_2$]Br$^-$ (Fig. 4.5), the vibration modes of the CN groups are confined between nearest Cu(I) atoms, so that they cannot propagate along the structure. Hence, the formation of RUM in κ-(ET)$_2$Cu$_2$(CN)$_3$ is very unlikely and as a consequence no signatures of the glass-like transition can be observed. Cooling the system further, another broad hump is observed at $T_{max,\chi} \simeq 70$ K. The latter coincides roughly with a broad maximum observed in magnetic susceptibility measurements [110]. Below $T \simeq 50$ K, α_c assumes negative values. Cooling the system further, a broad minimum is observed at $T_{min} \simeq 30$ K. Below $T \simeq 14$ K, α_c starts to assume positive values. A possible scenario for explaining the negative thermal expansion in the range $14\,\mathrm{K} \lesssim T \lesssim 50\,\mathrm{K}$ is discussed in the following. In this temperature range, lattice vibration modes (most likely from the anion) become soft, the Grüneisen parameter in turn assumes negative values and the lattice expands upon cooling[23]. However, the hypothesis of negative thermal expansion driven by spin degrees of freedom cannot be ruled out. In fact, the connection between negative thermal expansion and frustration has been reported in the literature, but a theory able to describe this phenomena is still lacking [143]. Amazingly, upon further cooling, a huge anomaly is observed at $T^{anom} \simeq 6$ K. The latter coincides with the hump anomaly observed in specific heat measurements [5]. This finding constitutes the first observation of lattice effects associated with the transition (or crossover/hidden ordering) at 6 K. A further analysis of the present data is difficult because the actual phonon background cannot be estimated. The low-temperature data will be discussed in more detail in the following. Fig. 4.26 (a) shows the thermal expansion coefficient below 14 K on expanded scales.

Upon cooling below 6 K, a hump at $T \simeq 2.8$ K is observed. Several runs were performed in order to check for reproducibility. The latter feature has not been observed in specific heat measurements [5], most likely due to the lack of resolution of such experiments.

The signatures observed in α_c have their direct correspondence in the spin-lattice relaxation rate (T_1^{-1}) and magnetic susceptibility (χ) [110]. Below 50 K, both quantities decrease monotonously with temperature down to 4 K, where T_1^{-1} starts to increase and shows a broad maximum at 1 K, while χ varies smoothly [110]. Thermal expansion measurements under magnetic fields (inset of Fig. 4.27) revealed that under 8 T, the peak position around 6 K as well the hump at $T \simeq 2.8$ K remains unaltered, in agreement with specific heat measurements under magnetic field [5], indicating therefore that the anomaly at 6 K is unlikely to be due to long-range magnetic ordering, at least for magnetic fields applied parallel to the *c*-axis[24]. In addition, measurements on cooling and warming (main panel of Fig. 4.27) revealed no traces of hysteretic behavior, at least in the resolution of the present experiments, so that the hypothesis of a first-order transi-

[23] Interestingly enough, negative thermal expansion has been also observed in amorphous $Y_{100-x}Fe_x$ (x = 92.5 and 84) alloys over the temperature range, in which these systems go from the paramagnetic to the spin-glass state. The latter feature is assigned to the thermal variation of spin fluctuations [142].

[24] It is worthwhile mentioning that for the "spin ice" system $Dy_2Ti_2O_7$ [136], already mentioned previously, the spins disorder is suppressed when magnetic field is applied perpendicular to the their Ising axis.

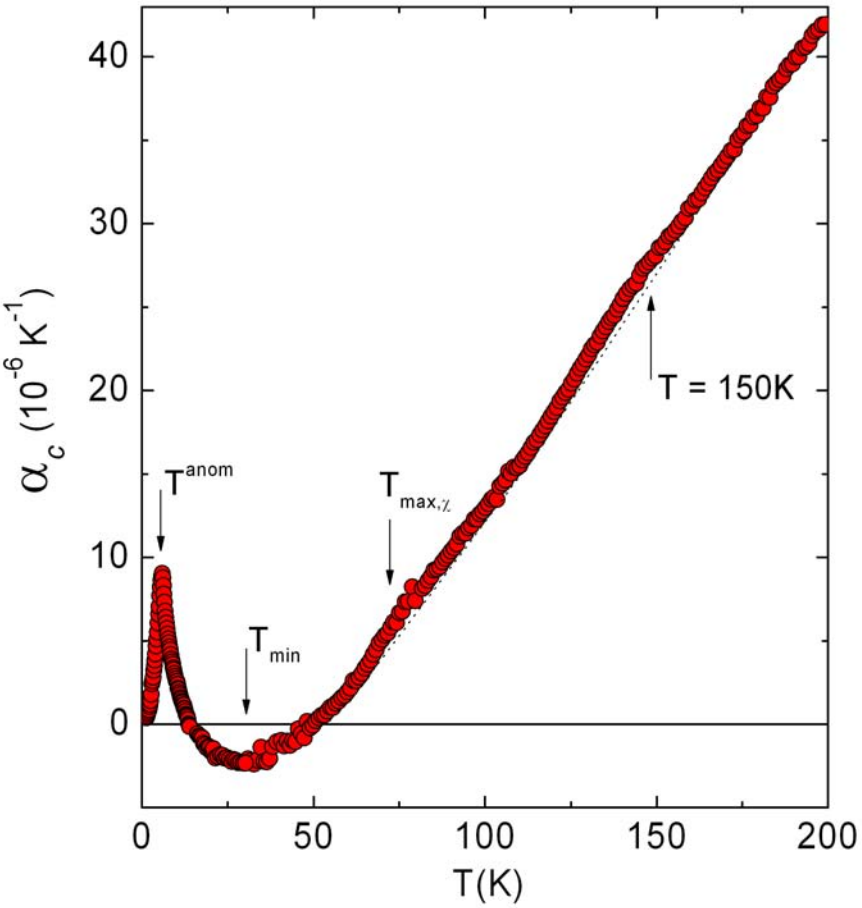

Figure 4.25: Expansivity along the in-plane *c*-axis for a single crystal of κ-(ET)$_2$Cu$_2$(CN)$_3$. T^{anom} indicates the temperature at which, according to Ref. [5], the crossover (hidden ordering) to a spin-liquid state occurs. The dashed line is used to indicate an hypothetical linear background. Broad hump anomalies at $T \simeq 150$ K and $T_{max,\chi} \simeq 70$ K are indicated by the arrows, cf. discussed in the text.

tion can be ruled out.

Hence, the actual origin of the anomaly in α_c at 6 K remains unclear. However, at first glance, the present thermal expansion findings appear to fit in the model proposed by Lee *et al.* [115]. As discussed briefly in Section 4.5, according to this model, spin pairing on the Fermi surface generates a spontaneous break of the lattice symmetry giving rise to a phase transition at finite temperature, which in turn is coupled to a lattice distortion. In other words, upon cooling, the spin entropy has to be (partially) frozen. The only way for this, without long-range magnetic ordering, is to introduce a lattice distortion. This process presents some similarities with a classical Spin-Peierls transition, where the formation of a singlet state requires that the spin entropy of the triplet state goes to zero by introducing a lattice distortion. In the present case, the amount of entropy in the temperature range $0.3\,\mathrm{K} < T < 1.5\,\mathrm{K}$ corresponds to a few percent of $R \ln 2$ [5], indicating therefore that only a minor part of the total number of spins contribute to the spin-liquid phase. Interestingly enough, the shape of the transition at 6 K (Fig. 4.26 (a)), resembles the shape of the anomaly in the thermal expansion coefficient associated

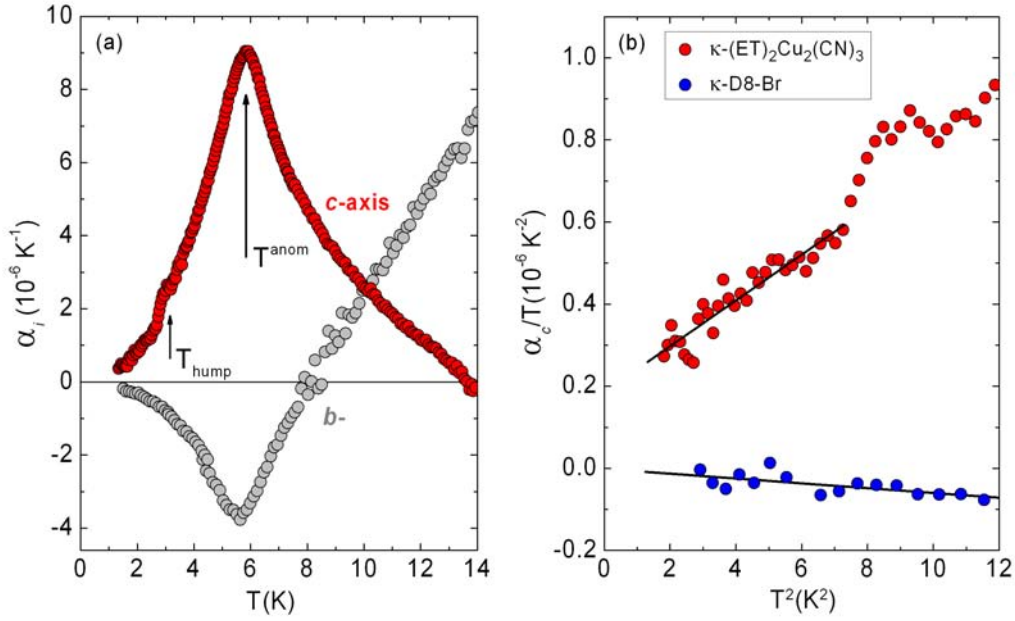

Figure 4.26: (a) Blow-up of the low-temperature expansivity data along the in-plane *c*- (crystal #1) and *b*-axis (crystal #2) of κ-(ET)$_2$Cu$_2$(CN)$_3$ on expanded scales, showing the sharpness of the transition at $T^{anom} \simeq 6$ K and a hump in α_c at $T_{hump} \simeq 2.8$ K along the *c*-axis. (b) α_c/T versus T^2 plot for κ-(ET)$_2$Cu$_2$(CN)$_3$ and fully deuterated κ-(ET)$_2$Cu[N(CN)$_2$]Br (data along the in-plane *a*-axis). Solid lines correspond to linear fittings.

with the Spin-Peierls transition for the quasi-1D organic conductors (TMTTF)$_2$X (X = PF_6 and AsF_6), see inset of Figs. 5.10 and 5.11 in Section 5.4. Hence, the sharp lattice distortion at $T^{anom} \simeq 6$ K seems to be associated with a real phase transition and not with a crossover, as proposed in Ref. [5]. During the preparation of this thesis, preliminary thermal expansion measurements along the second in-plane *b*-axis[25] revealed striking anisotropic in-plane lattice effects. Interestingly enough, along the in-plane *b*-axis (see Fig. 4.26) a negative anomaly is observed at $T^{anom} \simeq 6$ K, indicating that below T^{anom} a lattice expansion (shrinkage) along the *c*-axis (*b*-axis) occurs. The observed distinct in-plane anisotropy implies that the hopping integral terms t and t' are strongly affected. In Fig. 4.26 (b), the thermal expansion coefficient of κ-(ET)$_2$Cu$_2$(CN)$_3$ is shown in a α_c/T versus T^2 plot together with data for a fully deuterated κ-(ET)$_2$Cu[N(CN)$_2$]Br crystal (crystal #1). As can be seen from the linear fits (solid lines in Fig. 4.26 (b)), while the in-T linear term vanishes as $T \to 0$ for the Mott insulator κ-D8-Br salt, consistent with vanishing Sommerfeld coefficient, α_c/T remains finite ($\alpha_c/T = \gamma^{\alpha_c} = (0.19 \pm 0.02) \cdot 10^{-6}\,\mathrm{K}^{-2}$) for the κ-(ET)$_2Cu_2(CN)_3$ salt. Similar fits along the second in-plane *b*-axis results in $\gamma^{\alpha_b} = (-0.082 \pm 0.006) \cdot 10^{-6}\,\mathrm{K}^{-2}$, a value which corresponds roughly to half of γ^{α_c}. Since corresponding data along the out-of-plane *a*-axis are missing[26], the difference $\gamma^{\alpha_c} + \gamma^{\alpha_b}$

[25]Thermal expansion measurement along the in-plane *b*-axis (gray data in Fig. 4.26 (a)) was carried out by Rudra Sekhar Manna - Physics Institute - Group of Prof. Dr. Michael Lang - Goethe University - Frankfurt (M) - Germany, under supervision of the author of this thesis.

[26]Measurements along the out-of-plane *a*-axis in the temperature range 4.2 K - 200 K have been carried

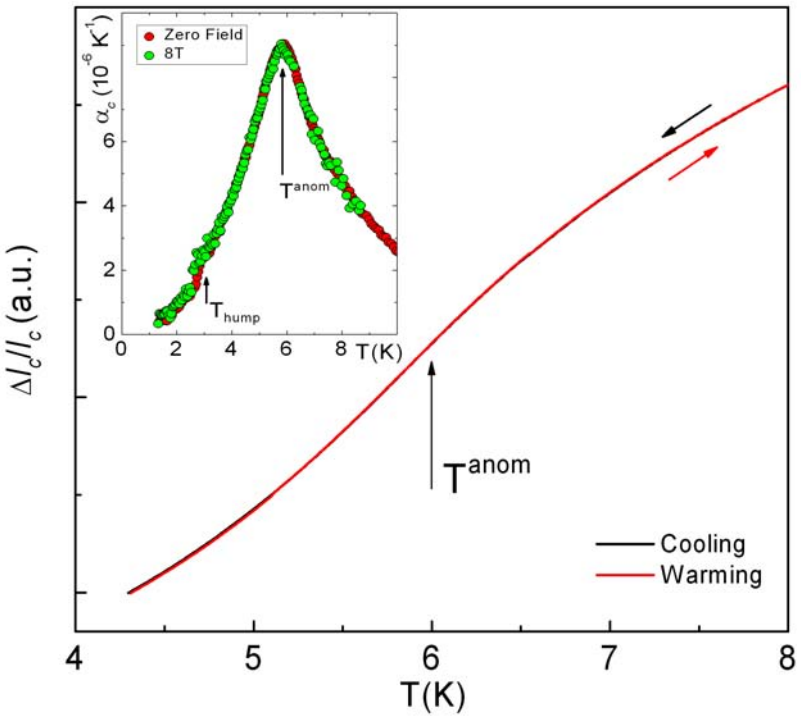

Figure 4.27: Main panel: Relative length changes (in arbitrary units) for κ-(ET)$_2$Cu$_2$(CN)$_3$ along the in-plane *c*-axis measured at very low sweeping rates of $\pm$1.5 K/h, showing the absence of hysteretic behavior. Inset: Thermal expansion data under zero magnetic field and 8 T. Such measurements were taken on warming, while the magnetic field was applied at 1.3 K.

= $0.11 \cdot 10^{-6}$ K^{-2} will be used to make a crude estimate[27] of the "spin-fluctuation" (sf) Grüneisen parameter Γ_{sf} for this salt, assuming that below 1.3 K (lowest temperature accessible in the present experiments) α_c/T behaves linearly as $T \rightarrow 0$. Using a Sommerfeld coefficient of γ = (20 mJmol^{-1}K^{-2}), obtained from specific heat measurements on a crystal from the same batch as the one studied here [28], a bulk modulus $B = 1/\kappa_T$ = 122 kbar [117] taken from κ-(ET)$_2$Cu(NCS)$_2$, and using the molar volume V_{mol} = $(2.6 \cdot 10^{-4})$ m^3/mol, results in $\Gamma_{sf} \simeq 15$. This value is roughly one order of magnitude higher than those found for other organic conductors. For example, for the κ-(ET)$_2$Cu(NCS)$_2$ and β''-(ET)$_2$SF$_5$CH$_2$CF$_2$SO$_3$ salts, $\Gamma_{eff} \simeq 3.5$ and 1 [11], respectively. The value obtained here ($\Gamma_{sf} \simeq 15$) is, however, not so far from typical values obtained for heavy fermion compounds[29]. As the Grüneisen parameter is a measure of the pressure dependence of the characteristic temperature, the large value of $\Gamma_{sf} \simeq 15$ estimated here for

out in the frame of the present work. Nevertheless, it was revealed that drift effects were involved in such experiments. Given the tiny thickness ($\sim$60 μm) of the crystal along this direction, the measured length changes (capacitance changes) were in the limit of the resolution of the capacitance bridge employed in the present experiments.

[27] The analysis made here is, obviously, no longer valid if a vanishing β/T is observed as $T \rightarrow 0$.

[28] Specific heat measurements on κ-(ET)$_2$Cu$_2$(CN)$_3$ down to 1.8 K have been performed by Dr. Andreas Brühl, Group of Prof. Dr. Michael Lang, Physics Institute - Goethe University - Frankfurt (M) - Germany. The Sommerfeld coefficient obtained from the latter experiments is somehow higher than γ = (15 mJmol^{-1}K^{-2}), obtained by S. Yamashita *et al.* [5].

[29] For example, Γ = 57 is obtained for the heavy-fermion compound CeCu$_6$ [144].

the κ-(ET)$_2$Cu$_2$(CN)$_3$ salt indicates that the characteristic energy which determines the ground state is very sensitive to external pressure. It remains to be seen whether the latter is in fact a spin-liquid state. In this sense, thermal expansion measurements along the out-of-plane *a*-axis, as well as measurements at very low temperatures along the *a*-, *b*- and *c*-axes are required in order to achieve a better understanding of the physics of this exciting material. Such experiments will reveal, for example, whether below 1.3 K α/T behaves linearly and remains finite as $T \to 0$, as observed in specific heat measurements [5] or if α/T decreases exponentially[30] as $T \to 0$. If the latter scenario is confirmed, perhaps the idea of a spin-liquid phase in κ-(ET)$_2$Cu$_2$(CN)$_3$ has to be reviewed.

[30] During the preparation of this work, it was reported [187] that the thermal conductivity of κ-(ET)$_2$Cu$_2$(CN)$_3$ is described by an activated behavior with a gap $\Delta_\kappa \simeq 0.46$ K. The latter results are at odds with the specific measurements performed by S. Yamashita *et al.* [5] (discussed in Section 4.5.2) and, if confirmed, a new window is opened to the understanding of the ground state of this system.

Chapter 5

The Quasi-1D Fabre-Bechgaard Salts

This chapter is dedicated to the study of the quasi-1D $(TMTCF)_2X$ charge-transfer salt family. In the materials of this family, the interplay between strong electron-electron and electron-phonon interactions gives rise to a variety of ground states. By applying pressure or exchanging the anion X, the above-mentioned interactions together with the bandwidth are altered and the system can, for example, be tuned from the non-magnetic Spin-Peierls state to superconductivity. The charge-ordering (CO) phase transition, already introduced in Section 2.6, is one of the main subjects of the present chapter. The chapter is organized in the following way: firstly the main features of the crystal structure of the $(TMTCF)_2X$ family are recalled. This is followed by a discussion of the main literature results. Thermal expansion measurements obtained in the frame of the present work are then presented and discussed in detail. This chapter presents two highlights: i) observation of lattice effects associated with the CO (*structureless*) transition in the $(TMTTF)_2X$ family with X = PF_6, AsF_6 and SbF_6; ii) evidence for a second-order transition suggestive of neutral-ionic (NI) transition in the same family due to the charge disproportionation.

5.1 Crystal Structure of the Fabre-Bechgaard Salts

The building block of the Fabre-Bechgaard family of organic conductors is the (TMTCF) molecule (shown in Fig. 5.1); here *C* stands for the chalcogenes S or Se atoms. Irrespective of the counter ion, all $(TMTCF)_2X$ salts crystallize in the triclinic structure $P\bar{1}$ with two donor molecules and one anion in the unit cell, cf. Fig. 5.2.

As can be seen from Figs. 5.2 and 5.3, the planar (TMTCF) molecules are arranged in a zig-zag configuration forming stacks along the *a*-axis, where the highest conductivity in these materials is observed. The stacks form layers in the *a* - *b* plane, which are separated by the anions along the *c*-axis, so that the shortest separation between the sulfur (for the TMTTF family) or selenium (for the TMTSF) atom is along the crystallographic *b*-axis.

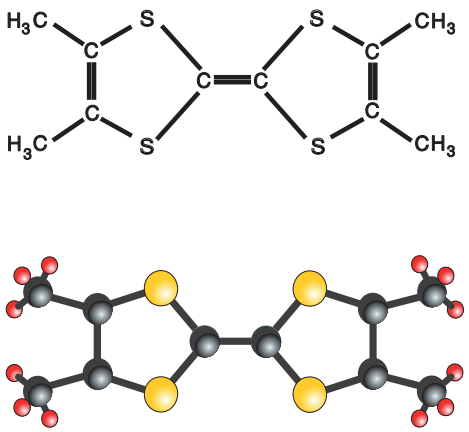

Figure 5.1: The (TMTCF) molecule, which is the basic entity that furnishes the Fabre-Bechgaard charge-transfer salts. *C* stands for S or Se atoms.

The methyl groups of the donor molecules TMTCF delimit cavities, in which the anions are lodged. The anions are classified according to their symmetry. For example, X = Br (spherical); PF_6, AsF_6 and SbF_6 (octahedral) are centrosymmetrical anions, while BF_4, ReO_4 (tetrahedral) and SCN (linear) are non-centrosymmetrical. As will be discussed in Section 5.3, the counter ions are not only responsible for making the charge balance of the $(TMTCF)_2^+$ donor molecule, but they also influence dramatically the electronic properties of the present materials. In the TMTSF salts, the interstack interaction is stronger than in the TMTTF salts. This is because the shortest Se-Se distance along the *b*-axis in the TMTSF family is less than twice the van der Waals' radii of the Se atoms, whereas in the TMTTF family the shortest S-S distance along the *b*-axis is more than twice the van der Waals' radii of the sulfur atoms. For this reason TMTTF based salts are more 1D than the TMTSF based salts. The hopping terms are roughly given by $t_a : t_b : t_c = 250 : 10 : 1$, cf. [145] and references therein. As the crystal structure is triclinic, thermal expansion measurements were carried out along three orthogonal axes, namely along the *a*-, *b'*- and c^* axes. The *a*-axis is along the stacks, the *b'*-axis is perpendicular to the *a*-axis in the *a*-*b* plane and c^*-axis is perpendicular to the *a*-*b* (*a*-*b'*) plane[1]. An important aspect in the structure of these materials is that the stacks are not equally spaced. There are two varying distances between consecutive molecules in the same stack, as indicated by d_1 and d_2 in Fig. 5.2, with $d_1 > d_2$. This feature gives rise to the formation of dimers of TMTCF molecules along the stacks. Dimerization[2] plays a very important role in the band filling and consequently in the electronic properties of these salts. Without taking into account dimerization effects, the band is quarter-filled in terms of holes, while an effective half-filled band has to be considered if dimerization is relatively strong. Upon cooling, dimerization is increased and the consequence of this is that, for $(TMTTF)_2X$ with X = PF_6 and AsF_6, a crossover to a Mott localized state, to be referred to as localiza-

[1]The crystals of the salts $(TMTTF)_2X$ (X = PF_6, AsF_6 and SbF_6) have the following shape: the long crystal axis is parallel to the *a*-axis, the intermediate axis parallel to the *b'*-axis and the short one parallel to the c^*-axis. This was the criterium adopted to align the crystals.

[2]Dimerization is usually defined as $2(d_1 - d_2)/a$, with a being the average distances between TMT*C*F molecules along the stacks, cf. Fig. 5.2. Dimerization effects are more pronounced in the TMTTF family and enhanced as the temperature is decreased [146].

tion (loc) in Section 5.3, takes place[3]. It is worthy of note that without taking into account the dimerization, the lattice periodicity π/a along the stacks in reciprocal space corresponds to the $4k_F$ wave-vector of the correlated electron gas in 1D. This new periodicity is related to the charge-ordering phenomena in the TMTTF family. The dimensions of the unit cell of the salts $(TMTTF)_2X$ (X = PF_6, AsF_6 and SbF_6) investigated here are listed in Table 5.1.

X	**PF_6**	**AsF_6**	**SbF_6**
a(Å)	7.146	7.178	7.195
b(Å)	7.583	7.610	7.622
c(Å)	13.218	13.317	13.45
α (^{0})	82.69	82.03	81.19
β (^{0})	84.87	95.75	96.65
γ (^{0})	72.42	107.11	106.19
V(Å^3)	676	598.2	643.3
d_1 (Å)	3.54	3.52	-
d_2 (Å)	3.64	3.62	-

Table 5.1: Lattice parameters of the $(TMTTF)_2X$ salts at room temperature for X = PF_6 [147], AsF_6 [148] and SbF_6 [149, 150].

5.2 Sample Preparation

The samples studied in this work, synthesized by the standard constant-current (low current density) electrochemical method, were provided by the group of Prof. Dr. J.-P. Pouget[4]. The list of the $(TMTTF)_2X$ salts investigated via thermal expansion is presented in Table 5.2. The crystals are needle-shaped with dimensions of about $10 \times 1 \times 0.5\,mm^3$. For measurements along the *a*-axis, due to the inherently large expansivity of the present materials, the sample was cut into pieces at lengths of about 1 mm. The data for the X = PF_6 salt discussed here refer to crystal #1. In order to check for reproducibility of the data, several runs were performed and, in particular, along the c^*-axis a second crystal (crystal #2) from the same batch was measured. For the X = AsF_6 salt, crystals #2 and #1 from the same batch were measured along the b'- and c^*-axes, respectively. For the latter salt *a*-axis data are missing because the crystals spontaneously cleaved as soon as a small force was exerted by the dilatometer. This seems to be due to the highly 1D character of this salt.

Anion X	**Crystal Number**	**Measured Direction**	**Batch**
PF_6	1	a, b', c^*	EII 93(2)
PF_6	2	c^*	EII 93(2)
AsF_6	1	c^*	EII 95
AsF_6	2	b'	EII 95
SbF_6	1	c^*	EII 131

Table 5.2: Samples of the quasi-1D organic conductor $(TMTTF)_2X$ on which thermal expansion measurements were carried out.

[3] In contrast with the continuous transition into the Mott localized state observed for the $(TMTTF)_2X$ salts with X = PF_6 and AsF_6, in Section 5.4, evidence for a first-order MI transition in the $(TMTTF)_2SbF_6$ salt will be provided.

[4] Laboratoire de Physique des Solides, Université Paris Sud, CNRS UMR 8502, Orsay, France.

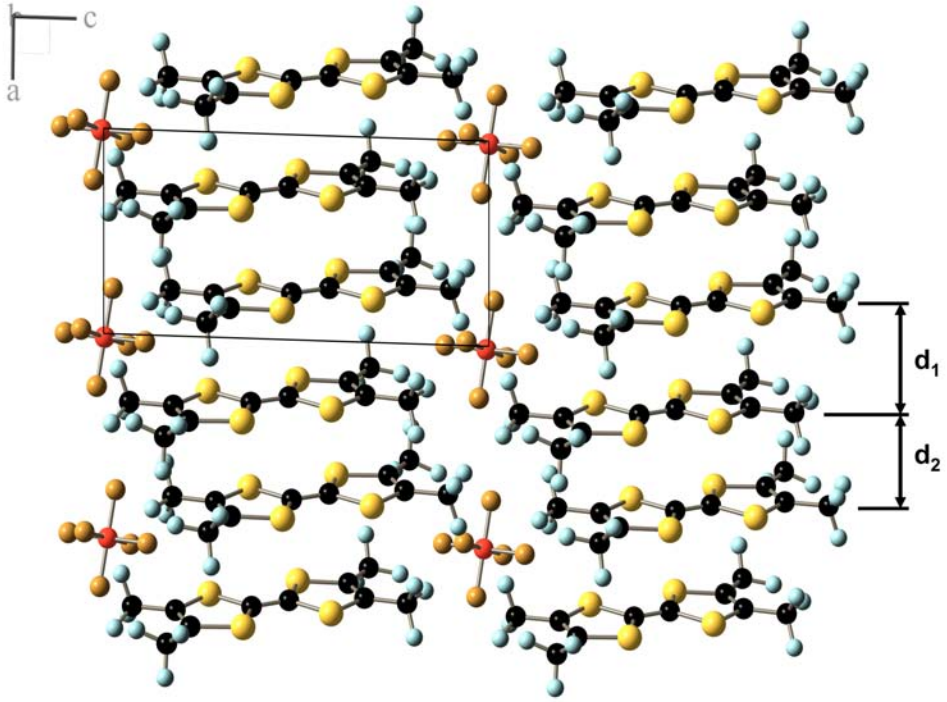

Figure 5.2: *a-c* plane projection of the crystallographic structure of the $(TMTTF)_2X$ charge-transfer salts. d_1 and d_2 are the interdimer and the intradimer spacing, respectively, being $d_1 > d_2$. The unit cell outline (black) is shown.

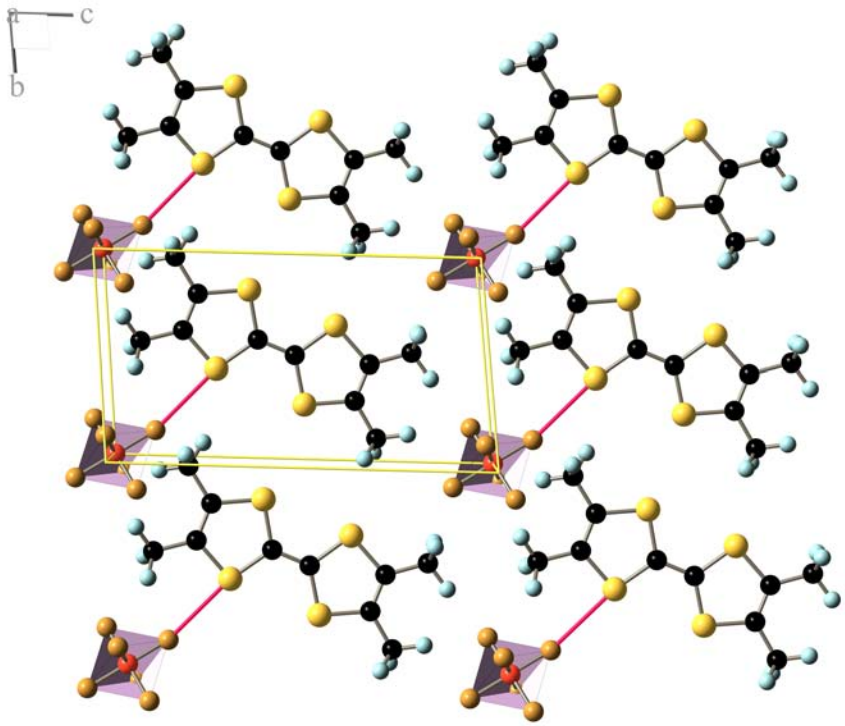

Figure 5.3: *b-c* plane view of the structure of $(TMTTF)_2X$ charge-transfer salts. The anion (X = PF_6, AsF_6 or SbF_6) is shown in an octahedron representation. Red lines indicate the shortest distance between the F and S atoms. The unit cell outline (yellow lines) is shown.

5.3 $(TMTTF)_2X$: State of the Art

The origin of the organic superconductors era can be traced back to the observation of superconductivity in $(TMTSF)_2PF_6$ by D. Jérome *et al.* [151] in the early 80s. Since then, charge-transfer salts of the $(TMTCF)_2X$ family, whose generalized P - T phase diagram is shown in Fig. 5.4, have been intensively studied and revealed to be ideal model-systems for studying electronic correlation effects in 1D. Here, the focus of the discussion will be on the properties of $(TMTTF)_2X$ family. As discussed in Section 2.4, quasi-1D conductors are inherently more susceptive to certain electronic instabilities than 2- or 3-D conductors. Due to the instability of the electron gas in 1D, together with the interplay of electron-electron and electron-phonon interactions, the phase diagram of such substances covers a wide variety of ground states.

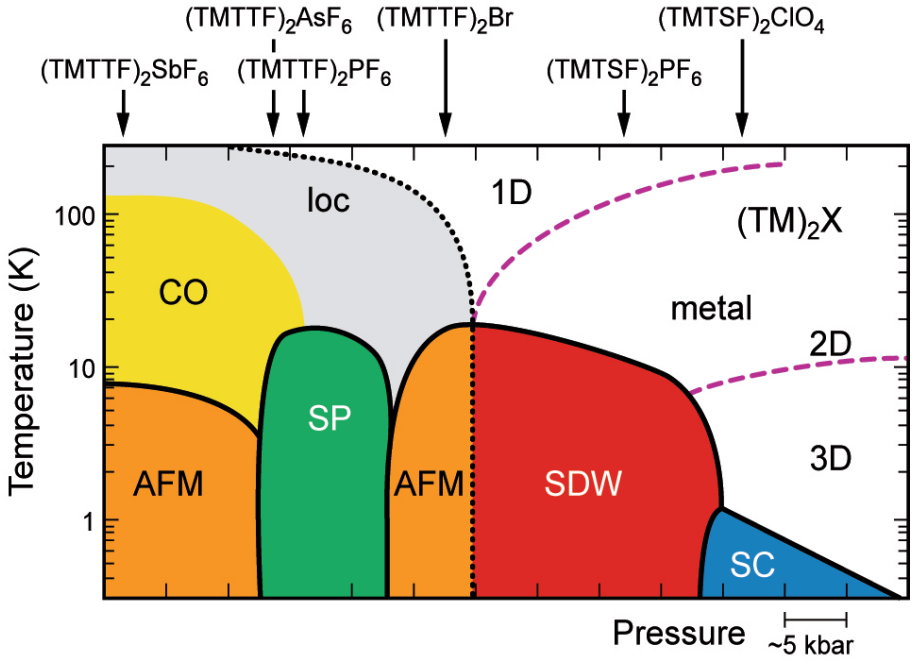

Figure 5.4: Generalized P - T phase diagram of the Fabre-Bechgaard charge-transfer salts. The position of the different compounds under ambient pressure is indicated by arrows. The various phases are Charge Localization (loc), Charge-Ordering (CO), Spin-Peierls (SP), Antiferromagnetic (AFM), Spin-Density Wave (SDW), Superconductivity (SC). Dimensional crossover passing through 1- to 2- or even 3D is indicated by the dashed lines. Picture taken from Ref. [46], cf. the generic phase diagram proposed by D. Jérome [77]. For details on the pressure dependence of T_{CO} for the X = SbF_6 and AsF_6 salts, see Fig. 5.8.

As Fig.5.4 highlights, the ground states can be tuned by anion substitution, exchange of the chalcogen atom of the donor molecule (C = Se or S) and/or external pressure application. In fact, pressure application increases the inter-stack interactions (t_b and t_c) and, as a consequence the dimensionality. As mentioned in Section 5.1, the $(TMTTF)_2X$ family, located on the left side of the phase diagram, is more 1D than its selenium analogous $(TMTSF)_2X$, located on the right side of the phase diagram. The phase diagram shown in Fig. 5.4 suggests that the members of the TMTTF family can be tuned to the TMTSF family by applying pressure. For example, by cooling the $(TMTTF)_2PF_6$ salt under ambient pressure, a smooth MI transition at $T_\rho \simeq 240\,\mathrm{K}$ (see curve 3 in Fig. 5.5) is observed. Upon further cooling, a CO phase transition coinciding with the onset of ferroelectricity takes place at $T_{CO} \simeq 65\,\mathrm{K}$. Cooling down to lower temperatures, a lattice

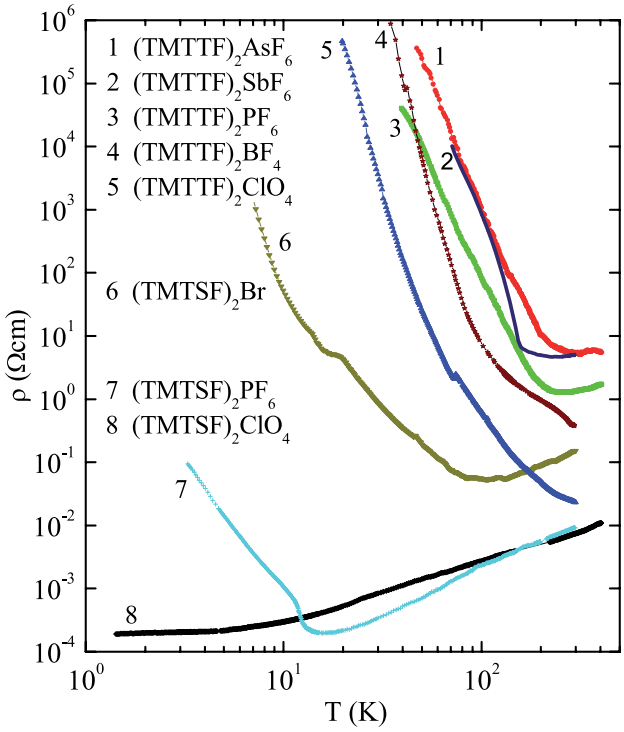

Figure 5.5: Resistivity versus temperature for several $(TMTCF)_2X$ salts. Upon cooling, a continuously charge localization, marked by a broad minimum at T_ρ = 200 - 250 K, is observed for the $(TMTTF)_2AsF_6$ (curve 1) and $(TMTTF)_2PF_6$ (curve 3) salts before the onset of the charge-ordered phase. For the $(TMTTF)_2SbF_6$ salt (curve 2), a CO transition accompanied by a MI transition takes place at $T_{CO,MI} \simeq 150$ K. The $(TMTSF)_2PF_6$ salt (curve 8) remains metallic down to T_c = 1.2 K, where the resistance vanishes and superconductivity takes place. Picture taken from Ref. [46].

distorted SP state at $T_{SP} \simeq 18$ K occurs. On applying pressure, the CO phase and the SP state are suppressed. The latter gives way to an antiferromagnetic ordering, similar to the one found in $(TMTTF)_2Br$ salt under ambient pressure. Applying further pressure ($\sim$ 15 kbar), the Mott localized (loc) state is then suppressed and the salt becomes metallic. At low T, a SDW phase transition takes place. Under a pressure of 52 - 54 kbar the SDW is then removed and superconductivity occurs at T = 1.4 - 1.8 K [152], closing the sequence of ground states in the phase diagram. As can be seen from Fig. 5.4, the $(TMTSF)_2ClO_4$ salt is the only ambient pressure superconductor. Interestingly enough, for some non-centrosymmetrical anions, another phase transition called anion-ordering (AO) transition, which is a first-order phase transition, not shown in the phase diagram, can take place. At room temperature, the anion cavities delimited by the methyl groups of the TMTCF molecule are disordered. Upon cooling, the change of the spacing between TMTCF molecules is altered, implying thus a change of the contact between the anion cavity and its vicinity. Due to this the non-centrosymmetrical (tetrahedral) anions, such as ClO_4, ReO_4 and (linear) SCN, have to choose one of the two possible orientations in the cavity. A double potential barrier model[5], originated from the anions surrounding, was proposed by Pouget *et al*. to describe this transition [146]. Nevertheless, one of the most exciting results of past years in the $(TMTTF)_2X$ family was the observation of a CO phase transition at T_{CO} coinciding with the onset of a ferroelectric (FE) transition

[5]A similar model to treat the orientational degrees of freedom of the ethylene end-groups of the ET molecules in the quasi-2D organic κ-$(ET)_2X$ charge-transfer salt family was proposed by J. Müller [62].

for the X = PF_6 ($T_{CO} \simeq 65$ K [6]), AsF_6 ($T_{CO} \simeq 105$ K [6]) and SbF_6 ($T_{CO} \simeq 154$ K [153])[6] salts. In fact, some indications for the existence of the latter transition in the $(TMTTF)_2X$ family were observed more than 20 years ago. Resistivity measurements on the X = SbF_6 salt [150][7] revealed a sharp MI insulator transition at $T = 154$ K, coinciding with a dramatic change in the thermopower [156] and peak divergence in the real part of the dielectric constant [157]. The absence of signatures in magnetic susceptibility [156] leads to the belief that only charge degrees of freedom are involved in this transition. Until now, no evidence of structural changes [150] associated with this transition has been reported in the literature and due to this it has been labelled *structureless* transition. However, it was only in 2000 that a new piece of the puzzle was found, when NMR measurements performed by Chow *et al*. [6] revealed a splitting of the spectral line below the *structureless* transition, cf. Fig. 5.6. This spectral splitting is brought about because above the transition temperature T_{CO}, all the TMTTF molecules are equivalent, while below T_{CO} charge-rich TMTTF molecules alternate with charge-poor molecules (see inset of Fig. 5.6), giving rise to two inequivalent hyperfine couplings and a doubling of the spectral lines[8]. Hence, based on this observation, Chow *et al.* deduced that the *structureless* is associated with a CO phase transition.

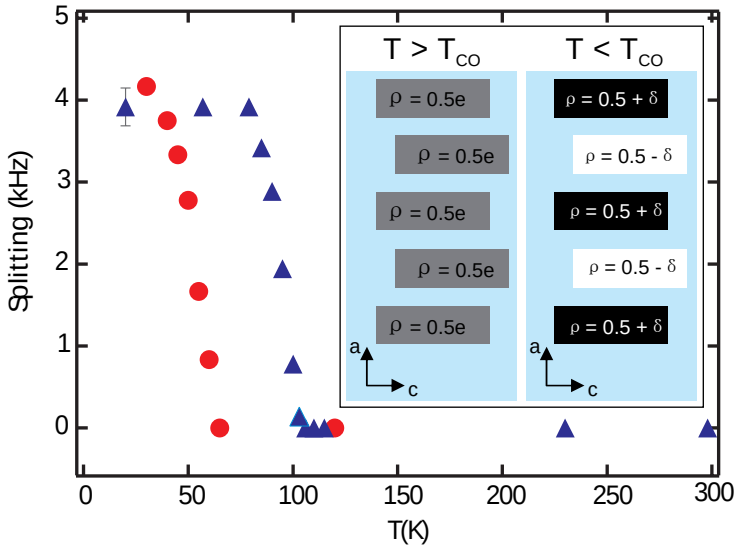

Figure 5.6: Spectral (^{13}C NMR line) splitting versus temperature due to two inequivalent donor molecules with unequal electron densities in $(TMTTF)_2X$ charge-transfer salts, with X = PF_6 (red curve) and AsF_6 (blue curve). Picture taken from Ref. [6]. Inset shows that above T_{CO} the charge ($\rho = 0.5e$) is equally distributed along the stacks. Gray rectangles represent equally charged TMTTF molecules. Below T_{CO} an alternated charge pattern $\pm\delta$ is found. Black and white rectangles represent, charge rich- and charge poor-sites.

Almost at the same time, dielectric measurements[9] [153,154] probed the FE character of the transition. This is due to the presence of electric dipoles generated by charge disproportionation along the stacks. Indeed, the absence of structural effects accompanying

[6] In fact, the CO transition was later also observed in the X = Br ($T_{CO} \simeq 28$ K), BF_4 ($T_{CO} \simeq 28$ K) and ReO_4 ($T_{CO} \simeq 227.5$ K) salts [155].

[7] In Ref. [150] the existence of the *structureless* transition in the X = PF_6 and AsF_6 salts was also mentioned.

[8] The spectral splitting associated with the CO transition observed by Chow *et al.* was interpreted as the order parameter of the transition.

[9] In fact, the first observation of divergence of the dielectric constant at the *structureless* transition was reported in Ref. [157].

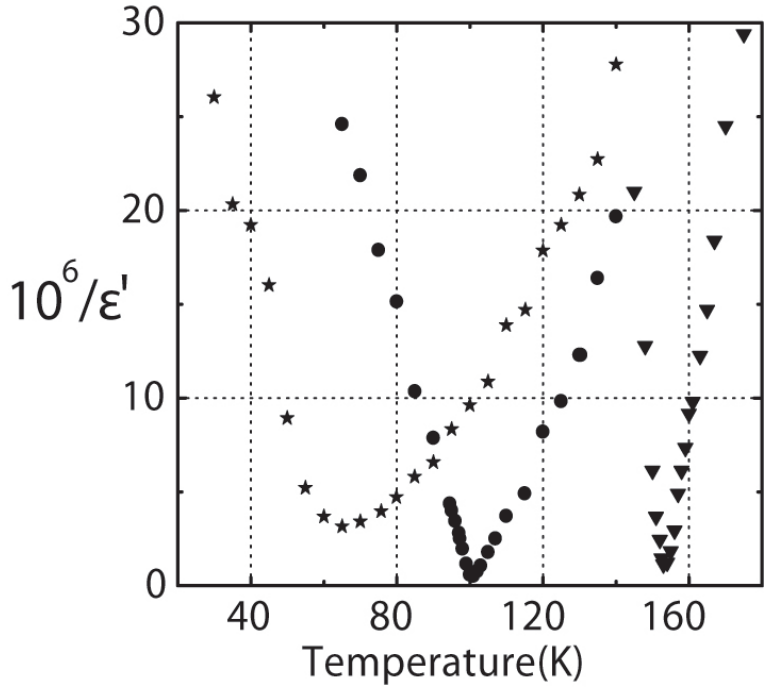

Figure 5.7: Inverse of the real part of the dielectric constant ϵ' of the $(TMTTF)_2X$ charge-transfer salts, with X = PF_6 (stars), AsF_6 (circles) and SbF_6 (triangles down), measured at 100 Hz. Picture taken from Ref. [153].

the CO transition is particularly puzzling as atomic displacements, breaking the inversion symmetry, are prerequisite for ferroelectricity to occur in these materials. According to the authors of Ref. [153], the FE phase is stabilized by subtle anion displacements, resulting in a 3D FE behavior. However, no such anion displacements have been reported until now in the literature. As Fig. 5.7 demonstrates, the transition is described nicely by a Curie-like behavior of the real part of the dielectric constant, i.e. ϵ' = A / | T - T_{CO} |, consistent with a second-order phase transition with a mean-field character, indicating that fluctuations are suppressed by the 3D long range Coulomb interactions [153]. Nevertheless, a careful analysis of the dielectric constant data reveal precursor effects already at $T \simeq 200$ K for the X = PF_6 salt [154]. Interestingly enough, below $T \simeq 200$ K the spin susceptibility decreases monotonically [170]. Hence, the observation of pronounced signatures in the dielectric constant, but absence of magnetic signatures at T_{CO}, offer strong evidence for spin-charge separation in these materials.

The effect of pressure on the CO transition was studied in detail via NMR measurements [158, 159], cf. Fig. 5.8. It was observed that by applying pressure, T_{CO} decreases dramatically. For example, for the X = AsF_6 salt (data in blue in Fig. 5.8), a pressure of roughly 1.5 kbar is enough to suppress the CO phase. The authors interpret this feature as the result of the increase of the bandwidth relative to the strength of the inter-site Coulomb repulsion within the stacks, which is recognized as the driving force for the CO transition to occur. As can be seen from Fig. 5.8, under low pressures ($P \simeq 1.5$ kbar) both SP and CO phases coexist. For the X = SbF_6 salt (data in red in Fig. 5.8), a pressure of roughly 5 kbar is necessary to suppress the CO phase. At low temperatures, pressure application destroys the AF ordering giving rise to a singlet ground state. This is not a surprise, as the the SbF_6^- counter ion is much larger than PF_6^- or AsF_6^-, implying thus a more compact packing in the b - c plane and consequently stronger interactions between counter ion and stack. These results demonstrate the inadequacy of the idea of a

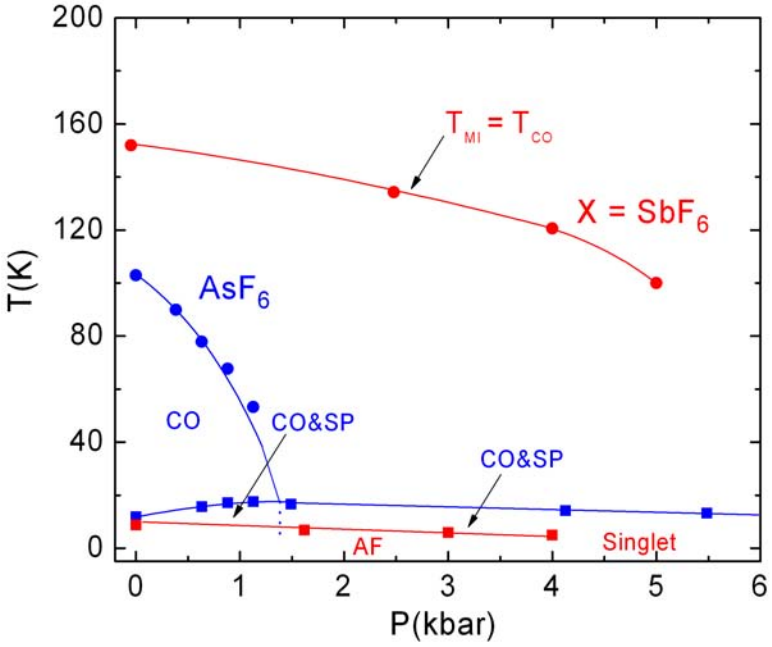

Figure 5.8: Pressure versus temperature phase diagram for $(TMTTF)_2X$, X = AsF_6 (blue) (data taken from Ref. [158]) and SbF_6 (red) (data taken from Ref. [159]) obtained from NMR measurements under pressure. Lines are guides to the eyes for both set of data. X = SbF_6: $T_{MI} = T_{CO}$ indicates that the MI transition temperature T_{MI} coincides with the charge-ordering transition temperature T_{CO}. T_{CO} decreases as pressure is increased. Above 5 kbar, no signature for the CO is observed. In the same way, above 4 kbar the AF ordering is suppressed giving way to a singlet ground state. X = AsF_6: CO & SP indicate the coexistence of charge-ordered and Spin-Peierls phases. Dashed blue line separates the coexistence region. This data set shows that the idea of a generalized phase diagram for the $(TMTTF)_2X$ family is inappropriate.

universal phase diagram, at least on the left side of the phase diagram (Fig. 5.4).

Later Dumm *et al.* [161] studied the influence of charge disproportionation on the vibrational spectra of the X = PF_6 and AsF_6 salts via mid-infrared optical conductivity as a function of temperature with the light polarized along the stacks (*a*-axis) (Fig. 5.9). They found that the intermolecular $a_g(\nu_3)$ mode, which becomes infra-red active through electron-molecular-vibration, splits below T_{CO}. This feature is explained by the strong dependence of this vibronic mode on the degree of ionization of the TMTTF molecule [162]. In this study, the authors estimated a charge disproportionation ratio of 5 : 4 and 2 : 1 for X = PF_6 and AsF_6, respectively. A higher charge disproportionation ratio for the X = AsF_6 is linked with pronounced peak in the real part of the dielectric constant at T_{CO} (Fig. 5.7). Note that a rather broad phase transition is observed for the X = PF_6 salt. The reason for this discrepancy was not discussed by the authors of Ref. [153].

From the theoretical point of view, using the extended Hubbard model coupled to the lattice, Riera and Poiblanc [160] proposed that the CO is due to a cooperative effect between the inter-site Coulomb interaction V and the coupling of electronic stacks to the anions. In their model, small uniform displacements of the anions, which imply local changes of the on-site electronic energy, are necessary to stabilize the CO phase.

Concluding this section, it is useful to stress that according to the model proposed by Riera and Poiblanc [160], anion displacement plays a crucial role in the stabilization of

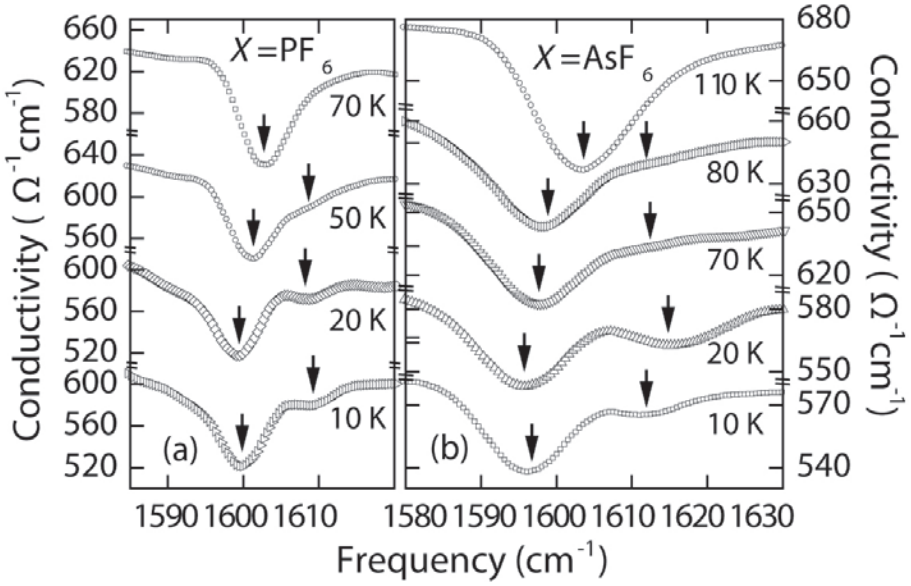

Figure 5.9: Mid-infrared conductivity for light polarized parallel to the stacks (*a*-axis) of $(TMTTF)_2X$ with (a) X = PF_6 and (b) X = AsF_6 at various temperatures. Below T_{CO} the electron-molecular vibronic mode $a_g(\nu_3)$ splits, as indicated by arrows, indicating the existence of two differently charged species of TMTTF molecules. Picture taken from Ref. [161].

the CO phase. However, the observation of such a feature is still lacking. The difficulty of detecting structural changes associated with the CO transition in the $(TMTTF)_2X$ family results from their triclinic symmetry implying that apart from inversion symmetry, no other symmetry element is broken at the CO transition. In order to solve this issue, systematic high-resolution thermal expansion experiments were carried out on the $(TMTTF)_2X$ family with X = PF_6, AsF_6 and SbF_6. These results comprise the main part of the present chapter and will be discussed in the next section.

5.4 Thermal Expansion Measurements on $(TMTTF)_2X$ salts

As discussed in the previous section, up to now no evidence of structural changes associated with the CO (*structureless*) transition has been reported in the literature. The focus of this section is the direct observation of such effects via high-resolution thermal expansion experiments. Figs. 5.10, 5.11 and 5.12 show the uniaxial expansivity for the X = PF_6, AsF_6 and SbF_6 salts, respectively. These results represent the first report of directional-dependent high-resolution thermal expansion experiments on the present materials. As can be seen from Figs. 5.10 and 5.11, the data disclose strong anisotropic lattice effects at both the Spin-Peierls transition (inset of Figs. 5.10 and 5.11) and the CO transition, with the strongest response along the c^*-axis, along which planes of TMTTF molecules alternate with planes of counter anions X. Interestingly, along the chain direction[10] (*a*-axis), almost no effects are observed. The anomalous behavior along the c^* direction, where the stacks are separated by counter anions, provides strong evidence that the counter anion plays a crucial role in the stabilization of the CO phase[11]. As

[10]Data along the *a*-axis for the X = AsF_6 salt are missing because the sample simply cleaved as soon as a small force was exerted by dilatometer. This seems to be related to the high 1D character of this salt.

[11]In fact, anion displacements accompanying the CO transition can be viewed as a direct consequence of the Earnshaw's theorem, which states that a classical system of point charges, under the interaction of

expected from the overall temperature dependence of the data, attempts to fit the data employing a Debye-like behavior along the three axes proved unsuccessful. Along the chain-axis up to $\sim$ 100 K (red solid line in Fig.5.10) a Debye fit work relatively well[12], with a Debye temperature Θ_D of 158 K. However, due to the anomalous lattice effects, as depicted in Figs. 5.10 and 5.11, along the *b'*- and *c**-axes the Debye model fails to describe the data. These findings are now discussed in more detail. For the X = PF_6 (Fig. 5.10) and X = AsF_6 (Fig. 5.11) salts, upon cooling, anomalous behavior is observed along the *c**-axis for $T > T_{CO}$. The data reveal a striking negative slope, $d\alpha_{c^*}(T)/dT < 0$, down to the CO transition temperature T_{CO}. Less pronounced effects are observed along the *a*- and *b'*-axes. The rapid reduction of α_{c^*} immediately below T_{CO} is indicative of a broadened step-like anomaly, i.e. a mean-field-like transition, with $\Delta\alpha_{c^*} \mid_{T_{CO}} = \alpha(T \rightarrow T_{CO}^-) - \alpha(T \rightarrow T_{CO}^+) < 0$. According to the Ehrenfest theorem (Eq. 2.26), the sign of the volumetric thermal expansion coefficient jump, i.e. $\Delta\beta = \Sigma_i \Delta\alpha_i$, defines the pressure dependence of the corresponding second-order phase transition. Hence, the negative jump anomaly in $\alpha_i(T)$ at T_{CO} is consistent with $dT_{CO}/dP < 0$, which agrees with NMR data under hydrostatic pressure [158]. Upon further cooling, a kink at $T_{int} \simeq (39 \pm 2)$ K and (65 ± 3) K for X = PF_6 and AsF_6, respectively, indicates a new phase transition, up until now not discussed in the literature. Possible scenarios for this feature will be discussed below. The SP transition takes place at $T_{SP} \simeq 18$ K for the X = PF_6 salt and 11 K for X = AsF_6. Again, more pronounced effects are observed along the *c**-axis. This means that the tetramerization of the TMTTF stacks is accompanied by striking lattice effects perpendicular to the chains, indicating therefore a shift of the TMTTF molecules along the *c**-axis. Since the TMTTF molecules form cavities where the anions are trapped, these SP distortions of the TMTTF sublattice will also cause shifts of the anions. Note that the anomalies at T_{CO} and T_{SP} differ markedly in their shapes. While kinks observed at T_{CO} are consistent with a mean-field transition, as discussed above, the anomalies at T_{SP} for both salts significantly deviate from such a behavior, indicating the presence of significant critical fluctuations, complying with Spin-Peierls fluctuations observed for both compounds by X-ray diffuse scattering studies [150, 163]. A negative contribution in α_b' for the X = AsF_6 salt indicates, according to the Ehrenfest theorem, a negative pressure dependence along the *b'*-axis. The shape of the anomalies at T_{CO} is unlike that of conventional FE materials like tri-glycine sulfate (TGS) [164] and $BaTiO_3$ [165], where sharp negative anomalies are observed at the transition temperature.

Below T_{CO}, however, the observed kink in $\alpha_i(T)$ at T_{int}, again more pronounced along the *c**-axis, indicates the existence of an additional phase transition at $T_{SP} < T_{int} < T_{CO}$. These features can be better visualized in Fig. 5.14, where the volumetric thermal expansion coefficient β, divided by T for $(TMTTF)_2PF_6$, is shown together with dielectric constant data extracted from the literature [155] for the same salt. Very sharp kinks in $\beta(T)/T$ are observed at T_{CO} and T_{int}. Note that the shape of the anomalies is very similar, indicating therefore that both phase transitions are likely to have the same origin. Interestingly enough, a small bump at T_{int} can also be observed in the real part of the dielectric constant $\epsilon'(T)$, a feature which has been overlooked so far. It is important to note that a small shift in the peak at T_{CO} as well as in the bump at T_{int} in the dielectric constant is likely due to the frequency dependence of ϵ' for this salt. For the $(TMTTF)_2PF_6$ salt, it has been found that with decreasing frequency, the maximum of ϵ' is enhanced and its position shifts to lower temperatures [154], while for the $(TMTTF)_2AsF_6$ and $(TMTTF)_2SbF_6$ salts the peak position remains practically unaffected, but the magnitude

Coulomb forces alone is unstable, since there is no minimum in the electrostatic potential.

[12] We observed that by changing the temperature range of the fits, Θ_D varies markedly. For example, a fitting up to 24 K along the *a*-axis results in Θ_D = 102 K.

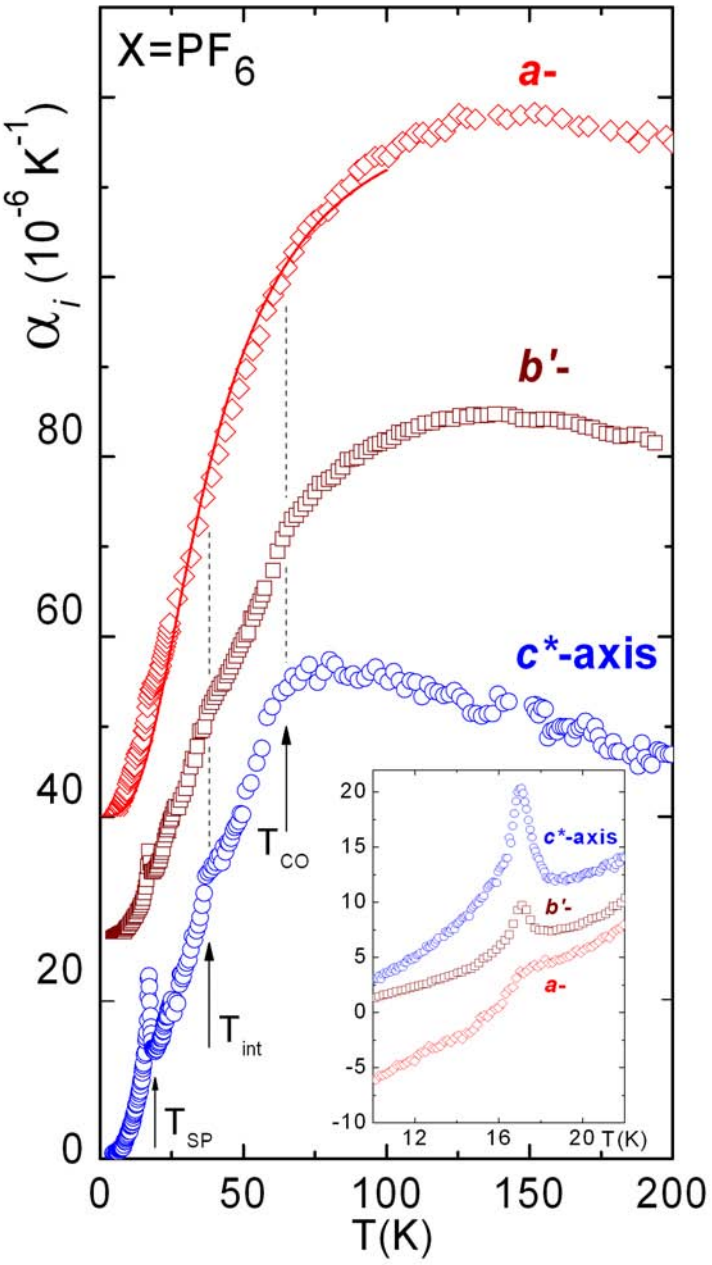

Figure 5.10: Uniaxial thermal expansion coefficient versus T along the *a*-, *b*′- and *c**-axis for the $(TMTTF)_2PF_6$ salt. Red line is a Debye fitting up to 100 K along the *a*-axis. Data are shifted for clarity. Inset: zoom of the low temperature data. Arrows indicate the charge-ordering (T_{CO}), the intermediary (T_{int}) and the Spin-Peierls (T_{SP}) transition temperatures.

of the anomaly decreases as the frequency is increased[13]. A hint to the physical process involved in the anomalies at T_{CO} and T_{int} is provided in the inset of Fig. 5.14, where α_{c^*}/T is plotted as a function of T/T_{CO} for the X = PF_6 and AsF_6 salts. A remarkable phenomenological result obtained from this plot is that the anomalies at T_{int} and T_{CO} for

[13]In fact, such frequency dependence in ϵ' for the $(TMTTF)_2PF_6$ salt is a typical signature of relaxor-type ferroelectric systems, see e.g. [166].

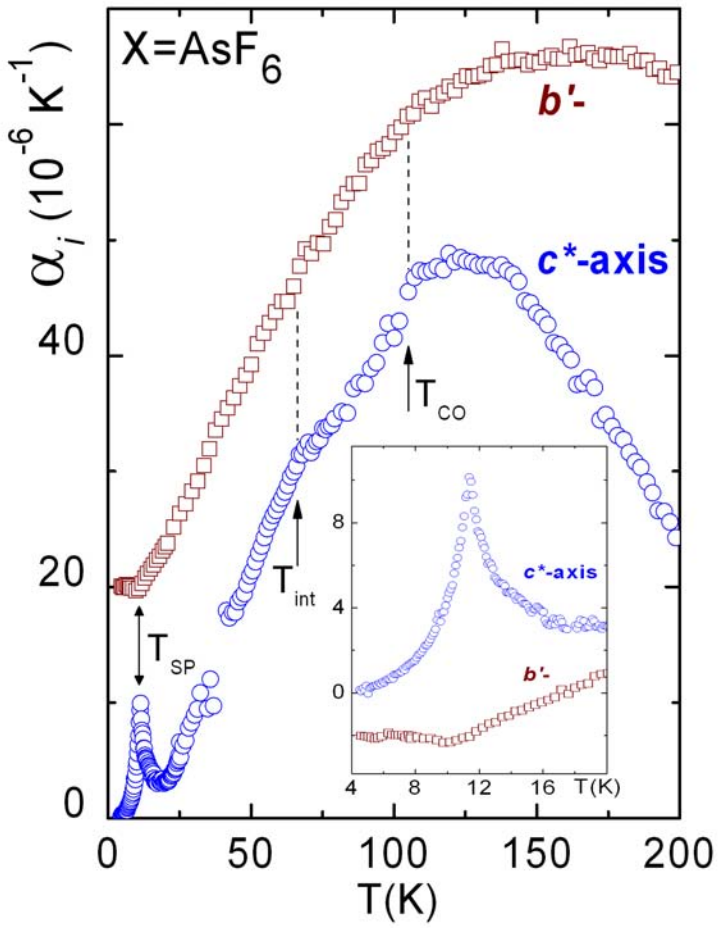

Figure 5.11: Uniaxial thermal expansion coefficient versus T along the b'- and c^*-axis for the $(TMTTF)_2AsF_6$ salt. Data are shifted for clarity. Inset: blow up of the low-temperature data. Arrows indicate the charge-ordering (T_{CO}), the intermediary (T_{int}) and the Spin-Peierls (T_{SP}) transition temperatures, respectively. Missing data in α_{c^*} in the T window 39 - 41 K is due to high noise in this temperature window.

both salts are linked by $T_{int} \simeq 0.6 \cdot T_{CO}$. Interestingly enough, dielectric measurements as a function of T on the mixed-stack charge-transfer salt (TTF-CA), which is recognized as the prototype system for studying the NI transition (cf. discussed in Section 2.7) revealed a striking behavior [167]. Upon cooling the system through the NI transition, two distinct peaks are observed in the real part of the dielectric constant. The authors assigned these features to the dynamics of the NI domain-pairs and ionic domains in the neutral lattice. Amazingly, the position of the peaks is linked by a factor of 0.6, i.e. the same factor that links T_{int} and T_{CO} in the $(TMTTF)_2X$ salts with X = PF_6, AsF_6, as discussed above. This observation indicates that a connection between both phenomena exists. The huge anomaly observed at $T_{CO,MI}$ = 154 K (Fig. 5.12) for the X = SbF_6 salt, coinciding nicely with the peak in ϵ', is quite distinct from the features observed in the X = PF_6, AsF_6 salts, since in X = SbF_6 the CO transition is accompanied by a MI transition. Interestingly, the anomaly at $T_{CO,MI}$ in X = SbF_6 resembles the shape of the anomaly observed at the Mott MI transition in κ-D8-Br (see Fig. 4.14 in Section 4.6), indicating therefore that for the X = SbF_6 salt, charge localization occurs not gradually like in the X = PF_6 and AsF_6 salts but

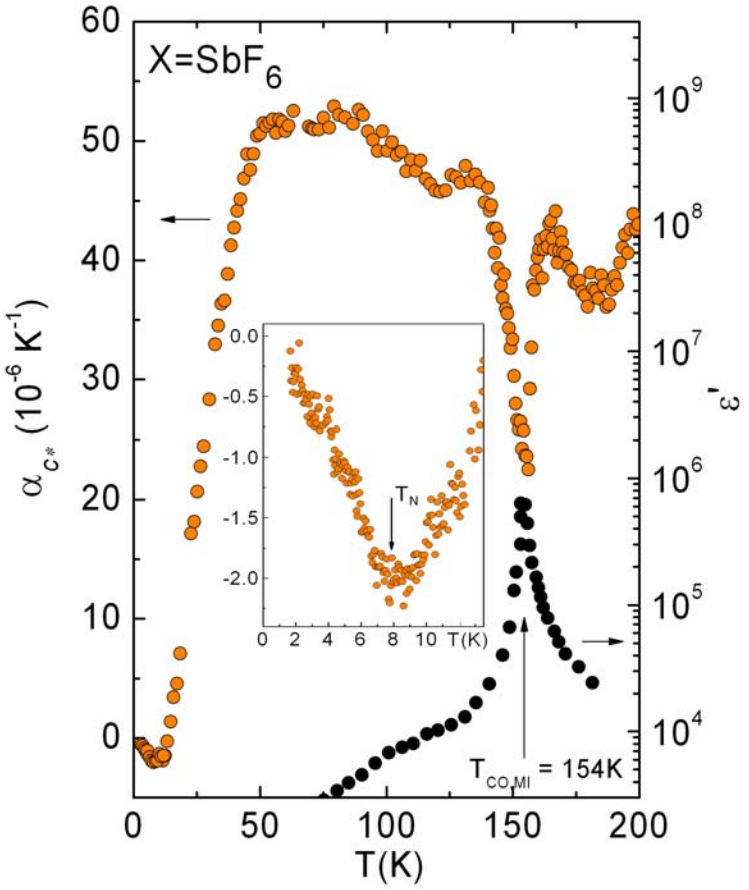

Figure 5.12: Left scale: uniaxial thermal expansion coefficient versus T along the c^*-axis for the $(TMTTF)_2SbF_6$ salt. Right scale: real part of the dielectric constant ϵ' (data taken from Ref. [155]) plotted on the same T scale as α_{c^*}. $T_{CO,MI}$ indicates the coexistence of CO and MI transitions. Inset shows details of the tiny anomaly in α_{c^*} due to the antiferromagnetic ordering at $T_N \simeq 8$ K.

abruptly. As can be seen from Fig. 5.13, an abrupt change of the c^* lattice parameter with a jump in the relative length change at $T_{CO,MI}$ = 154 K of about 3.3×10^{-4} is observed. This value is of the same order of magnitude than the relative length change jump along the polymeric anion chains associated with the Mott MI transition observed in κ-D8-Br (see Fig. 4.15). Based on the latter results, the MI transition for the $(TMTTF)_2SbF_6$ is likely to be first-order.

It is worth mentioning that a tiny crystal of the X = SbF_6 salt with thickness of about 0.1 mm was used for such measurements. Interestingly, despite this small thickness, which is even smaller than the Ga spheres used to sustain the sample in the cell, huge lattice effects show up at $T_{CO,MI}$ = 154 K. As can be seen from the inset of Fig. 5.12, a negative anomalous contribution in α_{c^*} shows up at T_N. Although very small, this negative contribution indicates that dT_N / $dP_{c^*} < 0$. NMR measurements on the X = SbF_6 under hydrostatic pressure revealed a negative pressure dependence of T_N [158] (see Fig. 5.8). Hence, the present results provide evidence that also for the X = SbF_6 the c^* lattice parameter is important for the pressure-induced changes of T_N.

Based on the findings discussed above for the X = PF_6 and AsF_6 salts, some natural questions arise: (i) What is the origin of the anomalous behavior in $\alpha_{c^*}(T)$ above T_{CO}?

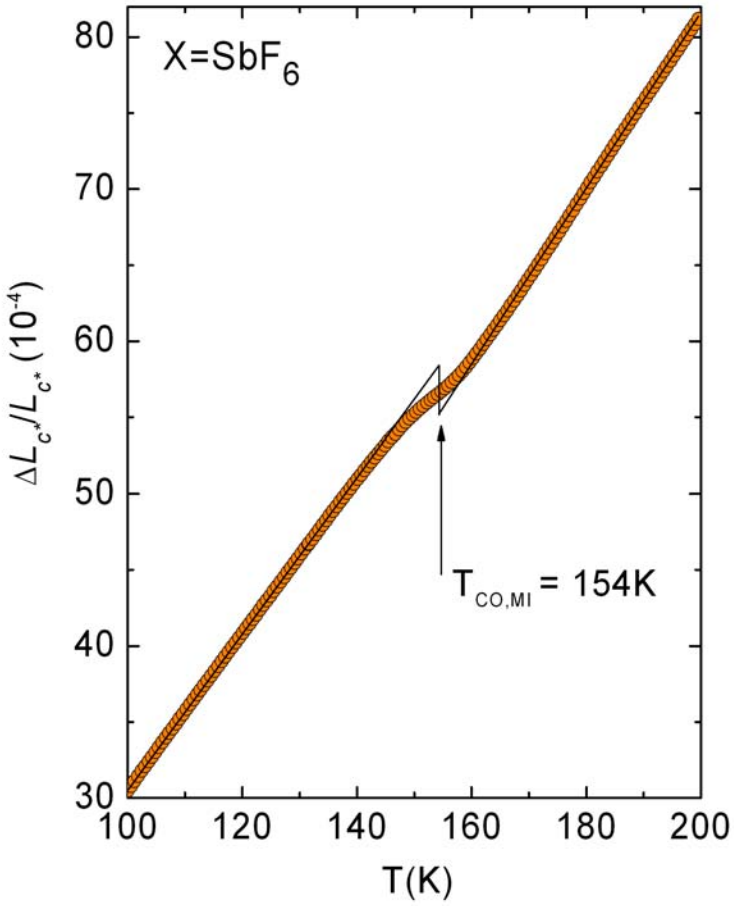

Figure 5.13: Relative length changes versus T along the c^*-axis for the $(TMTTF)_2SbF_6$ salt. Solid lines are used to indicate the change of the lattice parameter at $T_{CO,MI}$ = 154 K.

(ii) Why are such effects more pronounced in the salt with X = AsF_6 than X = PF_6? (iii) What is the origin of the kink at T_{int}? The answers for these questions are not straightforward and require special analysis.

Concerning question (i), the present thermal expansion data reveal that precursor effects, namely a negative contribution in α_{c^*}, start to play a role far above T_{CO}; a feature that can also be seen in dielectric measurements [155]. While the dielectric constant is described by mean-field-like behavior [153], where fluctuations are absent, the anomalous behavior in α_{c^*} indicates that a mechanism involving the anions starts to play a role at temperatures well above T_{CO}. However, the absence of critical behavior in $\alpha_i(T)$ is consistent with a mean-field-like character observed in dielectric constant measurements. One could try to associate this feature with the Mott localization, which in turn is related to the dimerization of the stacks upon cooling the system, but for the X = PF_6 and AsF_6 salts, a broad minimum in resistivity is observed at $T_\rho \simeq 240$ K [46], indicating that at T_{CO} the charge carriers are already (almost) completely localized. Furthermore, concerning question (i), a magnetic contribution due to 1D spin excitations is unlikely [168] as the sign of such a contribution is given by the pressure dependence of the exchange coupling constant [169], $\partial J/\partial p$, which is positive here[14]. Hence, this negative contribution may in-

[14]For the $(TMTTF)_2X$ salts, substitution of X = PF_6 by Br, corresponding to an increase of pressure (see

dicate any kind of unconventional lattice dynamics in the present systems, which can be understood within the "rigid-unit mode" (RUM) scenario, introduced in Section 4.6. As a possible mechanism, it could be considered that rotational or translational modes of rigid PF_6 or AsF_6 units linked to the TMTTF molecules via F-S halogen bonds could cause a negative contribution to α_i. Indeed, these octahedron anions (see Fig. 5.3), trapped in centrosymmetrical anion cavities delimited by the methyl groups [146], are known to be highly disordered at high temperatures and thought to rotate [171]. As discussed in previous sections, such RUM are likely to be the driving force of the negative thermal expansion (NTE) phenomenon [121,122]. As pointed out above, the CO transition seems to affect dramatically the overall behavior of the $\alpha_{c^*}(T)$ expansivity, as for the X = PF_6 and AsF_6 salts T_{CO} coincides roughly with the temperature below which the negative contribution to $\alpha_{c^*}(T)$ is no longer active. Above T_{CO}, CO fluctuations via F-S contacts cause positional fluctuations of the anions towards their new off-center equilibrium position, providing an effective damping of these modes. Accordingly, upon approaching T_{CO} from above, the anion motions become strongly reduced giving rise to a suppression of the negative contribution in α_{c^*} for $T < T_{CO}$. Interestingly enough, also in the $(TMTSF)_2PF_6$ salt, located in the metallic side of the phase diagram (Fig. 5.4), a negative contribution in the thermal expansion coefficient, though less pronounced than that observed in $(TMTTF)_2PF_6$, has been observed above $T \simeq 100$ K [168]. As pointed out by Monceau *et al.* [153] and Brazovskii [172], an incipient FE ordering may exist also in the $(TMTSF)_2X$ family, being hidden or existing only in a fluctuation regime. Hence, one could speculate that the negative contribution in the thermal expansion observed in $(TMTSF)_2PF_6$ reported in Ref. [168] provides evidence for this feature.

A possible answer for question (ii) might be related to the difference of the charge disproportionation ratio for both compounds. As discussed in the previous section, the estimated charge disproportionation ratio of about 2 : 1 for the X = AsF_6 salt [161] is much larger than 5 : 4, estimated for the X = PF_6 salt. Hence, a more pronounced anomalous behavior of α_{c^*} for the X = AsF_6 salt above T_{CO} might be linked to the charge disproportionation ratio, which in turn defines the shift of the anion from its centrosymmetrical position to stabilize the CO state [160]. The size of the counter ion ($AsF_6^- > PF_6^-$) should also play an important role. As discussed by Pouget *et al.* in Ref. [173], for anions of the the same symmetry T_{CO} increases as the anion size increases. For example, $T_{CO}^{X=SbF_6}$ = 154 K $> T_{CO}^{X=AsF_6}$ = 105 K $> T_{CO}^{X=PF_6}$ = 65 K. In fact, the anion size defines its free volume in the cavity as well as the intensity of the electron-anion coupling. Hence, more pronounced anomalous effects in c^*-axis for the X = AsF_6 salt above T_{CO} salt are likely to be related to this coupling.

Concerning question (iii), given the similarity in the shape of the anomalies at T_{CO} and T_{int} (Fig. 5.14) as well as the phenomenological link between the transition temperatures via $T_{int} \simeq 0.6 \cdot T_{CO}$ (cf. inset of Fig. 5.14), both features are undoubtedly related to each other. Possible scenarios include effects due to disorder, i.e. relaxor-type effects [166] either at T_{CO}, T_{int} (or at both) or two consecutive phase transitions associated with a change in the CO pattern. An interpretation for the anomaly at T_{int} in terms of a neutral-ionic (NI) transition, to be discussed in Section 5.5, cannot be ruled out.

The present findings (see Figs. 5.10, 5.11 and 5.12) provide strong evidence that the interstack c^*-axis plays a crucial role for the stabilization of the CO phase. The c^* direction is distinct in that it incorporates the anions X (see Figs. 5.2 and 5.3), while the *a*-axis lattice parameter, which is determined by the intrastack interactions between neighboring TMTTF molecules, remains practically unaffected, cf. Fig. 5.10. Hence, according to

Fig. 5.4), rises J from 420 K to 500 K [170].

the anisotropy observed in α_i with dominant effect in α_{c^*}, anions displacement and their coupling to the TMTTF molecules play a crucial role in the CO transition, as predicted theoretically [160]. Fig. 5.15 demonstrates a simple model [8], taking into account both the charge degrees of freedom on the TMTTF stacks (along the *a*-axis) as well as their coupling to the anions.

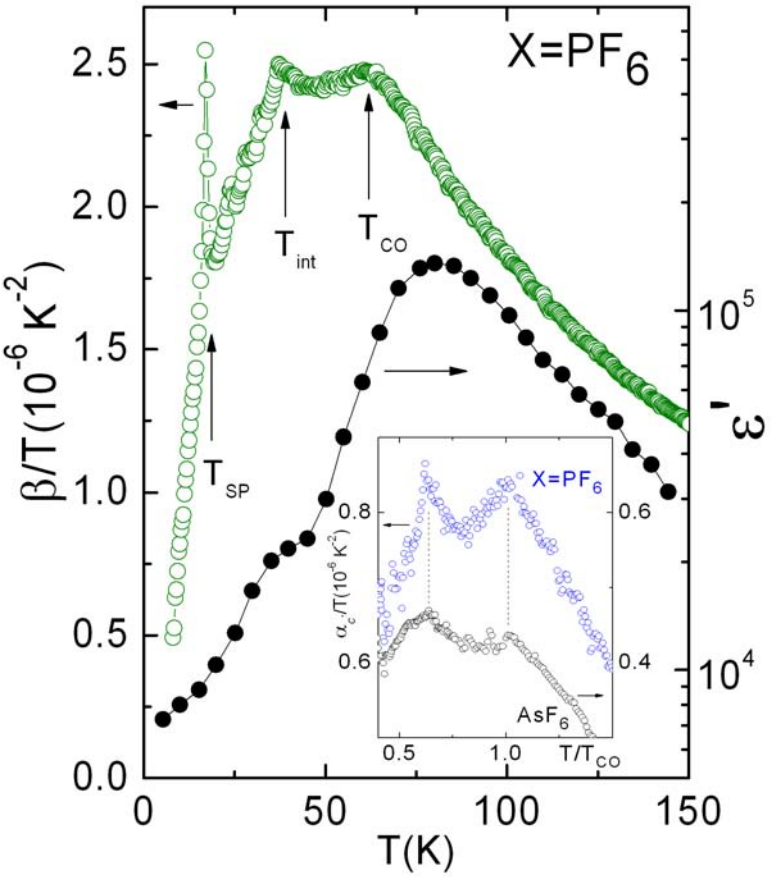

Figure 5.14: Main panel, left scale: Volumetric thermal expansion $\beta = \alpha_a + \alpha'_b + \alpha^*_c$ over T for (TMTTF)$_2$PF$_6$, obtained from the data set shown in Fig. 5.10. Arrows at T_{SP}, T_{int} and T_{CO} are defined in Fig. 5.10. Right scale: Real part of the dielectric constant ϵ', plotted on the same temperature scale. Data taken from Ref. [155]. Solid line in ϵ' data is guide for the eyes. Inset: α^*_c/T versus T/T_{CO} data for (TMTTF)$_2$X with X = PF$_6$ (left scale) and X = AsF$_6$ (right scale), showing that T_{CO} and T_{int} are linked by the relation $T_{int} \simeq 0.6 \cdot T_{CO}$.

The figure shows schematically the arrangements of TMTTF (hexagons) and the anions (circles) in the (b', c') plane (top panel) and the (a, b' + c') planes (bottom panel). Upon cooling through T_{CO}, the charge ρ on the TMTTF molecule changes from a homogeneous distribution with ρ = 0.5 (in units of e) above T_{CO} to a modulated structure which alternates by $\pm\delta$ along the TMTTF stacks below. For deriving the resulting 3D charge pattern, we start by considering a stack of anions along the ***a***-axis and the two nearest-neighbor stacks of TMTTF molecules linked via short S-F contacts (green line in Fig. 5.15). For a fixed charge modulation on one of the stacks, the electrostatic energy of the whole array can be reduced if one of the anions' nearest-neighbor TMTTF molecules is charge rich (TMTTF)$^{(\rho_0+\delta)}$ (black symbols), the other one charge poor (TMTTF)$^{(\rho_0-\delta)}$

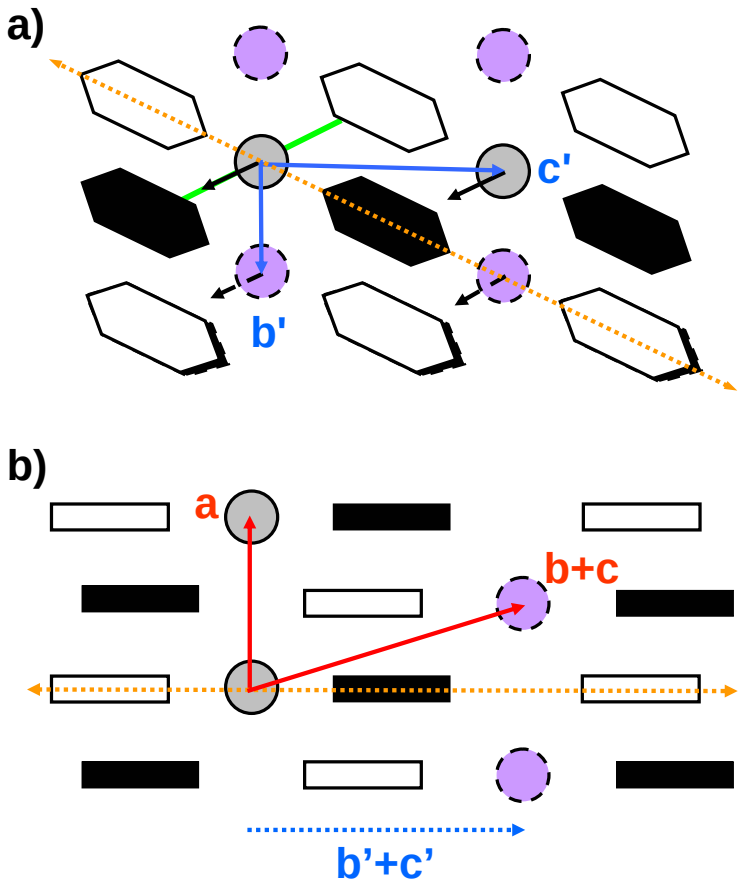

Figure 5.15: Schematic representation of the 3D ferroelectric character in the $(TMTTF)_2X$ family. a) Charge pattern in (b', c') plane. Black and white hexagons are used to represent charge rich- and charge poor-sites, i.e. $(TMTTF)^{0.5+\rho}$ and $(TMTTF)^{0.5-\rho}$, respectively. Dashed black hexagons are used to represent $(TMTTF)^{0.5+\rho}$ molecules located in another layer. Anions are represented by full and dashed circles. Arrows indicate displacements of the anions from their centro-symmetrical positions towards positive charged nearest-neighbor $(TMTTF)^{0.5+\rho}$ molecules, necessary for the stabilization of the CO phase. Green line exemplarily indicates short S-F contacts. b) View of the charge pattern in the (a, $b' + c'$) plane, indicated by orange dotted line in a).

(white symbols), while the anions perform slight shifts towards the charge rich ones. The resulting anion displacements (indicated by the arrows in Fig. 5.15), which are uniform for all anions and lift the inversion symmetry, together with the minimization of Coulomb energies of adjacent stacks along the $\boldsymbol{b}$ axis determine the 3D charge pattern unambiguously.

5.5 Evidence for a Neutral-Ionic Transition in $(TMTTF)_2X$

The main features related to a NI transition have already been introduced in Section 2.7. In the following, evidence for a NI transition in the $(TMTTF)_2X$ family is put forward. For the latter family of organic conductors, as discussed in Section 5.1, the stacks are weakly coupled to each other, being along the c-axis separated by counter ions. Upon cooling, the inter-site Coulomb repulsion V plays a major role and a CO transition coinciding with the onset of ferroelectricity [153] takes place at T_{CO}, with T_{CO}

being strongly anion dependent. Hence, below T_{CO}, the charge alternates along the stacks in a ... (0.5 + ρ) (0.5 - ρ) (0.5 + ρ) (0.5 - ρ) ... pattern (here (0.5 + ρ) and (0.5 - ρ) denote reach- and poor-charge sites, respectively), gives rise to an "effective mixed-stack" configuration, similar to that one intrinsic to mixed-stack charge-transfer salts, in which a NI transition has been observed. The inequivalent charge distribution[15] in the unit cell, i.e. ... $(TMTTF)^{0.5+\rho}$ $(TMTTF)^{0.5-\rho}$ ..., plays thus the role of a ... D A D A ... pattern, typical of conventional NI materials. In addition, it is noteworthy to mention that the spectral splitting observed in mid-infrared conductivity measurements (Fig. 5.9) [161] shows up below T_{CO} in form of very weak features. Interestingly enough, below T = 50 K and 70 K for the $(TMTTF)_2PF_6$ and $(TMTTF)_2AsF_6$ salts, respectively, a shift of the minimum to lower frequencies accompanied by a pronounced change in the shape of the line is observed. A remarkable aspect in the mid-infrared conductivity data is that pronounced features in the spectral splitting are observed below temperatures, which coincides with the T_{int} anomalies observed in α_{c^*} for the $(TMTTF)_2PF_6$ and $(TMTTF)_2AsF_6$ salts, discussed in this work. The mid-infrared conductivity data reported by Dumm *et al*. [161] for the $(TMTTF)_2PF_6$ and $(TMTTF)_2AsF_6$ salts is quite distinct from the optical absorption on (TTF-CA) [52], where the peak associated with the neutral-phase is continuously suppressed giving place to another well-defined peak associated with the ionic-phase. The deviation from the latter behavior in the $(TMTTF)_2PF_6$ and $(TMTTF)_2AsF_6$ salts might be due to sample to sample dependence or sample quality. The data shown in Fig. 5.9 indicate, however, that some additional feature appears at T_{int}. As already mentioned above, one of the most striking observations in favor of an interpretation of T_{int} in terms of a NI transition is the empirical relation $T_{int} \simeq 0.6 \cdot T_{CO}$, which fits roughly with the relation between peak positions in ϵ' for the (TTF-CA) [167], recognized as a model system for studying the NI transition. In addition, it is worth mentioning that according to the model proposed by Hubbard and Torrance to describe the NI transition [54] (discussed in Section 2.7), weak signatures in specific heat (or thermal expansion) are expected, showing up as a third-order transition, i.e. a kink in these quantities, like those observed at T_{int}. Yet, according to this model, due to the continuous polarization of the crystal lattice, the transition should be very broad ($\sim$30 K), being only the intermediary phase of the transition an actual Wigner crystal (or charge-ordered phase). In this case, the charge-ordered phase in the $(TMTTF)_2PF_6$ and $(TMTTF)_2AsF_6$ salts would be restricted to the temperature range $T_{int} < T < T_{CO}$. Furthermore, based on the arguments discussed above, it would be feasible to understand why the CO is easily destroyed under pressure (Fig. 5.8) in view of a NI transition. Upon applying pressure, the crystal volume is reduced. Consequently the energy balance between the Madelung energy and the cost of ionization is altered. Eventually the transition can be completely suppressed.

[15] If only one stack is considered, the existence of an electrical dipole in the unit cell could be proposed, with the electrical dipole moment vector $\overrightarrow{p}$ = q.$\overrightarrow{r}$ aligned along the stacks.

Chapter 6

Polymeric methyltrioxorhenium (poly-MTO)

6.1 Structure of poly-MTO

Polymeric methyltrioxorhenium (poly-MTO) $(CH_3)_{0.92}ReO_3$ is the first example of an inherently conductive organometallic polymeric oxide [174]. Its structural motive and transport properties (to be discussed below) are reminiscent of those of classical perowskites in two dimensions, cf. Fig. 6.1. The two dimensionality along the (ReO_2) planes, which are likely to be connected by Hydrogen bridges [174,175], was verified by X-ray powder diffraction measurements [176,177]. From the diffraction pattern obtained in these studies [176,177], all observed Bragg reflections can be indexed by a cubic lattice with parameters ranging from 3.66(5) to 3.68(5) Å. The asymmetry of the reflection profiles was assigned to the 2D character of the system. Based on these studies, poly-MTO fits in a 2D space group *P4mm* [177].

The sample studied in this work was synthesized by auto-polymerization of MTO in the melt[1] at 120 °C, resulting in golden-colored samples[2], as shown in Fig. 6.2. For the resistivity studies reported here, one sample of poly-MTO (labelled CH 022) was used.

6.2 Literature Results and Motivation

The metallic conductivity of poly-MTO has been attributed to the presence of demethylated Re atoms (at the level of about 10 %) giving rise to excess electrons which delocalize within the Re-5d bands [174, 175]. Interestingly, at the same time, magnetic susceptibil-

[1] According to Ref. [177], melting point of pure MTO is 106 °C.

[2] The polycrystal studied here was provided by PD Dr. E.-W. Scheidt, Chemische Physik und Materialwissenschaften Department - University of Augsburg.

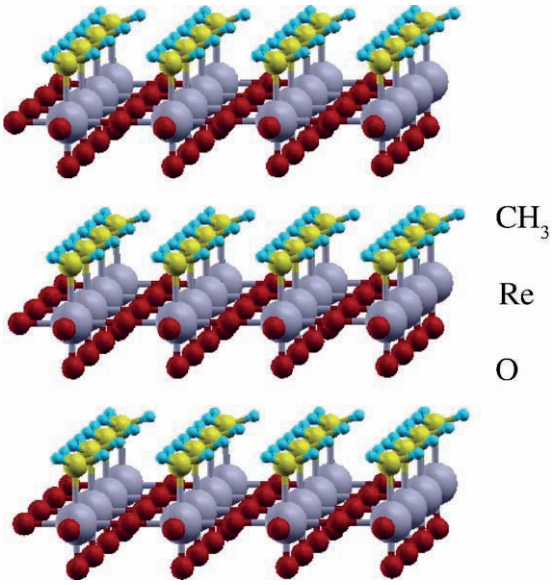

Figure 6.1: Model for the crystal structure of poly-MTO. Absence of reflections associated with the interlayer stacking in x-ray powder diffraction patterns suggests the existence of a 2D $(ReO_2)_\infty$ layered structure [177]. Picture taken from Ref. [176].

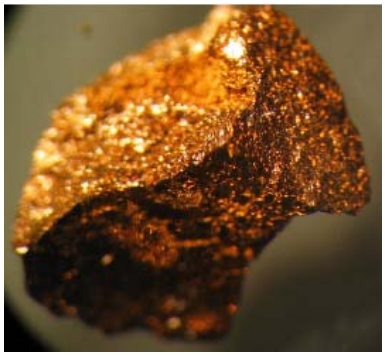

Figure 6.2: Sample of a polycrystal of poly-MTO. Picture taken from poster presentation of R. Miller *et al.*, Strongly Correlated Electron Systems Conference (SCES) 2005.

ity and magnetization measurements [176] indicate that a small portion of about 0.05% of the Re atoms remain in a localized $5d^1$ state, accompanied by a localized magnetic moment. Hence, the system can be considered as a quasi-2D electron gas of correlated electrons which is susceptive to weak disorder and which interacts with a diluted system of magnetic moments. The resistivity under zero and selected magnetic fields is shown in Fig. 6.3. Upon cooling under zero magnetic field (Fig. 6.3 a)), the system remains metallic ($d\rho/dT > 0$) down to about 30 K, below which the resistivity starts to increase. In this non-metallic range ($d\rho/dT < 0$), between 5 and 30 K the resistivity follows a $\ln(1/T)$ dependence. Below 5 K it starts to increase and saturates below about 2 K [178]. Interestingly enough, the anomalous resistivity of poly-MTO resembles the behavior found in the Zn-doped high-T_c superconductor $YBa_2Cu_3O_{7-\delta}$ [180], where the reversed situation is encountered: diluted non-magnetic Zn (replacing magnetic Cu) acting as scattering centers in an antiferromagnetically spin-correlated background. Common scenarios accounting for the above logarithmic behavior at low temperatures in the resistivity, such as, for example, a magnetic Kondo effect, which describes successfully

the electrons scattering that arise from magnetic impurities [188], or a 2D weak localization (Ref. [181] and references therein), which predicts that potential disorder in metals not only increases the residual resistance but also gives way to anomalous magnetic field dependences of the resistivity at low temperatures, seem to fail as they imply a reduction of the logarithmic increase in the presence of a magnetic field, which is in contrast to the findings for poly-MTO. As can be seen from Figs. 6.3 b) and c), the resistivity of poly-MTO at low temperatures increases under magnetic field. A scenario in terms of an Altshuler-Aronov correction, assuming a crossover of the charge-carrier diffusion from the 2D $(ReO_2)_\infty$ planes at high temperatures to a 3D diffusion at low temperatures, was proposed by E.-W. Scheidt *et al.* to explain the latter features [178]. According to the model proposed by Altshuler and Aronov [179], the $\ln(1/T)$ and $T^{1/2}$ dependence of the resistivity (Fig. 6.3) has its origin in a contribution related to an electron-electron scattering in the presence of a randomly distributed potential. In other words, the Altshuler-Aronov correction treats contributions which result from a combination of correlation effects and disorder.

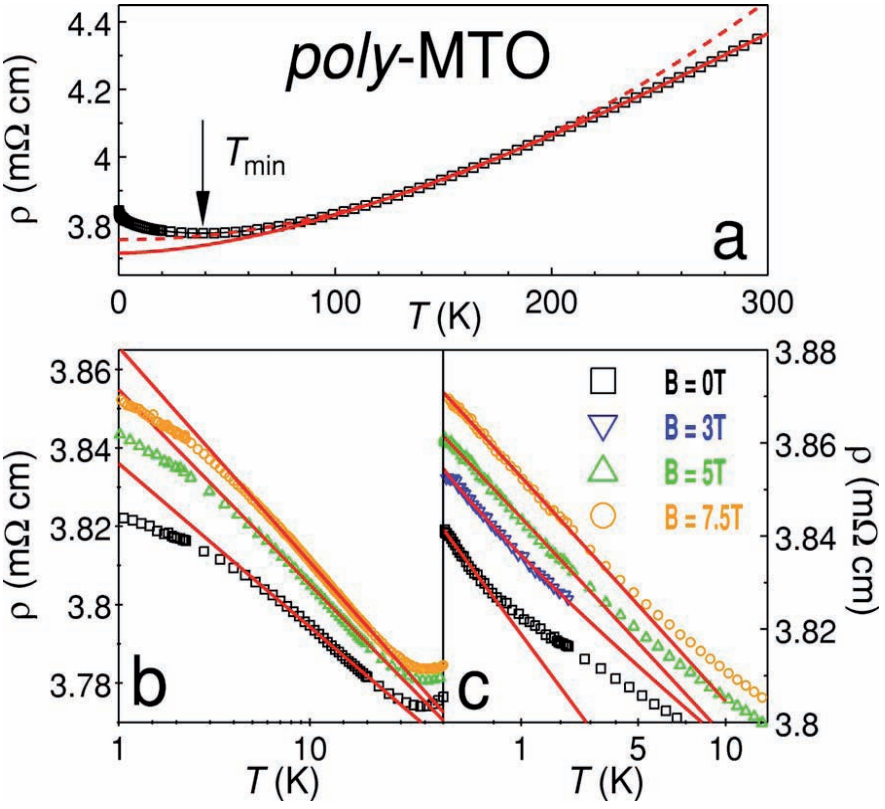

Figure 6.3: a) Temperature dependence of the resistivity $\rho(T)$ below 300 K. $T_{min} \simeq 38$ K refers to the metal-to-insulator transition temperature. Red dashed line is a $\rho(T) = \rho_0 + A_{ee}T^2$ fit (ρ_0 is the residual resistivity and A_{ee} the electron-electron scattering amplitute) in the temperature window 100 K $< T <$ 200 K. Red solid line is a $\rho(T) = \rho_0 + K(T/T_F)^2\, T^2 \ln(T_F/\mathrm{T})$ fit for $T >$ 90 K (K is a constant and T_F is the Fermi temperature). b) $\rho(T)$ in a semi-logarithmic representation for various magnetic fields, as indicated in the label of c). Solid lines are logarithmic fits in the temperature range 5 - 30 K. c) Resistivity data together with a plot according to $\rho(T) \propto T^{1/2}$ (red solid lines). Picture taken from [177].

Attempts to increase the conductivity of poly-MTO by intercalation with the organic donor molecule tetrathiafulvalene (TTF) proved unsuccessful: upon increasing the amount of TTF donors, the system becomes less conducting in the metallic high-temperature range and the resistivity upturn at $T \simeq 30$ K was strongly reinforced [176].

Another way to increase the conductivity and/or suppress the MI insulator transition at T_{min} (Fig. 6.3) may be by application of external hydrostatic pressure. Since pressure increases the intralayer- (and interlayer-) hopping, i.e. the bandwidth W, while leaving the disorder V_0 (V_0 is a measure of the width of the disorder potential) unaffected, pressure studies enable the quantity V_0/W to be varied and by this, eventually to tune the system towards the metallic state or even to induce superconductivity. In fact, the possibility of a pressure-induced superconducting transition was the main motivation for the present study. Hence, in order to obtain more information on the nature of the MI transition around 30 K, resistivity measurements under pressure using a Helium-gas pressure cell (described in Section 3.2.1) have been performed in the frame of the present work. The results are discussed in the next Section.

6.3 Transport Measurements on Poly-(MTO) Under Pressure

Resistivity measurements on poly-MTO have been performed by employing the gas-pressure cell described in Section 3.2.1. Measurements on cooling and warming up have been taken by varying the temperature in a rate of ± 6 K/h. No traces of hysteresis, at least in the resolution of the present experiments, have been observed in the present study. Fig. 6.4 shows resistivity data under ambient and selected pressures in the temperature range 2 - 300 K. The measurements were conducted in ten consecutive runs: ambient pressure, 200 bar, 1 kbar (after this measurement pressure was released completely), 3 kbar, 3 kbar (measurement was repeated to check reproducibility, same behavior was observed), 5 kbar, 8 kbar, 10 kbar, 10.55 kbar (maximal pressure achieved here) and a final run at ambient pressure. Measurements under 5, and 10 and 10.55 kbar are omitted here. In the following, the findings are discussed in detail. The measurement under ambient pressure reproduces nicely literature data (see Fig. 6.3, previous section) [177], small deviations in terms of absolute values are attributed to small errors in the estimate of the geometrical parameters of the sample (distance between the voltage contacts and sample cross-section, mainly due to the non-uniform shape of the sample, see Fig. 6.2.). However, the difference between the resistivity value at room temperature (RT) and the resistivity value at 2 K, which amounts to $(\rho_{RT} - \rho_{2\,K}) \simeq 0.4$ mΩcm, is roughly the same, indicating thus the reliability of the present experiments. Upon applying pressure, as can be seen from curves under 200 bar and 1 kbar in Fig. 6.4, a reduction of the resistivity over the whole temperature range investigated is observed. The data under pressures of 3 and 8 kbar will be discussed below. Fig. 6.5 depicts the resistivity under ambient pressure, 200 bar and 1 kbar below 100 K. An auxiliary horizontal line is used to demonstrate that the upturn of the resistivity at $T_{min} \simeq 30$ K, marking the metal-to-insulator transition, remains practically unaltered[3] when pressure is applied, at least for pressures until 1 kbar. Hence, the reduction of the resistivity under pressures of 200 bar and 1 kbar over the entire temperature range studied indicates that the elastic scattering due to impurities, which gives rise to the residual resistance ρ_0, is markedly reduced under pressure application. This is a particularly unusual feature as ρ_0 usually has its origin in defects or impurities randomly distributed throughout the crystal structure, which

[3] From the present studies, under ambient pressure, 200 bar and 1 kbar $(\rho_{2\,K} - \rho_{T_{min}})$ = (0.016 $\pm$ 0.004) mΩcm.

should not be affected by pressure. Interestingly, a reduction of the residual resistivity under pressure was also observed for the quasi-2D organic charge-transfer salt κ-(BEDT-TTF)$_2$Cu[N(CN)$_2$]Cl [102]. The physical origin of the latter feature, however, remains elusive. In the following, measurements under 3 and 8 kbar are discussed. Here, it is useful to recall that for measurements under ambient pressure, 200 bar and 1 kbar, pressure was applied continuously, i.e., firstly measurements under ambient pressure were performed, after that a pressure of 200 bar was applied and data taken. After finishing such measurements, pressure was increased from 200 bar up to 1 kbar and data taken again. However, after taking measurements under 1 kbar, pressure was completely released. After this, measurements under pressures above 1 kbar were performed and finally a measurement under ambient pressure was taken. We observed that the latter does not reproduce the starting measurement under ambient pressure. A possible explanation for this feature might be related to the induction of a strain on the polycrystal studied here during the measurements under pressure (200 bar and 1 kbar) before releasing of pressure. A remarkable aspect in the present data set is the observation of solidification of ^{4}He in the resistivity curves of poly-MTO under pressures of 3 and 8 kbar, cf. the arrows in Fig. 6.4. Therefore, one can conclude that upon solidifying, the pressure transmitter medium ^{4}He induces strains on the polycrystal. According to the literature [182], ^{4}He solidification implies a pressure reduction. Hence, an increase of the sample resistivity would be expected.

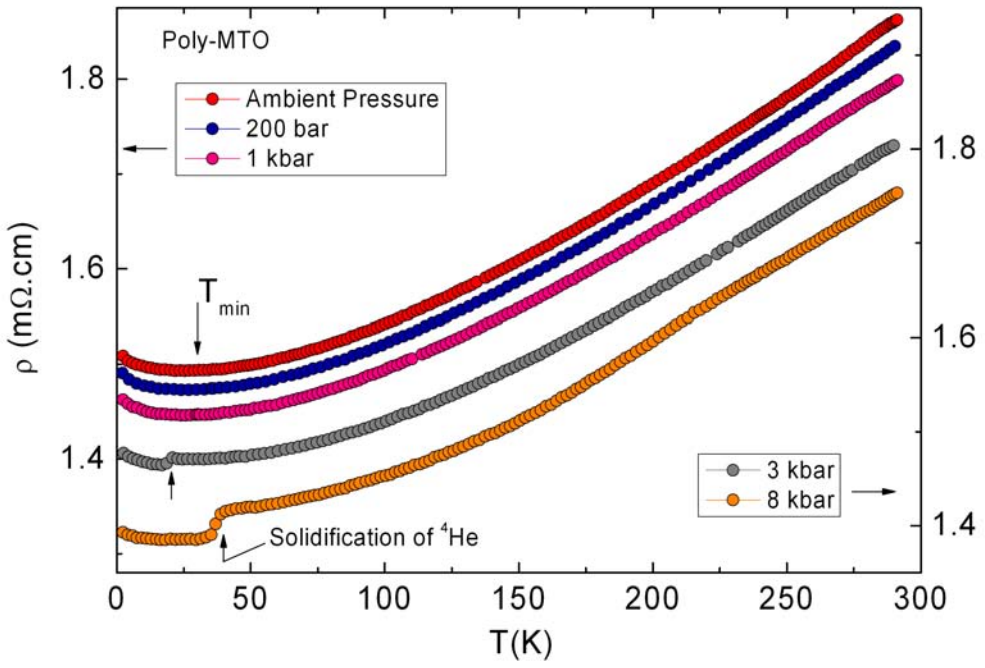

Figure 6.4: Resistivity for a polycrystal of poly-MTO in the temperature range 2 - 300 K poly-MTO at different pressures plotted in the same temperature scale. Left scale: resistivity data under ambient pressure, 200 bar and 1 kbar. Right scale: resistivity data under 3 and 8 kbar. Arrow down indicates the minimum of the resistivity around 30 K, while arrows up the solidification of the pressure transmitter medium ^{4}He at 3 and 8 kbar.

Nevertheless, in contrast to expectation, a reduction of the resistivity of the sample is observed, marked by an abrupt jump right on the ^{4}He solidification temperature. In-

terestingly enough, in the case of organic conductors discussed in previous chapters, see e.g. [97], such features, related to the solidification of ^{4}He, are not observed in experiments under pressure employing the same method. Hence, for the measurements under 3 and 8 kbar, an analysis of the data below the temperature at which ^{4}H solidifies is not reliable.

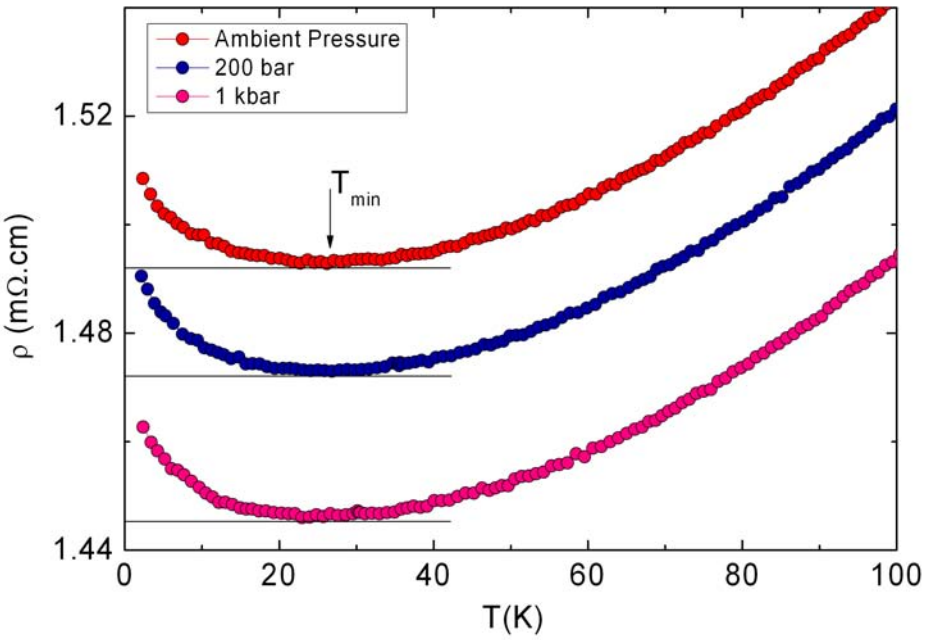

Figure 6.5: Resistivity for a polycrystal of poly-MTO below 100 K under ambient pressure, 200 bar and 1 kbar. The arrow indicates the MI transition around 30 K.

From the present studies under pressure on poly-MTO we conclude that hydrostatic pressure results in a reduction of the resistivity over the whole temperature range investigated, indicating therefore that pressure application implies a reduction of the residual resistivity. In addition, the present studies reveal that the metal-to-insulator transition at $T_{min} \simeq 30$ K remains unaffected under pressure until 1 kbar.

Chapter 7

Summary and Conclusions

In the field of strongly correlated electron systems, there is a long standing discussion on whether lattice degrees of freedom play a role for several physical phenomena, among them the Mott MI transition and charge-ordering transition. Charge-transfer salts of the κ-(BEDT-TTF)$_2$X and (TMTCF)$_2$X families have been revealed as model systems for the study of the latter phenomena. The (TMTCF)$_2$X salts have been recognized as model systems for studying correlation effects in 1D, while the (BEDT-TTF)-based materials for such studies in 2D. In this work, high-resolution dilatometry experiments were performed in order to address these issues. The main results obtained are summarized below.

Thermal expansion measurements on fully deuterated salts of κ-(BEDT-TTF)$_2$Cu[N(CN)$_2$]Br revealed discontinuous changes of the lattice parameters at the Mott metal-to-insulator transition temperature T_{MI} = 13.6 K, accompanied by a striking anisotropy. While huge effects are observed along the in-plane *a*-axis, along which the polymeric anion chains are aligned, an almost zero effect is observed along the second in-plane *c*-axis, along which the polymeric anion chains are linked via Br-N weak contacts. Still more amazing is the observation of pronounced lattice effects along the out-of-plane *b*-axis. These findings provide strong evidence that the Mott transition for the present class of materials cannot be described in the frame of a purely 2D electronic triangular dimer model. Furthermore, in order to achieve a better understanding of the Mott transition in the present material, thermal expansion measurements were taken under magnetic field, quasi-uniaxial pressure as well as by employing different cooling speeds across the glass-like transition. For example, measurements under magnetic field reveal the insensitivity of the Mott MI insulator temperature under fields up to 10 T, which is consistent with the proposal of a Mott insulating state with a hole localized on a dimer. A field-induced first-order transition at $T_{SF} \simeq 9.5$ K for a magnetic field applied along the *b*-axis was observed, indicative of a spin-flop transition with strong magneto-elastic coupling. Measurements under quasi-uniaxial pressure applied along

the out-of-plane *b*-axes revealed effects in contrast to those observed upon increasing the cooling speed across the glass-like transition. While quasi-uniaxial pressure shifts T_{MI} towards lower temperatures and T_p to higher temperatures, the opposite situation is observed upon fast cooling through the glass-like transition. Interestingly enough, the glass-like transition temperature transition T_g remains unaffected under quasi-uniaxial pressure. Although by means of thermal expansion measurements one has access to the macroscopic behavior of the sample studied, the strong anisotropic lattice effects observed, marked by a negative thermal expansion above T_g, enable us to draw some conclusions at the microscopic level. Hence, a model within the rigid-unit-mode scenario, taking into account the low-energy vibration modes of the cyanide ligands of the polymeric anions $Cu[N(CN)_2]Br^-$, was proposed to describe the negative thermal expansion above the $T_g \simeq 77$ K. In this model, low-energy vibration modes of the cyanide groups of the polymeric anion chains become frozen upon cooling dow to T_g, shrinking thus the *a* lattice parameter upon warming the system above T_g.

Thermal expansion measurements on the κ-(BEDT-TTF)$_2$Cu$_2$(CN)$_3$ salt, a system which is discussed currently as a candidate for the realization of a spin-liquid ground state, were reported for the first time in the present work. The measurements reported here, taken along the in-plane *c*-axis, reveal some new aspects, which can be of extreme importance for a wider understanding of the physical properties of this material. For example, the absence of the so-called glass-like transition in κ-(BEDT-TTF)$_2$Cu$_2$(CN)$_3$ is in line with the above-mentioned model within the rigid-unit modes scenario. While the anion $Cu[N(CN)_2]Br^-$ is arranged in form of chains weakly linked via Br-N contacts, the anions $Cu_2(CN)_3^-$ are arranged in a 2D network fashion, so that the cyanide groups are confined between the Cu atoms and therefore the vibration modes associated with the cyanide groups cannot propagate along the structure as it occurs, for example, in fully deuterated salts of κ-(BEDT-TTF)$_2$Cu[N(CN)$_2$]Br, cf. discussed above. A negative thermal expansion is observed for $14 < T < 50$ K. In addition, the thermal expansion coefficient reveals a huge anomaly indicative of a phase transition at T = 6 K, coinciding nicely with a hump in the specific heat, which has been assigned to a crossover to the quantum spin-liquid state, recently reported in the literature. Combining thermal expansion and specific heat data, a spin-fluctuation Grüneisen parameter $\Gamma_{sf} \simeq 30$ was obtained.

The quasi-1D (TMTTF)$_2$X salts (X = PF_6, AsF_6 and SbF_6) were also intensively studied in this work. The findings reported here revealed, for the first time, lattice effects associated with the charge-ordering (*structureless*) transition. Given the charge unbalancing imposed by the charge-ordering transition, uniform displacements of negative charged anions X^- from their symmetric positions towards positive charged nearest-neighbor $(TMTTF)^{0.5+\rho}$ are required to minimize the electrostatic energy. Hence, the present results demonstrate the importance of lattice effects/anion displacements for the stabilization of the charge-ordered phase, as predicted theoretically from calculations on the basis of the extended Hubbard model for small Peierls coupling. The anomalous expansivity along the c^*-axis, along which planes of TMTTF molecules are separated by planes of anions X, for $T_{CO} < T < 200$ K was interpreted considering the rigid-unit-mode scenario. Here, the situation is slightly different from the above-discussed model for taking into account negative thermal above T_g for fully deuterated salts of κ-(BEDT-TTF)$_2$Cu[N(CN)$_2$]Br along the *a*-axis, where vibration modes of cyanide groups of the anion were assumed to be frozen below T_g, giving way to negative thermal expansion when the temperature is increased above T_g. In the case of the (TMTTF)$_2$X salts (X = PF_6 and AsF_6), the thermal expansion coefficient along the c^*-axis remains positive with

a dramatic change of slope from $d\alpha_{c^*}/dT < 0$ above T_{CO} to $d\alpha_{c^*}/dT > 0$ below T_{CO}. This anomalous behavior can be understood in the light of the rigid-unit-mode scenario again. Although the charge-ordering transition in $(TMTTF)_2X$ can be nicely described by mean-field theory, as the dielectric constant obeys the Curie law, charge-ordering fluctuations show up well above the charge-ordered transition temperature T_{CO}. Such charge-fluctuations provoke, via weak S-F contacts, rotational or translational shifts of the rigid PF_6 or AsF_6 units from the center of the cavities delimited by the methyl groups. Right on the charge-ordering transition temperature (T_{CO} = 65 K and 105 K for X = PF_6 and AsF_6 salts, respectively), translational or vibrational modes of the anions are no longer active and, as consequence, a dramatic change of slope in the thermal expansion coefficient along the c^*-direction is observed. Based on the strong anisotropy observed, a scheme to demonstrate the 3D ferroelectric character of the charge-ordering transition, taking into account charge-degrees of freedom and anion displacements, was proposed. Furthermore, evidence for a new phase transition for the PF_6 and AsF_6 salts at $T_{int} \simeq 0.6 \cdot T_{CO}$ was presented. The similarities of the latter with the neutral-ionic transition in the mixed-stack TTF-CA charge-transfer salt was presented. Measurements along the c^*-axis on the $(TMTTF)_2X$ salt with X = SbF_6 revealed a discontinuous change of the lattice parameter at the charge-ordering transition temperature. The latter feature contrasts to the anomaly observed in X = PF_6 and AsF_6 salts at the charge-ordering transition temperature. This can be easily understood, as the charge-ordering transition in X = SbF_6 salt is accompanied by a Mott metal-to-insulator transition, which implies that above $T_{CO} = T_{MI}$ the material is still metallic. The anomaly observed at $T_{CO,MI}$ = 154 K, however, resembles that observed at the Mott transition in fully deuterated salts of κ-$(BEDT\text{-}TTF)_2Cu[N(CN)_2]Br$.

In the present work, resistivity measurements under hydrostatic pressure using a ^{4}He gas pressure were performed on the $(CH_3)_{0.92}ReO_3$ compound. The results for pressure until 1 kbar have shown a reduction of the resistivity over the temperature range investigated, indicating therefore that the residual resistivity is reduced, while the metal-to-insulator transition at $T_{MI} \simeq 30$ K remains unaffected.

Chapter 8

Perspectives and Outlook

In the present work, a few fundamental questions related to the role of lattice degrees of freedom for the Mott metal-to-insulator transition and charge-ordering transition in charge-transfer salts of the κ-(BEDT-TTF)$_2$X and (TMTTF)$_2$X families have been addressed. However, during the realization of this work, a few new questions have arisen and remain unanswered. In the following, some suggestions for further investigations related to the physics of the materials discussed in this work are presented.

Concerning fully deuterated salts of κ-(BEDT-TTF)$_2$Cu[N(CN)$_2$]Br, further in-plane (along the *a*- and *c*-axis) resistivity measurements are required in order to ascertain more information on the striking anisotropy observed in the directional-dependent thermal expansion measurements presented here. For the realization of such measurements, sizeable single crystals are necessary. In addition, resistivity measurements under hydrostatic pressure can provide information whether the samples studied in this work are actually located on the verge of the critical end point (P_0, T_0). By applying pressure, the MI transition should be suppressed and, similarly to fully hydrogenated salts of κ-(BEDT-TTF)$_2$Cu[N(CN)$_2$]Br, bulk superconductivity should take place. Thermal expansion measurements on fully deuterated salts of κ-(BEDT-TTF)$_2$Cu[N(CN)$_2$]Br under magnetic fields revealed a field-induced phase transition, described here in terms of a spin-flop transition accompanied by continuous suppression of the percolative superconductivity. Based on these results, magnetostriction measurements at selected temperatures, for instance at 6, 8, 10 and 12 K, can clarify the real character of these effects. If in fact a spin-flop transition takes place at fields of 0.5 T, a first-order transition should be observed in magnetostriction experiments below $T \simeq 9$ K. Such experiments will thus enable a more precise mapping of the speculative H-T phase diagram (see Fig. 4.20) proposed in this work. Owing to the rigid-unit-mode scenario proposed here, which is based on the low-energy vibration modes of the cyanide groups of the polymeric anion, to describe negative thermal expansion above the glass-like anomaly, systematic Raman and/or infra-red studies are required to support this description. In addition, such stud-

ies will reveal whether the Mott MI transition is accompanied by any symmetry breaking or not. In fact a symmetry break would be expected if the endpoint of the first-order MI transition line is a tricritical point, as suggested by the present experiments.

Now, considering the κ-$(ET)_2Cu_2(CN)_3$ charge-transfer salt, more information on the sharp anomaly observed at T = 6 K can be gained by performing directional-dependent thermal expansion measurements along the out-of-plane *a*-axis in order to check, for instance, if a positive or negative Poisson's ratio is observed as well as to check either β/T remains finite or if it vanishes as $T \rightarrow 0$. In addition, systematic thermal expansion at very low-T will tell us either α/T presents an activated behavior [187] or if α/T follows a linear behavior [5] as $T \rightarrow 0$.

For the $(TMTTCF)_2X$ salts, directional-dependent thermal expansion measurements on $(TMTTF)_2SbF_6$ are important in order to look for anisotropic effects at the charge-ordering transition which in turn is accompanied by a Mott metal-to-insulator transition. In addition, given the high resolution of the thermal expansion setup of the group of Prof. Dr. Michael Lang, systematic measurements on the TMTSF family are important in order to check the existence of *hidden* ferroelectricity, as suggested in Ref. [153]. In addition, measurements on the $(TMTSF)_2ClO_4$ superconductor around the anion-ordering transition will reveal whether there exist similarities between the anion-ordering and the glass-like transition observed in fully deuterated/hydrogenated salts of κ-$(BEDT\text{-}TTF)_2Cu[N(CN)_2]Br$.

Finally, thermal expansion measurements on (TTF-CA) can reveal indirectly whether there exist some similarities between the features observed at the charge-ordering transition in $(TMTTF)_2X$ (X = PF_6 and AsF_6) at T_{int} and T_{CO} and therefore verify if the proposal of a neutral-ionic transition in the latter salts is plausible, as proposed in Section 5.5.

Thus various new avenues stemming from the current project are opened and I hope that this dissertation may serve as a base for these future projects.

Bibliography

[1] T.H.K. Barron , J.G. Collins and G.K. White, Thermal Expansion of Solids at Low Temperatures, Adv. Phys. **29**, 609-730 (1980).

[2] N. Toyota, M. Lang and J. Müller, Low-Dimensional Molecular Metals, Springer, Germany (2007).

[3] A. Kawamoto, K. Miyagawa and K. Kanoda, Phys. Rev. B **55**, 14140 (1997).

[4] M. de Souza, A. Brühl, Ch. Strack, B. Wolf, D. Schweitzer and M. Lang, Phys. Rev. Lett. **99**, 037003 (2007).

[5] S. Yamashita, Y. Nakazawa, M. Oguni, Y. Oshima, H. Nojiri, Y. Shimizu, K. Miyagawa and K. Kanoda, Nature Physics **4**, 459 (2008).

[6] D.S. Chow , F. Zamborszky, B. Alavi, D.J. Tantillo, A. Baur, C.A. Merlic, and S. E. Brown, Phys. Rev. Lett. **85**, 1698 (2000).

[7] H. Seo and H. Fukuyama, J. Phys. Soc. Jpn. **66**, 1249 (1997).

[8] M. de Souza, P. Foury-Leylekian, A. Moradpour, J.-P. Pouget and M. Lang, Phys. Rev. Lett., in press, pre-print in cond-mat/0807.0735v1.

[9] E. Grüneisen, Annalen der Physik **331**, 393 (1908).

[10] J.S.O. Evans, J. Chem. Soc., Dalton Trans. **19**, 3317 (1999); G.D. Barrera, J.A.O Bruno, T.H.K. Barron and N.L. Allan, J. Phys.: Condens. Matter **17**, R217 (2005).

[11] J. Müller, M. Lang, F. Steglich, J.A. Schlueter, A.M. Kini, U. Geiser, J. Mohtashman, R.W. Winter, G.L. Gard, T. Sasaki and N. Toyota, Phys. Rev. B **61**, 11739 (2000).

[12] G. Gladstone, M.A. Jensen and J.R. Schrieffer: In: Superconductivity Vol. **2** ed. by R.D. Parks (M. Dekker, New York 1969) p. 655.

[13] C. Meingast, B. Blank, H. Bürkle, B. Obst, T. Wolf, H. Wühl, V. Selvamanickam and K. Salama, Phys. Rev. B **41**, 11299 (1990).

[14] M. Lang and J. Müller, *Organic Superconductors* in *The Physics of Superconductors* Vol. II, K.H. Bennemann, J.B. Ketterson (eds.) p. 435-554 (Springer-Verlag), Berlin (2004).

[15] K. Huang, Statistical Mechanics Wiley, New York (1987).

[16] See, e.g., L.E. Reichl, A Modern Course in Statistical Physics, 2^{nd} Edition, Wiley-Interscience Publication, USA (1998), p. 96; W. Greiner, L. Neise and H. Stöker, Thermodynamics and Statistical Physics, Springer, New York (1995), p. 416; a nice discussion (in Portuguese) about continuous and discontinuous phase transitions was made by J.A. Souza, Ph.D. Thesis, University of São Paulo, São Paulo (2006).

[17] L.D. Landau and E.M. Lifshitz, Statistical Physics, Pergamon, London (1959) p. 482.

[18] L.P. Kadanoff, W. Götze, D. Hamblen, R. Hecht, E.A.S. Lewis, V.V. Palciauskas, M. Rayl and J. Swift, Rev. Mod. Phys. **39**, 395-431 (1967).

[19] P. Limelette, A. Georges, D. Jerome, P. Wzietek, P. Metcalf and J.M. Honig, Science **302**, 89 (2003).

[20] V.P. LaBella, D.W. Bullock, M. Anser, Z. Ding, C. Emery, L. Bellaiche and P.M. Thibado, Phys. Rev. Lett. **84**, 4152 (2000).

[21] V. Pasler, P. Schweiss, C. Meingast, B. Obst, H. Wühl, A. I. Rykov and S. Tajima, Phys. Rev. Lett. **81**, 1094 (1998).

[22] F. Kagawa, K. Miyagawa and K. Kanoda, Nature **436**, 534 (2005).

[23] W.A. Little, Phys. Rev. **134**, A1416 (1964).

[24] D.C. Mattis, The Many-body Problem: an Encyclopedia of Exactly Solved Models in One Dimension, World Scientific (1993); Z.N.C. Ha, Quantum Many-Body Systems in One Dimension, World Scientific, Singapore (1996).

[25] N.D. Mermin and H. Wagner, Phys. Rev. Lett. **17**, 1133 (1966).

[26] G.D. Mahan, Many Particle Physics. Second Edition, Plenum, New York (1990).

[27] J.M. Luttinger, J. Math. Phys. **4**, 1154 (1963).

[28] O. M. Auslaender, A. Yacoby, R. de Picciotto, K.W. Baldwin, L.N. Pfeiffer and K.W. West, Phys. Rev. Lett. **84**, 1764 (2000).

[29] H. Ishii, H. Kataura, H. Shiozawa, H. Yoshioka, H. Otsubo, Y. Takayama, T. Miyahara, S. Suzuki, Y. Achiba, M. Nakatake, T. Narimura, M. Higashiguchi, K. Shimada, H. Namatame and M. Taniguchi, Nature **426**, 540 (2003).

[30] R.E. Peierls, "Quantum theory of solids", Clarendon, Oxford (1955).

[31] G. Grüner, Rev. Mod. Phys. **60**, 1129 (1988).

[32] A. Nothardt, Ph.D. Thesis (in German), University of Stuttgart (2005).

[33] S. Kagoshima, H. Nagasawa and T. Sambongi, One-Dimensional Conductors, Springer-Verlag, Berlin Heidelberg (1988).

[34] K. Petukhov, Ph.D. Thesis, University of Stuttgart (2003).

[35] D. Jérome, in Organic Conductors: Fundamentals and Applications, ed. by J. P. Farges, Marcel Dekker, New York (1994).

[36] S. Lefebvre, P. Wzietek, S. Brown, C. Bourbonnais, Jérome, C. Méziere, M. Fourmigué and P. Batail, Phys. Rev. Lett. **85**, 5420 (2000).

[37] N.D. Mathur, F.M. Grosche, S.R. Julian, I.R. Walker, D.M. Freye, R.K.W. Haselwimmer and G.G. Lonzarich, Nature **394**, 39 (1998).

[38] J. Orenstein and A.J. Millis, Science **288**, 468 (2000); M. Maple, J. of Magn. and Mag. Mat. **177**, 18 (1998).

[39] P. Monthoux, D. Pines and G.G. Lonzarich, Nature **450**, 1177 (2007).

[40] F. Gebhard, The Mott Metal-Insulator Transition, Springer Tracts in Modern Physics, Volume **137**, Springer-Verlag Berlin Heidelberg (1997).

[41] In fact, as nicely discussed by René Descartes in *Discours de la Méthode*, Paris, Flammarion (1642), if one has a complex problem to be solved, one should start solving the more simple parts of the problem until achieving the solution of the more complex parts. This law holds in all areas of the knowledgement.

[42] J.C. Bonner and M.E. Fisher, Phys. Rev. **135**, A640 (1964).

[43] D.C. Johnston, R.K. Kremer, M. Troyer, X. Wang, A. Klümper, S.L. Bud'ko, A.F. Panchula and P.C. Canfield, Phys. Rev. B **61**, 9558 (2000).

[44] S. Eggert, I. Affleck and M. Takahashi, Phys. Rev. Lett. **73**, 332 (1994).

[45] B. Salameh, Ph.D. Thesis, University of Stuttgart (2005).

[46] M. Dressel, Naturwissenschaften **94**, 527 (2007).

[47] J. Hubbard, Phys. Rev. B **17**, 494 (1978).

[48] J. Moldenhauer, Ch. Horn, K. I. Pokhodnia and D. Schweitzer, Synthetic Metals **60**, 31 (1993).

[49] K. Hiraki and K. Kanoda, Phys. Rev. Lett. **80**, 4737 (1998).

[50] S. Horiuchi, R. Kumai, Y. Okimoto and Y. Tokura, Chem. Phys. **325**, 78 - 91 (2006).

[51] Charles Kittel, Introduction to Solid State Physics, 7th Edition, p. 68, John Wiley and Sons, USA (1996).

[52] J.B. Torrance, A. Girlando, J.J. Mayerle, J.I. Crowley, V.Y. Lee and P. Batail, Phys. Rev. Lett. **47**, 1747 (1981).

[53] J.B. Torrance, J.E. Vazquez, J.J. Mayerle and V.Y. Lee, Phys. Rev. Lett. **46**, 253 (1981).

[54] J. Hubbard and J.B. Torrance, Phys. Rev. Lett. **47**, 1750 (1981).

[55] N.F. Mott, Rev. Mod. Phys. **40**, 677 (1968).

[56] N.F. Mott, Metal-Insulator Transitions, Second Edition, Taylor and Francis (1990).

[57] G. Kotliar and D. Vollhardt, Physics Today, March 2004, 53-59.

[58] O. Madelung, Introduction to Solid State Physics, Springer, Berlin (1978), p. 363.

[59] D.B. McWhan, T.M. Rice and J.P. Remeika, Phys. Rev. Lett. **23**, 1384 (1969).

[60] R. Pott and R. Schefzyk, J. Phys. E **16**, 445 (1983).

[61] M. Lang, Ph.D. Thesis (in German), Darmstadt Technical University, Darmstadt (1991).

[62] J. Müller, Ph.D. Thesis (in German), Max-Planck-Institute, Dresden, Germany (2001).

[63] A. Brühl, Ph.D. Thesis (in German), University of Frankfurt (2007).

[64] J.W. Loram, K.A. Mirza, C.P. Joyce and A.J. Osborne, Europhys. Lett. **8**, 263 (1989).

[65] E.I. Geshko, V.P. Mikhal'chenko and B.M. Sharlai, Soviet Phys. - Solid State **14**, Number 6, 1554 (1972).

[66] P.W. Bridgman, Phys. Rev. **48**, 893 (1935).

[67] I.R. Walker, Rev. of Sci. Instr. **70**, 3402 (1999).

[68] S. Reich and T. Godin, Meas. Sci. Technol., 1079-1082 (1996).

[69] I. Umehara, F. Tomioka, A. Tsuboi, T. Ono, M. Hedo and Y. Uwatoko, J. of Magn. and Mag. Mat. **272-276**, 2301-2302 (2004).

[70] Y. Uwatoko, T. Fujiwara, M. Hedo, F. Tomioka and I. Umehara, J. Phys.: Condens. Matter **17**, S1011-1016 (2005).

[71] G.J. Piermarini and S. Block, Rev. of Phys. Chem. of Jpn., 851 Suppl. I (1975).

[72] L. Merril and W.A. Bassett , Rev. of Sci. Instr. **45**, 290-294 (1974).

[73] For more information about this pressure cell, see Instruction Manual - Gas Pressure Cell GC10 from High Pressure Research Center, Polish Academy of Sciences, Warszawa, Poland.

[74] W.F. Sherman and A.A. Stadtmuller, Experimental Techniques in High-Pressure Research, John Wiley and Sons LTD (1987).

[75] M. Lang, Superconductivity Review **2**, 1 (1996).

[76] T. Ishiguro and K. Yamaji, *Organic Superconductors* in Springer Series in Solid-State Sciences 88, Springer-Verlag, Germany (1990).

[77] D. Jérome, The Physics of Organic Superconductors, in Science, New Series **252**, 1509 (1991).

[78] R.H. McKenzie, Comments Condensed Matter Physics **18**, 309-337 (1998).

[79] J. Wosnitza, Studies of High Temperature Superconductors **34**, Nova Science Publishers, 97-131 (2000).

[80] J. Singleton, Journal of Solid State Chemistry **168**, 675 (2002).

[81] K. Miyagawa, K. Kanoda and A. Kawamoto, Chem. Rev. **104**, 5635-5653 (2004).

[82] H. Fukuyama, J. Phys. Soc. Jpn. **75**, 051001-1 (2006).

[83] H. Mori, J. Phys. Soc. Jpn. **75**, 051003-1 (2006).

[84] K. Kanoda, J. Phys. Soc. Jpn. **75**, 051007-1 (2006).

[85] B.J. Powell and R.H. McKenzie, J. Phys.: Condens. Matter **18**, R827-R866 (2006).

[86] J. Müller, M. Lang, F. Steglich, J. A. Schlueter, A.M. Kini and T. Sasaki, Phys. Rev. B **65**, 144521 (2002).

[87] T. Sasaki, N. Yoneyama, N. Kobayashi, Y. Ikemoto and H. Kimura, Phys. Rev. Lett. **92**, 227001 (2004).

[88] R.H. Mckenzie, Comments Condens. Matter Phys. **18**, 309 (1998).

[89] J.A. Schlueter, U. Geiser, M.A. Whited, N. Drichko, B. Salameh, K. Petukhov and M. Dressel, Dalton Transactions **2007**, 2580 (2007).

[90] A. M. Kini, U. Geiser, H.H. Wang, K.D. Carlson, J.M. Williams, W.K. Kwok, K.G. Vandervoort, J.E. Thompson, D.L. Stupka, D. Jung and M.-H. Whangbo, Inorg. Chem. **29**, 2555 (1990).

[91] U. Geiser, A.J. Schutz, H.H. Wang, D.M. Watkins, D.L. Stupka, J.M. Williams, J.E. Schirber, D.L. Overmyer, D. Jung, J.J. Novoa and M.-H, Whangbo, Physica C **174**, 475 (1991).

[92] U. Geiser, H.H. Wang, K.D. Carlson, J.M. Williams, H.A. Charlier, J.E. Heindl, G.A. Yaconi, B.J. Love, M.W. Lathrop, J.E. Schirber, D.L. Overmyer, J. Ren and M.-H. Whangbo, Inorg. Chem. **30**, 2586 (1991).

[93] K. Hartke, Th. Kissel, J. Quante and R. Matusch, Chem. Ber. **113**, 1898 (1980).

[94] M. Mizuno, A. Garito and M. Cava, J. Chem. Soc. Chem. Commun. **1978**, 18 (1978).

[95] S. Gärtner, D. Schweitzer and H.J. Keller, Synthetic Metals **44**, 227 (1991).

[96] E. Grieβhaber, Ph.D. Thesis (in German), University of Stuttgart (2000).

[97] Ch. Strack, C. Akinci, V. Pashchenko, B. Wolf, E. Uhrig, W. Assmus, M. Lang, J. Schreuer, L. Wiehl, J. A. Schlueter, J. Wosnitza, D. Schweitzer, J. Müller and J. Wykhoff , Phys. Rev. B **72**, 054511 (2005).

[98] R.H. Mckenzie, Science **278**, 820 (1997).

[99] E. Dagoto, Science **309**, 257 (2005).

[100] O.J. Taylor, A. Carrington and J.A. Schlueter, Phys. Rev. Lett. **99**, 057001 (2007).

[101] D. Fournier, M. Poirier, M. Castonguay and K.D. Truong, Phys. Rev. Lett. **90**, 127002 (2003).

[102] P. Limelette, P. Wzietek, S. Florens, A. Georges, T.A. Costi, C. Pasquier, D. Jérome, C. Mézière and P. Batail, Phys. Rev. Lett. **91**, 016401 (2003).

[103] M. Lang, M. de Souza, A. Brühl, Ch. Strack, B. Wolf, J.A. Schlueter, J. Müller and D. Schweitzer, *Proceedings of the 8^{th} Intern. Conf. on Materials and Mechanisms of Superconductivity - High Temperature Superconductors*, Physica C **460-462**, 129 (2007).

[104] F. Kagawa, T. Itou, K. Miyagawa and K. Kanoda, Phys. Rev. B **69**, 064511 (2004).

[105] S. Papanikolaou, R.M. Fernandes, E. Fradkin, P.W. Phillips, J. Schmalian and R. Sknepnek, Phys. Rev. Lett. **1**, 026408 (2008).

[106] K. Kanoda, Hyperfine Interact. **104**, 235 (1997).

[107] A. Kawamoto, K. Miyagawa, Y. Nakazawa and K. Kanoda, Phys. Rev. B **52**, 15522 (1995).

[108] S.R. Hassan, A. Georges and H.R. Krishnamurthy, Phys. Rev. Lett. **94**, 036402 (2005).

[109] J. Merino and R.H. McKenzie, Phys. Rev. B **62**, 16442 (2000).

[110] Y. Shimizu, K. Miyagawa, K. Kanoda, M. Maesato and G. Saito, Phys. Rev. Lett. **91**, 107001-1 (2003).

[111] Y. Kurosaki, Y. Shimizu, K. Miyagawa, K. Kanoda and G. Saito, Phys. Rev. Lett. **95**, 177001-1 (2005).

[112] P.W. Anderson, Mat. Res. Bull. **8**, 153 (1973).

[113] P.W. Anderson, Science **235**, 1196 (1987).

[114] A.P. Ramirez, Nature Physics **4**, 442 (2008).

[115] S.-S. Lee, P.A. Lee and T. Senthil, Phys. Rev. Lett. **98**, 067006 (2007).

[116] K. Miyagawa, A. Kawamoto and K. Kanoda, Phys. Rev. Lett. **89**, 017003 (2002).

[117] D. Chasseau, Synth. Met., **42**, 2039 (1991).

[118] R. Lakes, Sience **235**, 1038 (1987).

[119] M. Lang, M. de Souza, A. Brühl, Ch. Strack, B. Wolf and D. Schweitzer, Physica B **403**, 1384 (2008).

[120] A.U.B. Wolter, R. Feyerherm, E. Dudzik, S. Süllow, Ch. Strack, M. Lang and D. Schweitzer, Phys. Rev. B **75**, 104512 (2007).

[121] A.L. Goodwin, M. Calleja, M.J. Conterio, M.T. Dove, J.S.O. Evans, D.A. Keen, L. Peters and M.G. Tucker, Science **319**, 794 (2008).

[122] A.L. Goodwin and C.J. Kepert, Phys. Rev. B **71**, 140301 (2005).

[123] T.A. Mary, J.S.O. Evans, T. Vogt and A.W. Sleight, Science **272**, 90 (1996).

[124] S. Roth, One-Dimensional Metals, VCH Publishers, Germany (1995).

[125] H. Elsinger, J. Wosnitza, S. Wanka, J. Hagel, D. Schweitzer and W. Strunz, Phys. Rev. Lett. **84**, 6098 (2000).

[126] Y. Nakazawa, H. Taniguchi, A. Kawamoto and K. Kanoda, Phys. Rev. B **61**, R16295 (2000).

[127] U. Welp, S. Fleshler, W.K. Kwok, G.W. Crabtree, K.D. Carlson, H.H. Wang, U. Geiser, J.M. Williams and V. M. Hitsman, Phys. Rev. Lett. **69**, 840 (2000).

[128] M. Pinterić, M. Miljak, N. Biškup, O. Milat, I. Aviani, S. Tomić, D. Schweitzer, W. Strunz, and I. Heinen, Eur. Phys. J. B **11**, 217 (2000).

[129] K. Miyagawa, A. Kawamoto, Y. Nakazawa and K. Kanoda, Phys. Rev. Lett. **75**, 1174 (1995).

[130] F. Kagawa, T. Itou, K. Miyagawa and K. Kanoda, Phys. Rev. Lett. **93**, 127001 (2004).

[131] D.F. Smith, S.M. De Soto, C.P. Slichter, J.A. Schlueter, A.M. Kini and R.G. Daugherty, Phys. Rev. B **68**, 024512 (2000).

[132] D.F. Smith, C.P. Slichter, J.A. Schlueter, A.M. Kini and R.G. Daugherty, Phys. Rev. Lett. **93**, 167002 (2004).

[133] A. Kawamoto, M. Yamasita and K.-I. Kumagai, Phys. Rev. B **70**, 212506 (2004).

[134] H. Taniguchi, A. Kawamoto and K. Kanoda, Phys. Rev. B **59**, 8424 (1999).

[135] H. Taniguchi, A. Kawamoto and K. Kanoda, Phys. Rev. B **67**, 014510 (2003).

[136] A.P. Ramirez, A. Hayshi, R.J. Cava, R. Siddharthan and B.S. Shastry, Nature **399**, 333 (1999).

[137] L. Pauling, J. of the Am. Chem. Soc. **57**, 2680 (1935).

[138] Q.A. Pankhurst, C.E. Johnson, D.H. Jones and M.F. Thomas, Hyperfine Interact. **41**, 505 (1988).

[139] X. Su, F. Zuo, J.A. Schlueter, A.M. Kini and J.M. Williams, Phys. Rev. B **58**, R2944 (1998).

[140] E. Griesshaber, M. Schiller, D. Schweitzer, I. Heinen and W. Strunz, Phyisica C **317**, 421 (1999).

[141] J.A. Souza, Y.-K. Yu, J.J. Neumeier, H. Terashida and R.F. Jardim, Phys. Rev. Lett. **94**, 207209 (2005).

[142] A. Fujita, T. Suzuki, N. Kataoka and K. Fukamichi, Phys. Rev. B **50**, 6199 (1994).

[143] Z. Schlesinger, J.A. Rosen, J.N. Hancock and A.P. Ramirez, Phys. Rev. Lett. **101**, 015501 (2008).

[144] A. Visser, A. Lacerda, P. Haen, J. Flouquet, F.E. Kayzel and J.J.M. Franse, Phys. Rev. B **39**, 11301 (1989).

[145] V. Vescoli, L. Degiorgi, W. Henderson, G. Grüner, K.P. Starkey and L.K. Montgomery, Science **281**, 1181 (1998) and reference 4 therein.

[146] J.-P. Pouget and S. Ravy, J. Phys. I (France) **6**, L393 (1984).

[147] B. Gallois, Ph.D. Thesis (in French), University of Bordeaux (1987).

[148] D. Chasseau, J. Gaultier, J. L. Miane, C. Coulon, P. Delhaes, S. Flandrois, J. M. Fabre and L. Giral, J. Phys. Colloq. France **44**, C3-1223 (1983).

[149] P. Vaca, C. Coulon, B. Gallois, J.-P. Pouget and J.M. Fabre, J. Phys. I **1**, 125 (1991).

[150] R. Laversanne, C. Coulon, B. Gallois, J.-P. Pouget and R. Moret, J. Phys. Lett. (France) **45**, L393 (1984).

[151] D. Jérome, A. Mazaud, M. Ribault and K. Bechgaard, J. Phys. Lett. **41**, L95 (1980).

[152] T. Adachi, E. Ojima, K. Kato and H. Kobayashi, J. Am. Chem. Soc. **122**, 3238 (2000).

[153] P. Monceau, F.Ya. Nad and S. Brazovskii, Phys. Rev. Lett. **86**, 4080 (2001).

[154] F. Nad, P. Monceau, C. Carcel and J.M. Fabre, Phys. Rev. B **62**, 1753 (2000).

[155] F. Nad and P. Monceau, J. Phys. Soc. Jpn. **75**, 051005-1 (2006).

[156] C. Coulon, S.S.P. Parkin, R. Laversanne, Mol. Crys. Liq. Cryst. **119**, 325 (1985).

[157] H.H.S. Javadi, R. Laversanne and A.J. Epstein, Phys. Rev. B **37**, 4280 (1988).

[158] F. Zamborszky, W. Yu, W. Raas, S.E. Brown, B. Alavi, C.A. Merlic and A. Baur, Phys. Rev. B **66**, 081103 (2002).

[159] W. Yu, F. Zhang, F. Zamborszky, B. Alavi, A. Baur, C.A. Merlic and S.E. Brown, Phys. Rev. B **70**, 121101 (2004).

[160] J. Riera and D. Poiblanc, Phys. Rev. B **63**, 241102-1 (2001).

[161] M. Dumm, M. Abaker and M. Dressel, J. Phys. IV France **131**, 55 (2005).

[162] M. Meneghetti, R. Bozio, I. Zanon, C. Pecile, C. Ricotta and M. Zanetti, J. Chem. Phys. **80**, 6210 (1984).

[163] J.-P. Pouget, R. Moret, R. Comes, K. Bechgaard, J.M. Fabre and L. Giral, Mol. Cryst. and Liq. Cryst. **79**, 485 (1982).

[164] K. Imai, J. Phys. Soc. Jpn. **43**, 1320 (1977).

[165] S. Sawada and G. Shirane, J. Phys. Soc. Jpn. **4**, 52 (1949).

[166] Z.-Y. Cheng, R.S. Katiyar, X. Yao and A.S. Bhalla, Phys. Rev. B **57**, 8166 (1998).

[167] H. Okamoto, T. Mitani, Y. Tokura, S. Koshihara, T. Komatsu, Y. Iwasa, T. Koda and G. Saito, Phys. Rev. B **43**, 8224 (1991).

[168] M. Lang, J. Müller, F. Steglich, B. Wolf, M. Dumm and M. Dressel, J. Phys. IV (France) **114**, 111 (2004).

[169] A. Brühl, B. Wolf, V. Pashchenko, M. Anton, C. Gross, W. Assmus, R. Valenti, S. Glocke, A. Klümper, T. Saha-Dasgupta, B. Rahaman and M. Lang, Phys. Rev. Lett. **99**, 057204 (2007)

[170] M. Dumm, A. Loidl, B.W. Fravel, K.P. Starkey, L.K. Montgomery and M. Dressel, Phys. Rev. B **61**, 511 (2000).

[171] V.J. McBrierty, D.C. Douglass, F. Wudl and E. Aharon-Shalom, Phys. Rev. B **26**, 4805 (1982).

[172] S. Brazovskii, Springer series in Physics, to be published, cond-mat/0606009.

[173] J.-P. Pouget, P. Foury-Leylekian, D. Le Bolloc'h, B. Hennion, S. Ravy, C. Coulon, V. Cardoso and A. Moradpour, J. of Low T. Phys. **142**, 147 (2007).

[174] W.A. Herrmann, R.W. Fischer and W. Scherer, Adv. Mater. **4**, 653 (1992).

[175] H.S. Genin, K.A. Lawler, R. Hoffmann, W.A. Herrmann, R.W. Fischer and W. Scherer, J. Am. Chem. Soc. **117**, 3244 (1995).

[176] R. Miller, Ch. Helbig, G. Eickerling, R. Herrmann, E.-W. Scheidt and W. Scherer, Physica B **359-361**, 448 (2005).

[177] R. Miller, E.-W. Scheidt, G. Eickerling, C. Helbig, F. Mayr, R. Herrmann and W. Scherer, Phys. Rev. B **73**, 165113 (2006).

[178] E.-W. Scheidt, R. Miller, Ch. Helbig, G. Eickerling, F. Mayer, R. Herrmann, P. Schwab and W. Scherer, Physica B **378**, 1132 (2005).

[179] B.L. Altshuler and A.G. Aronov, Electron-Electron Interaction in Disordered Systems, North-Holland, Amsterdam (1985).

[180] K. Segawa and Y. Ando, Phys. Rev. B **59**, R3948 (1999).

[181] P.A. Lee and D.S. Fisher, Phys. Rev. Lett. **47**, 882 (1981).

[182] M. Eremets, High Pressure Experimental Methods, Oxford Science Publications (1996).

[183] Private communication from the company NGK Deutsche Berylco GMBH.

[184] L.D. Jennings and C.A. Swenson, Phys. Rev. **112**, 31 (1958).

[185] Additional information about this pressure cell can be found at the web site of the EL ElectroLAB Company http://www.h4.dion.ne.jp/∼el.com.

[186] K.C. Rule, A.U.B. Wolter, S. Süllow, D.A. Tennant, A. Brühl, S. Köhler, B. Wolf, M. Lang and J. Schreuer, Phys. Rev. Lett. **100**, 117202 (2008).

[187] M. Yamashita, N. Tanaka, Y. Kasahara, T. Sasaki, N. Yoneyama, N. Kobayashi, S. Fujimoto, T. Shibauchi and Y. Matsuda, Nature Physics, in press.

[188] N.W. Aschcroft and D. Mermin, Solid State Physics (Chapter 22), College Edition, USA (1976).

List of Abbreviations and Symbols

- α — Thermal expansion coefficient
- β — Spontaneous magnetization critical exponent
- γ — Magnetic susceptibility critical exponent or Sommerfeld coefficient
- δ — Magnetization critical exponent or charge disproportionation
- $\tilde{\alpha}$ — Specific heat critical exponent
- α- , β-, κ- and θ-phase — Phases of the (BEDT-TTF) charge-transfer salts
- λ — Screening constant
- μ — Chemical Potential
- μ_B — Bohr magneton
- ρ — Resistivity or density
- χ — Magnetic susceptibility
- ^{o} — Unit of angle, degree
- 1-, 2-, 3-D — One-, two-, three-dimensional
- A — Acceptor
- A — Affinity of the acceptor A
- a_0 — Bohr radius
- AFI — Antiferromagnetic-insulator
- AO — Anion Ordering
- BEDT-TTF — bis(ethylenedithiolo)-tetrathiofulvalene
- ^{0}C — Celsius degree
- C — Capacitance
- CO — Charge-Ordering or Charge-Ordered
- CDW — Charge Density Wave
- D — Donor
- DMFT — Dynamical Mean-Field Theory

- D8 Fully deuterated
- e Electron charge
- ET Bis(ethylenedithiolo)-tetrathiofulvalene
- F Helmholtz free energy
- FCC Face-centered cubic crystal structure
- FL Fermi-liquid
- FS Fermi Surface
- G Gibbs free energy
- $\hbar$ Planck Constant
- H8 Fully hydrogenated
- I Ionization energy
- IR Infra-red
- J Coupling constant
- K Kelvin
- K Kinetic energy
- loc Localization
- M Magnetization or Madelung energy
- m_e Electron mass
- M_s Spontaneous Magnetization
- MI Metal-insulator transition
- NI Neutral-ionic transition
- NMR Nuclear Magnetic Ressonance
- NTE Negative Thermal Expansion
- PI Paramagnetic-insulator
- PID Proportional-Integral-Derivative
- Poly-MTO Poly-methyltrioxorhenium
- PM Paramagnetic-metal
- $P-T$ Pressure versus Temperature
- Q1D, Q2D Quasi-one-, quasi-two-dimensional
- S Entropy
- SC Superconductor
- SF Spin-flop
- SDW Spin Density Wave

- SP — Spin-Peierls
- SQUID — Superconducting Quantum Interference Device
- T_c — Transition temperature to superconducting state
- T_{FI} — Transition temperature of the field-induced transition
- T_g — Glass-like transition temperature
- TLL — Tomonaga-Luttinger-liquid
- T_M — Melting point temperature
- T_{MI} — Metal-to-insulator transition temperature
- (TTF-CA) — Tetrathiafulvalene Chloranil
- TMTTF — Tetramethyltetrathiafulvalene
- TMTSF — Tetramethyltetraselenafulvalene
- U — Internal energy or Coulomb potential energy
- V — Intersite Coulomb interaction
- X — Monovalent Anion

Curriculum Vitae

- August 14th, 1972 born in Mogi das Cruzes - São Paulo - Brazil.

- 1981-1988 Elementary school at Mogi das Cruzes (EEPSG Dr. Deodato Wertheimer).
- 1987-1988 Industrial learning course at Senai - Mogi das Cruzes.
- 1988-1994 Worked at NGK of Brazil.
- February-November 1991 Joined the army.
- 1990-1994 High school at Mogi das Cruzes ETE Presidente Vargas - Mechanic Technique course.
- 1994-1996 Studies of Engineering and Mathematics at Braz Cubas University - Mogi das Cruzes.
- 1995-1996 Worked in industries: Eletropaulo (Electricity of São Paulo) and Air Products Industrial of Gases.
- 1997-2000 Studies of Physics (graduate and bachelor) at Universidade Estadual Paulista.
  Scientific Initiation Work: "A.C. Conductivity and Dielectric Constant in Conducting Polymers".
  Advisor: Prof. Dr. Lygia Christina de Moura Walmsley.
- 2001-2002 Masters Degree at Universidade Estadual Paulista
  Project: "Non-linear Electrical Properties of Conjugated Polymers".
  Advisor: Prof. Dr. Lygia Christina de Moura Walmsley.
- February-August 2003 Lectures at Universidade Estadual de Campinas - UNICAMP.
  Course given: Experimental Physics I.

- October 2003 - March 2004 German language course at Goethe Institute Mannheim-Heidelberg, Germany.
- April 2004 - May 2005 Research on low-dimensional materials at 1. Physikalisches Institut (Prof. Dr. Martin Dressel's Group), University of Stuttgart, Germany.
- June 2005 - November 2008 Ph.D. project at physics institute - Prof. Dr. Michael Lang's group - in the Goethe University Frankfurt (M), Project: "Investigation of the transport and thermal properties of low-dimensional organic compounds".

- Awards and Honors
  August 1999 - December 2000 Scholarship: FAPESP (The State of São Paulo Research Foundation) - Grants Nr. 99/04314-0.

  Marc 2000 - February 2003 Scholarship: FAPESP (The State of São Paulo Research Foundation) - Grants Nr. 00/12956-1.

  April-August 2003 Scholarship: (Scholarship for Graduate Instructors - UNICAMP).

  October 2003 - March 2004 Scholarship: DAAD (Deutscher Akademischer Austauschdienst) - Grants Nr. A/03/42348.

  March 2004 - March 2008 Scholarship Capes - Brazilian Agency (Commission for Improvement of Staff of Academic Level - Comissão de Aperfeiçoamento de Pessoal de Nível Superior) - Grants Nr. BEX-1052-039.

List of Publications

Parts of this work have already been reported in the following publications:

- Thermodynamic Studies at the Charge-Ordering and Spin-Peierls Transition in $(TMTTF)_2X$, M. de Souza, A. Brühl, J. Müller, P. Foury-Leylekian, A. Moradpour, J.-P. Pouget and M. Lang, Physica B (invited paper), in press.
- Evidence for Lattice Effects at the Charge-Ordering Transition in $(TMTTF)_2X$, M. de Souza, P. Foury-Leylekian, A. Moradpour, J.-P. Pouget and M. Lang, Physical Review Letters **101**, 216403 (2008).
- Lattice Effects and Entropy Change at the Mott Transition in a Quasi-2D Organic Conductor, M. Lang, M. de Souza, A. Brühl, Ch. Strack, B. Wolf, D. Schweitzer, Physica B, **403**, 1384 (2008).
- Anomalous Lattice Effects at the Mott Transition in a Quasi-2D Organic Conductor, M. de Souza, A. Brühl, Ch. Strack, B. Wolf, D. Schweitzer and M. Lang, Physical Review Letters, **99**, 037003 (2007).
- Comparative Transport and Thermal Expansion Studies on Quasi-2D Organic Superconductors Close to the Metal-To-Insulator Transition, Michael Lang, Mariano de Souza, Andreas Brühl, Christian Strack, Bernd Wolf, John A. Schlueter, Jens Müller, Dieter Schweitzer, *Proceedings of the 8^{th} Intern. Conf. on Materials and Mechanisms of Superconductivity - High Temperature Superconductors*, Physica B, **460-462**, 129 (2007).

Other publications:

- Magnetic Behavior of Poly(3-methylthiophene): Metamagnetism and Room Temperature Weak Ferromagnetism - O.R. Nascimento, A.J. A Oliveira, A.A. Correa, L.O.S. Bulhões, E.C. Pereira, V.M. Souza, L. Walmsley, Phys. Rev. B **67**, 144422-1 (2003).
- Field Dependent Conductivity at low electric fields in pressed pellets of doped poly(3-methylthiophene): Evidence of charge density wave depinning - V.M. Souza, L. Walmsley. A.A. Correa and E.C. Pereira, Solid State Communications **126**, 141 (2003).
- Evidence of Room Temperature Charge Density Wave Behavior and Glass - like States in Pressed Pellets of Lightly Doped Poly (3-methylthiophene) - V.M. Souza, L. Walmsley, A.A. Correa, E.C. Pereira and A.L. Gobbi, Molecular Crystal and Liquid Crystals **374**, 119 (2002).

Publications in newspapers and magazines:

- The Nobel Prize in Physics 2007 (in Portuguese) - newspaper Diário de Mogi, Edition of October 11th 2007.
- Electrons in Low Dimensions (in Portuguese), Publication in Portuguese in Ciência Hoje Magazine, January-February (2007).
- A discussion on the profession of Physicist in Brazil (in Portuguese) - newspaper Diário de Mogi, Editions of August 05th 2007 and August 16th 2003.
- Slow and Late (in Portuguese), newspaper Folha de São Paulo, Edition of May 29th 2002. In this article, a brief discussion on the unequalness of access to education in Brazil is presented.
- Proposition of an elementary mathematical problem, published in the Magazine of the Institute of Mathematics of the Braz Cubas University (www.brazcubas.br) - ALEPH (1996).

Presented posters in conferences

- ECRYS-2008, 5th International Workshop on Electronic Crystals: Dilatometric Studies at the Charge-Ordering and Spin-Peierls Transition in $(TMTTF)_2X$ - Mariano de Souza, Pascale Foury, Alec Moradpour, Jean-Paul Pouget and Michael Lang - Cargese - France - August 24th - 30th, 2008.
- German Spring Meeting: Magnetic Field Effects on a Quasi-2D Organic Compound Close to the Mott Transition - Berlin - Germany - February 2008.
- International Symposium on Crystalline Organic Metals Superconductors and Ferromagnets - ISCOM: Exploring Magnetic Field Effects in the Vicinity of the Mott Transition in a Quasi-2D Organic Conductor - M. de Souza, A. Brühl, Ch. Strack, B. Wolf, D. Schweitzer, M. Lang - Valencia - Spain - September 2007.
- International Conference on Strongly Correlated Electron Systems: Anomalous Lattice Response at the Mott Transition of a Quasi-2D Organic Conductor - Houston - USA - May 2007.
- German Spring Meeting: Pressure Studies on the Polymeric Compound poly-methyltrioxorhenium (poly-MTO) $(CH_3)_{0.9}ReO_3$ - Dresden - Germany - March 2006.
- Workshop on Strange Metals: Evidence of Charge-Density Wave Behaviour in Pressed Pellets Doped poly(3-methylthiophene) - International Center of Condensed Matter (ICCM) - Brasilia/DF - Brazil - November 2002.
- XXVth National Meeting of Condensed Matter Physics - Non-Linear Conductivity and Charge-Density Wave Depinning in Conducting Polymers - Caxambu/MG - Brazil - 2002.
- XXVth National Meeting of Condensed Matter Physics - Evidence of Magnetic Interaction from Electron Spin Resonance Measurements in Pressed Pellets of Poly(3-Methylthiophene) Doped With ClO_4^- - Caxambu/MG - Brazil - 2002.

- XXIVth National Meeting of Condensed Matter Physics - Multiplicity of Conductive States in Pressed Pellets of Lightly Poly(3- Methylthiophene) - São Lourenço/MG - Brazil - 2001.
- VIth International Conference on Frontiers of Polymers and Advanced Materials (ICFPAM) - Evidence of Room Temperature and Glass - like States in Pressed Pellets of Lightly Doped Poly(3-Methilthiophene) - UFPE - Recife/PE - Brazil - 2001.

Talks

- Exploring Lattice Effects in Organic Charge-Transfer Salts Close to the Mott MI Transition - Students Seminary in Solid State Physics - Physics Institute - Goethe University - Germany - November 3rd 2008.
- Collective Phenomena in Charge-Transfer Salts Close to the Mott Transition - Meeting of the SFB/TRR49 - Waldthausen - Mainz - Germany - September - 26th 2008.
- Charge-Transfer Salts: A Brief Overview - DAAD Meeting - University of Frankfurt - Germany - June 17th 2008 (invited talk).
- Exploring Lattice Effects at the Mott Transition in a Quasi-2D Organic Conductor via High-Resolution Thermal Expansion Experiments - Theoretical Physics Department - University of Frankfurt - Germany - May 20th 2008 (invited talk).
- Charge Ordering in $(TMTTF)_2X$: Evidences for Structural Changes - German Spring Meeting - Berlin - Germany - February 2008.
- Anomalous Lattice Response at the Mott Transition in a Quasi-2D Organic Compound - Edgar Lüschner Seminar - Sport-Kloster - Switzerland - February 2008 (invited talk).
- Magnetic-Field-Induced Phase Transition in the Quasi-2D Compound κ-$(ET)_2Cu[N(CN)_2]Br$ - Group Seminary - Physics Institute - University of Frankfurt - September 2007.
- Anomalous Lattice Response at the Mott Transition in κ-$(D8\text{-}ET)_2Cu[N(CN)_2]Br$ - 1. Physics Institute - University of Stuttgart - August 2007 (invited talk).
- Thermal Expansion on $(TMTTF)_2PF_6$ - Group Seminary - Physics Institute - University of Frankfurt - July 2007.
- Report on the International Conference on Strongly Correlated Electron Systems (SCES) 2007 in Houston, Texas, USA - Group Seminary - Physics Institute - University of Frankfurt - June 2007.
- Lattice Response at the Mott Transition in a Quasi-2D Organic Conductor", M. de Souza, A. Brühl, Ch. Strack, B. Wolf, D. Schweitzer and M. Lang - German Spring Meeting, Regensburg - Germany, March 2007.
- Magnetic Measurements Under Pressure Using an Oil Pressure Cell - Group Seminary - Physics Institute - University of Frankfurt - January 2007.
- Thermische Ausdehnungsmessungen mit Subatomarer Auflösung - Solid State Physics Course WS 06/07 - University of Frankfurt - February 2007.

- The Mott Metal-Insulator Transition - talk given in the frame of the course "English for Academic Purposes" - University of Frankfurt - November 2006.
- Thermal Expansion Measurements on κ-(D8-ET)$_2$Cu[N(CN)$_2$]Br organic conductor - Group Seminary - Physics Institute - University of Frankfurt - May 2006.
- Polymeric Methyltrioxorhenium (poly-MTO)$(CH_3)_{0.9}ReO_3$ - Group Seminary - Physics Institute - University of Frankfurt - January 2006.
- Description of the resistivity setup for ambient and high pressure measurements - Group Seminary - 1. Physics Institute - University of Stuttgart - June 2004.
- A Study of the non-linear electrical properties in conjugated polymers - Group Seminary - 1. Physics Institute - University of Stuttgart - November 2003.

Teaching activities during the realization of this project

- Summer Semester 2008, Winter Semester 2008-2009 - Tutor of the experiment *Superconductivity and Phase Transitions* in the frame of the advanced laboratory courses for Physics students (in German).
- Winter Semester 2007-2008 - Tutor of the experiments Superconductivity and Zeeman Effect in the frame of the advanced laboratory courses for Physics students (in German).
- 4th - 11th October 2007 - Lab course for undergraduate students: High-resolution Thermal Expansion Measurements on Nb at the Superconducting Transition (in German).
- Winter Semester 2005-2006, Summer Semester 2006, Winter-Summer Semester 2006-2007, Summer Semester 2007: Exercises Lessons of Physics (Mechanic, Electrostatic, Optics and Thermodynamics) for students of neighbor areas (Biology, Chemistry, Geophysics and Biochemistry) (in German).

Acknowledgements

My interest in participating in actual scientific research evolved in 1994 when I was studying mechanical engineering in Mogi das Cruzes (my hometown). After studying engineering for approximately two years, I realized that my heart was in physics. I thus abandoned the world of engineering and start to study physics in Rio Claro - São Paulo. Already in the first year of the physics course, I had adventured into the field of fractal-chaos theory and astronomy, but during this time I realized that pure theoretical work was not where my real interest lay. I began the journey into the solid-state/low-temperature physics world already with my scientific initiation, starting in 1997. The more I explored it, the more I learned about the physics, and the more I found it exciting to investigate and try to understand the states of matter at low temperatures. These years have now passed and although the time elapsed might seem long just for obtaining a degree, I see that it is indeed very short, compared to a life of learning and teaching which awaits.

During the time of my promotion, my enlightenment has been very well assisted by my advisor, Prof. Dr. Michael Lang. I am grateful to him for the never-ceasing support, for the optimistic attitude, for the constant good humor, as well for the opportunity of making physics in the fantastic field of organic conductors in his group. However, I would not find my self in this track if it were not Prof. Dr. Lygia Walmsley and her advice at the very beginning of my career. During the ISCOM-2007 hold in Valencia-Spain she told Prof. Lang: ”Mariano is a fighter”. It was really not easy to overcome the adversities during my scientific career and I thank Prof. Walmsley for her support and encouragement. Unfortunately I cannot recall all the occasions at which I received invaluable support, advice and criticism. Among others I wish to thank: Dr. Marc Duran Serrano, Dr. Axel Nothardt, Dr. Belal Salameh and Dr. Marc Scheffler for the useful discussions during the time that I worked in Stuttgart. In Frankfurt, I have been greatly supported by all my colleagues, researchers from the Institute of physics and all the technical staff, especially Dr. Andreas Brühl (my mentor at the beginning in the challenge of thermal expansion experiments) and also Dr. Ulrich Tutsch, PD Dr. Bernd Wolf, Sebastian Köhler, Dr. Volodymyr Pashchenko, Dr. Yeekin Tsui, Katarina Removic-Langer, Christian Strack (mainly for his help during the transport experiments under pressure on poly-MTO at the very early beginning of my work in Frankfurt), Rudra Sekhar Manna, Dr. Deepshikha Jaiswal-Nagar, Thanh Cong Pham, Daniel Hofmann, Ammar Naji and Geoerg Hofmann. I thank also Prof. Dr. Pouget, Prof. Dr. Müller and Dr. Michael Dumm for many useful discussions. My great warm thanks are also to Ms. Carolyne Agnew who improved the English of my Thesis considerably. I thank also Mr. Dübel for the computational support, Mr. Pfeiffer, Mr. Junk and Mr. Bass for the technical support in the mechanical workshop, as well Mr. Isselbächer. Also my warm thanks to Siegfried Rapphahn for the support providing the necessary cryogenic liquids, always ”on time”, for the realization of the experiments which resulted in this work. My many thanks to

Latex expert Dr. Pablo Parmezani Munhoz for the support during the writing of this work. I thank DAAD (Deutscher Akademischer Austausch Dienst) for the scholarship awarded to me to study the German language at Goethe Institute Mannheim-Heidelberg before the start of my Ph.D. work here in Germany. My thanks to the Brazilian Foundation CAPES (Comissão de Aperfeiçoamento de Pessoal de Ensino Superior) (Grants number BEX 1052-039). This work is part of the SFB/TRR 49 *Condensed Matter Systems with Variable Many-Body Interactions* supported by German Science Foundation.

A person living a life in science may, on many occasions, be very unbearable to those close to him. I thank my mother Mair, my father João Mariano and my sisters Mair and Doraci as well as my niece Helena Maria. I thank Fabiana, Luiz and Ms. Costa and all the rest of my family. I thank the Nilsons' and Pfälzerin. Finally, I thank my friends and all those people who have supported me during my studies that finally led to this dissertation. My many thanks.

Valdeci Pereira Mariano de Souza
Frankfurt (M), November 2008.

**"Wer kämpft kann verlieren,
wer nicht kämpft hat schon
verloren."**
Rüdiger Nehberg
(German baker, 1935 -)

Appendix 1

Non-magnetic liquid pressure cell

During the realization of the present work, a self-built closed clamped oil pressure cell was produced. This cell consists basically of a cooper-beryllium (CuBe) cylindrical vessel, which is used like a pressure generator for measuring the magnetic properties of the samples. Pressure, on the sample to be studied, was applied by using an hydraulic press supplied by the company Schmidt Maschinentechnik. According to the literature, CuBe is one of the most used materials in the fabrication of the components (like piston, sleeve, etc) of pressure cells used for electrical and magnetic measurements, see e.g. [67]. In order to obtain a CuBe alloy with low content of impurities, which in other words means a small magnetic contribution from the body of the pressure cell in the magnetic measurements, susceptibility measurements on two different alloys of CuBe supplied by two different companies were carried out. For these measurements, a commercial SQUID (Superconducting Quantum Interference Device) magnetometer MPMS (Magnetic Property Measurement System) of the company Quantum Design was used. The magnetic susceptibility as a function of temperature is shown in Fig. 1.

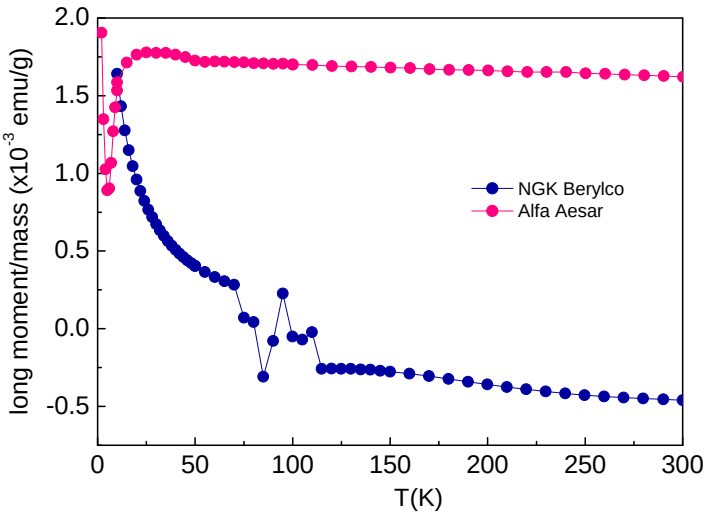

Figure 1: The temperature dependent susceptibility under 1 T of CuBe alloy supplied by two different companies. Solid lines are a guide for the eyes.

The magnetic susceptibility of CuBe alloy supplied by the Alfa Aesar company shows a small temperature dependence down to $T \approx 25$ K. As can be seen from Fig. 1, the sus-

ceptibility is positive down to low temperature, characteristic of paramagnetic or ferromagnetic contribution due to the magnetic impurities. Around $T \approx 25\,\mathrm{K}$, a drop is observed. The susceptibility of the CuBe alloy supplied by NGK Berylco company presents diamagnetic behavior down to $T \approx 25\,\mathrm{K}$, where an increase of the susceptibility is observed. This is quite different from the magnetic behavior of the CuBe sample supplied by Alfa Aesar company. The latter is most likely due to the presence of Ni, Co or Fe in this alloy. According to this company [183], the concentration of the above-mentioned magnetic impurities are Ni $< 0.30\%$, Co $< 0.30\%$ and Fe $< 0.30\%$. Due to its very low diamagnetic contribution at high temperatures, accompanied by a well defined Curie-type behavior at low temperatures, CuBe (Standard 25 alloy) supplied by NGK Berylco company was used in the fabrication of the pressure cell. This information might be useful for future projects, in which CuBe alloys could be used. As pressure fluid media, Fluorinert FC-77 1 : 1, supplied by the 3M company, was used. The advantage of using FC-77 is its high compressibility factor. The pressure values on the sample at low temperatures were determined indirectly by measuring the critical temperature of In. The dependence of the superconducting transition temperature T_c as a function of temperature is well-known in the literature. As reported in Ref. [184], the coefficient $(\partial T_c/\partial p)$ for In at zero field is $0.042\,\mathrm{K/kbar}$. Nevertheless, in employing this self-built pressure cell we could not achieve hydrostatic pressure. This was observed by analyzing the dependence of the In critical temperature for different pressures. For this reason, a commercial pressure cell was acquired.

A commercial hydrostatic pressure cell (Model LPC-15) also made of CuBe, manufactured by the Japanese company EL ElectronLAB [185], was then acquired. The latter was installed, calibrated and used to perform magnetic measurements under pressure on the natural mineral Azurite $Cu_3(CO_3)_2(OH)_2$, proposed as a realization of the $S = 1/2$ diamond chain, see [186] and references therein.

The magnetic susceptibility of In under selected pressures is shown in Fig. 2. The criterion for estimating the superconducting transition temperature in such measurements was to take the temperature at which, ignoring any rounding of the the transition curve, the In sample first became superconducting, i.e. the onset temperature was taken as T_c.

Although a similar pressurization procedure has been supplied by the company, the pressurization procedure of the pressure cell for magnetic measurements, as supplied by the company, is presented here in a more detailed way. The mentioned parts (typed in italic) refers to Fig. 3. In the following, the pressurization procedure is described.

1. Insert each *O-ring* on to one of the two *CuBe-plugs*. In the following, these two pieces are referred to as *O-ring + CuBe-plugs*.

2. Screw the *cylinder case bolt* on to the lower end of the *cylinder* and insert *CuBe-plug* and *Cu-Ring* through the inlet of the *cylinder case bolt*. Push *CuBe-plug* and *O-ring* inside up to 25 mm by using *sample exchange aggressiveness stick*. There will be no consequences, if *O-ring + CuBe-plugs* are pushed in too far.

3. Remove *cylinder case bolt* from *cylinder* and equip the top part of *cylinder case bolt* with *Cu-ring*. Afterwards screw *cylinder case bolt* on to *cylinder* (same position as before).

4. Exchange *cylinder case bolt* with lower pressure *clamping bolt*.

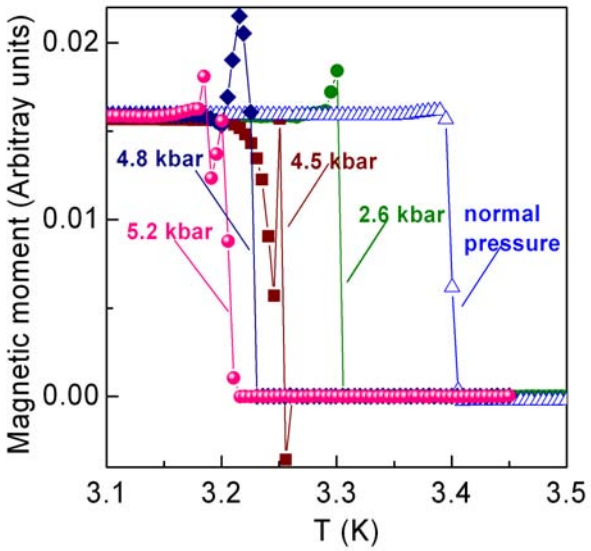

Figure 2: Magnetic susceptibility of an In sample under various pressures, as indicated by different colors. The indicated pressure values correspond to the estimated pressures at low temperatures.

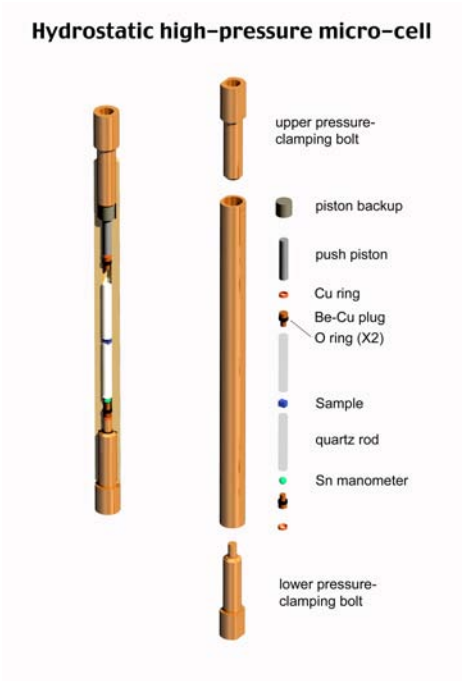

Figure 3: Pressure cell used for magnetic measurements under pressure. Picture supplied by EL ElectronLAB Company.

5. Push through upper inlet of *cylinder* the previously inserted *Cu-ring* and one each of *CuBe-plug* and *O-ring* as far down as possible by using *sample exchange aggressiveness stick* again.

   If not stated otherwise, "insert" means "insert into *cylinder* through the upper inlet".

6. Insert *Indium-manometer* and afterwards *quartz rod*.

7. Insert *sample*.

8. Remove the needle from the syringe and fill the syringe with 0.6 cc *Daphne oil 7373*. Afterwards equip the syringe with the needle and pour *Daphne oil 7373* into the *cylinder*, by holding the point of the needle to the *cylinder* sidewall. Make sure, that there is no air in the syringe before pouring in.

9. Screw *cylinder case bolt* on to the upper end of *cylinder* and insert the other *quartz rod*, which sinks in automatically.

10. After removing *cylinder case bolt* from , by holding the point of the needle to the pour in *Daphne oil 7373* to the height of about 22 mm.

11. Equip the upper end of *cylinder* again with *cylinder case bolt* and insert the other *O-ring + CuBe-plugs* by pushing with *sample exchange aggressiveness stick*. This time the pushing requires some force and as a result there will be some overflow of *Daphne oil 7373*.

12. Loosen *lower pressure-clamping bolt* by unscrewing it (around four rotations). After each rotation push the upper *CuBe-plug* and *O-ring* deeper by using *sample exchange aggressiveness stick* again. Every rotation corresponds to roughly 1 mm. Remove *cylinder case bolt*, equip the *cylinder* with *CuBe-plug + Cu-ring*.

13. Equip *upper pressure-clamping bolt* with *piston-backup* and *push piston* by using grease. Do not tighten *upper pressure-clamping bolt* too much. It may be easier, if you insert *push piston* before assembling it with *upper pressure-clamping bolt* and *piston-backup*. *Push piston* will break upon applying pressure, if it is not put into *cylinder* properly.

14. Fasten the previously loosened *lower pressure-clamping bolt* (four rotations). Clamp the pressure cell in *cylinder case*.

15. Insert *pressurization aggressiveness stick*, so that it is pushing on *piston-backup*. The assembling is finally complete. A sample holder provided by the company should be used to place the cell into the Squid magnetometer.

Appendix 2

Estimate of the expected height of the specific heat anomaly at T_{MI} in κ-D8-Br

Firstly, from basic thermodynamics, let us deduce the entropy change as a function of the specific heat. The specific heat at constant pressure is defined by:

$$C_p = \frac{\Delta Q}{\Delta T} \tag{1}$$

Where,

$$\Delta Q = T dS \tag{2}$$

Combining Eqs. 1 and 2, one achieves:

$$C_p = T\frac{dS}{dT} \tag{3}$$

Rearranging Eq. 3, one obtains:

$$dS = \frac{C_p}{T} \tag{4}$$

Integrating Eq. 4, one has:

$$\Delta S = \int \frac{C_p}{T} dT \tag{5}$$

Now, assuming a T^3 phonon background, the anomalous contribution to the thermal expansion coefficient along the *a*-axis $\alpha_a^{anom}(T)$ (see Fig. 4.14) at T_{MI} can be estimated. The latter is then used to estimate the anomalous contribution in the specific heat C_p^{anom}, as follows:

$$\int \frac{C_p^{anom}}{T} dT = \Delta S = \frac{1}{\gamma^{anom}} \int \frac{\alpha_a^{anom}(T)}{T} dT \tag{6}$$

The factor γ^{anom} in Eq. 6 is a proportionality factor, which defines the connection between $\alpha_a^{anom}(T)$ and C_p^{anom}:

$$\Delta C_p^{anom} = \frac{1}{\gamma^{anom}} \Delta \alpha_a^{anom} \tag{7}$$

Making use of the entropy change associated with the Mott MI transition, estimated in Section 4.6.2, and solving the integral in the left side of Eq. 6 the proportionality factor γ^{anom} can be obtained (γ^{anom} = 392 $\cdot$ 10^{-6} molJ^{-1}). Hence, substituting the obtained γ^{anom} value and $\Delta \alpha_a^{anom}$ = (60 $\cdot$ 10^{-6}) K^{-1} into Eq. 7 results in ΔC_p^{anom} = 0.15 Jmol$^{-1}K^{-1}$.